ABRASIVE ASSISTED BRUSH DEBURRING OF MICROMILLED FEATURES WITH APPLICATION TO A NOVEL SURGICAL DEVICE

A Dissertation
Presented to
The Academic Faculty

by

George K. Mathai

In Partial Fulfillment
of the Requirements for the Degree
PhD in the
George W. Woodruff School of Mechanical Engineering

Georgia Institute of Technology
May 2013

ABRASIVE ASSISTED BRUSH DEBURRING OF MICROMILLED FEATURES WITH APPLICATION TO A NOVEL SURGICAL DEVICE

Approved by:

Prof. Shreyes Melkote, Co-Advisor
George W. Woodruff School of Mechanical Engineering
Georgia Institute of Technology

Prof. Steven Danyluk
George W. Woodruff School of Mechanical Engineering
Georgia Institute of Technology

Prof. David Rosen, Co-Advisor
George W. Woodruff School of Mechanical Engineering
Georgia Institute of Technology

Prof. Ken Gall
School of Material Science and Engineering
Georgia Institute of Technology

Dr. Timothy Olsen, MD
Department of Ophthalmology
Emory University

Date Approved: December 05, 2012

ACKNOWLEDGEMENTS

I would like to thank the following people for making this thesis possible:

Jesus Christ: My hope, reason for living and inspiration.

My family: Dad, Mom, Mathew, Vinaya and their families. Your support, encouragement and prayers are invaluable.

My Advisors: Prof. Melkote and Prof. Rosen. Your guidance and inspiration has been critical to the contents of this study as well as my formation as a doctoral student.

My committee members: Prof. Danyluk, Prof. Gall and Dr. Olsen, for your erudite comments that have gone a long way in improving the quality of this study. Special thanks to Dr. Olsen for way more than just monetary support for this project.

Funding Agencies: Dobbs Foundation, EmtechBio, Georgia Research Alliance, Research to Prevent Blindness.

My labmates: Andrea, Craig, Christina, Hao, Jennifer, Lei, Mukund, Rui, Richard and Satya for your camaraderie and assistance.

PMRC/ME staff: Steven Sheffield, John Graham, Louie Boulanger, Kyle French, Vladimir Bortkevich, Ahn Nguyen, Pam Rountree and Melissa Raine for your technical and administrative support.

Emory University/UMN surgical team: Patryce, Kathy and Jenn for the long hours spent in surgical testing and your feedback.

Dr. Laroux Gillespie: For valuable discussion and input at the initial stages of this study.

Siddharth Avachat: For help with the Abaqus simulations in Chapter 7.

There are of course many more whose critical role directly or indirectly in the success of this project is deeply appreciated.

TABLE OF CONTENTS

LIST OF TABLES

LIST OF FIGURES

SUMMARY

Microscale features (or microfeatures) find application in several high-tech industrial sectors such as in the manufacture of biomedical, aerospace and consumer electronic components. Burrs severely inhibit the performance and aesthetics in these micromachined parts besides posing a safety risk to the user and manufacturer. Furthermore, machining of microfeatures in thin foils such as stents poses distinct challenges due to foil delamination and discontinuity at the foil-backing material interface. This makes it important to understand both the mechanics of burr formation in microparts as well as the methods and mechanisms by which they can be removed. Abrasive assisted brushing presents a fast and effective method for deburring these parts but is difficult to control. The dependence of deburring rate on the workpiece material, abrasive grit size, type and rotational speed of the brush is studied. It is found that deburring rate is proportional to the initial burr height indicating fracture of the burr at the root. Deburring rate increases with spindle speed and is higher for diamond grits than SiC. The formation of burrs in micromilling of a thin nickel-titanium alloy (nitinol or NiTi) foil used in implantable biomedical device applications is analyzed as a function of micromilling process parameters such as spindle speed, feed, tool wear, backing material and adhesive used to attach the foil to the backing material. All factors except spindle speed are found to affect burr size. If initial penetration is sufficient to cause the foil to fail in tension, the foil tears with the crack starting closer to the upmilling side thereby resulting in larger downmilling burrs. If penetration is insufficient, the foil plastically deforms until it tears typically in the middle of the cutter tooth path. A kinematic model that captures this behavior is used to predict burr widths and is verified through

experiments. The thesis also presents an investigation of the abrasive impregnated brush deburring process for thin NiTi foils. Models based on Hertzian indentation and fracture mechanics are proposed to predict the rates of indentation and deburring during brushing and are validated using experiments. Model predictions are found to be within the experimental variation. Burrs can be removed with this process within 12 minutes for a 6 mm long groove with no more than a micron change in foil thickness. Knowledge of burr formation and deburring is applied to a novel micromilled thin shape memory based NiTi foil device used for the surgical correction of Age-related Macular Degeneration (AMD), a leading cause of blindness in the western world in those over age 50. Burrs on the surface of the structure are used successfully to mechanically constrain and translocate an autograft to replace the diseased RPE-Bruch's membrane under the macula. The shape memory device is analyzed using experiments and finite element analysis. It is found that the force generated by shape memory is negligible and tissue damage is minimal during thermal activation of the device.

CHAPTER 1

INTRODUCTION

Deburring of Micromilled Features

Presence of burrs in micromilled parts is a major challenge that prevents their proper working, hinders part assembly, causes wear of other parts, leads to accumulation of dirt and poses a safety hazard to the operator. In micro fluidic channels they can increase the resistance to flow [1]. In biomedical applications, burrs increase the chance of autoimmune rejection of the inserted component [2]. It is impossible to machine burr free edges even with the best tool path planning [3, 4] necessitating a secondary edge finishing process. Deburring of micromilled features has distinct challenges over macromachined features since the size of the feature is comparable to the size of the burr (~30-100 μm). Techniques used at the macroscale, such as the use of deburring tools or grinding could be too aggressive, causing damage to the feature.

Brush deburring is a popular technique in industry primarily because it is inexpensive, but it has several other advantages including the ability to deburr a wide variety of geometries and materials, low brushing forces leading to reduced distortion of thin walled parts, absence of secondary burrs produced during deburring, ease of automation, low deburring time and the ability to accommodate inaccuracies in the set up due to the compliance of the brush [5]. Due to these benefits, this technique is recommended as the first option for deburring of microparts [6] but has not been studied for micromilled grooves. Consequently, this thesis focuses on a detailed study of the abrasive brush assisted deburring process.

Burr Formation in Thin Foils

Microscale features in thin foils or laminates find applications in some well known products such as coronary stents, electronics and in compliant mechanisms and flexures. Micromilling has been used to create precision parts for biomedical applications, micro heat exchangers and microfluidics applications [7]. Micromilling of thin foils can offer a cost effective option to manufacture sheet metal based microparts such as coronary stents. It could also be used to fabricte flexible and wearable electronics. Currently, these parts are fabricated using femtosecond pulsed lasers and Electrical Discharge Machining (EDM)[8, 9]. However, cost and machining rate considerations generally favor micromilling. For example, a typical femtosecond laser machining system can cost more than $300,000 [10]. On the other hand, a basic laboratory micromachining set-up can be built for about a tenth of the cost while a commercial micromachining system costs about $100,000 [11]. Typical processing speeds with femtosecond pulsed lasers are about 70 mm/min or lower to avoid a large heat affected zone (<5 μm) [8] while processing speeds for micromachining can be as high as 1000 mm/min for a foil of similar material (e.g. stainless steel). Micromilling tools as small as 5 μm in diameter are commercially available opening the possibility of extremely small feature sizes while still retaining the versatility of being able to manufacture larger 3D features in a wide variety of materials. Laser machining is typically limited to 2.5D features and may not be able to process some materials (e.g. aluminum) but allows for much smaller, submicron features to be created [12]. Moreover, one does not have to deal with tool breakage, which is quite common in micromilling. The major differences between the two processes are summarized in Table 1.

Table 1: Micromilling vs. laser machining

	Micromilling	**Laser Micromachining**
Cost (USD)	30k-100k	250k+
Typical processing speed (mm/min)	1000	70
Features	3D	2.5D
Materials	unlimited	nonreflective
Minimum feature size	~ 5 µm	submicron
Tool fracture	present	absent
Edge defects	burrs	recast material

Ploughing of material during micromilling cannot be neglected due to the larger tool edge and tip radii relative to the feed per tooth. It has been experimentally shown that burr size increases with a relatively larger edge radius in micromilling [3]. Micromachining of thin foils and laminates have distinct challenges in the form of foil deflection and delamination [13]. However, the study of burr formation in flexible foils has only focused on drilling and understanding of the mechanics of burr formation in these materials is absent. These aspects are investigated in this thesis.

Medical Device Application

Knowledge of burr formation and deburring obtained from this study is applied to the fabrication of a novel device used in the surgical correction of Age-related macular degeneration (AMD). This disease leads to the loss of central visual acuity from the loss of light-sensitive elements, known as photoreceptors (rods and cones) in a highly specialized region in the center of the retina referred to as the macula. The macula is a 5.5 mm region of the retina with the fovea (central 1.5 mm, central 15-20 degrees of visual field) that has the greatest density of cones; the specific cells responsible for color vision

and fine discrimination [14]. The National Eye Institute and results from other studies have identified AMD as a significant cause of vision loss in Americans 60 years and above [14-17].

Degeneration of the macula is caused due to deposition of extracellular material or leakage of blood vessels in the retinal pigment epithelium (RPE) and Bruchs membrane which lies beneath the macula and transports nutrients to it. Surgical correction of AMD involves re-supplying the macula with a healthy RPE-Bruchs-choroid graft using 3-port par plana vitrectomy techniques. Development of a mechanical device to support this delicate tissue avoids folding, injury, or loss of polarity of the translocated tissue [18]. In previous efforts, such a graft has been translocated using a spatula or with forceps. This often leads to damage and bleeding of the tissue [19]. Furthermore, studies have shown that the size of graft is limited by the size of the forceps used [18]. Therefore, the success of such a procedure would be increased by using a stable support structure that holds the tissue in its natural polarity and shape during translocation. The structure is also used to correctly orient the tissue under the fovea. The novel device used to perform this task is micromilled from 25 μm thick NiTi foil. Selective deburring is performed to remove the burrs on the areas that would cause inflammation while leaving them on areas where they can provide anchors to hold the tissue. The size of the anchor burrs are controlled within a range through the understanding of burr formation generated in this study.

Research Objectives

The focus of this research is to develop an improved scientific understanding of the brush deburring process for microscale features along with a fundamental understanding of burr formation in thin metal foils. The specific objectives of this study are:

- Evaluate abrasive slurry assisted brush deburring as a means to deburr microfeatures.
- Understand the mechanics of burr formation in thin foils as well as the effect of process parameters on the process.
- Understand the mechanics of material removal in brushing and abrasive impregnated brush deburring.
- Apply and verify the generated knowledge to the manufacture of a tissue translocation device.

These objectives are correspondingly broken down into four tasks which also form the framework of this document (Figure 1). A synopsis of prior research in the areas of burr formation, deburring of microparts and treatment of AMD is presented in Chapter 2 and this study is positioned relative to the current body of knowledge. Chapter 3 presents an experimental study of abrasive slurry assisted brush deburring of micromilled grooves in blocks of copper and tool steel. Burr height reduction rate, change in surface roughness and change in feature size are studied as a function of abrasive size, abrasive material, workpiece material and brush rotation speed. Chapter 4 focuses on understanding the effect of backing material, adhesive, tool wear and feed per tooth on burr height and a kinematic model is developed to predict burr width. The material removal mechanism in abrasive impregnated brushing of thin foils and deburring is investigated in Chapter 5 leading to a model to predict the penetration rates in the process. The shape memory foil based micromilled tissue support device for use in surgical correction of AMD is systematically designed in Chapter 6 using the Pahl and Beitz approach and evaluated with porcine in-vivo and ex-vivo studies. Finite element analysis (FEA) is used to estimate the clamping force generated by the shape memory effect, the maximum device deformation allowed and thermal gradients in the device during the surgery and the results are presented in Chapter 7. Tissue adhesion forces with and without burrs are also measured experimentally. Conclusions and original

contributions of these tasks are summarized and potential improvements are suggested in Chapter 8.

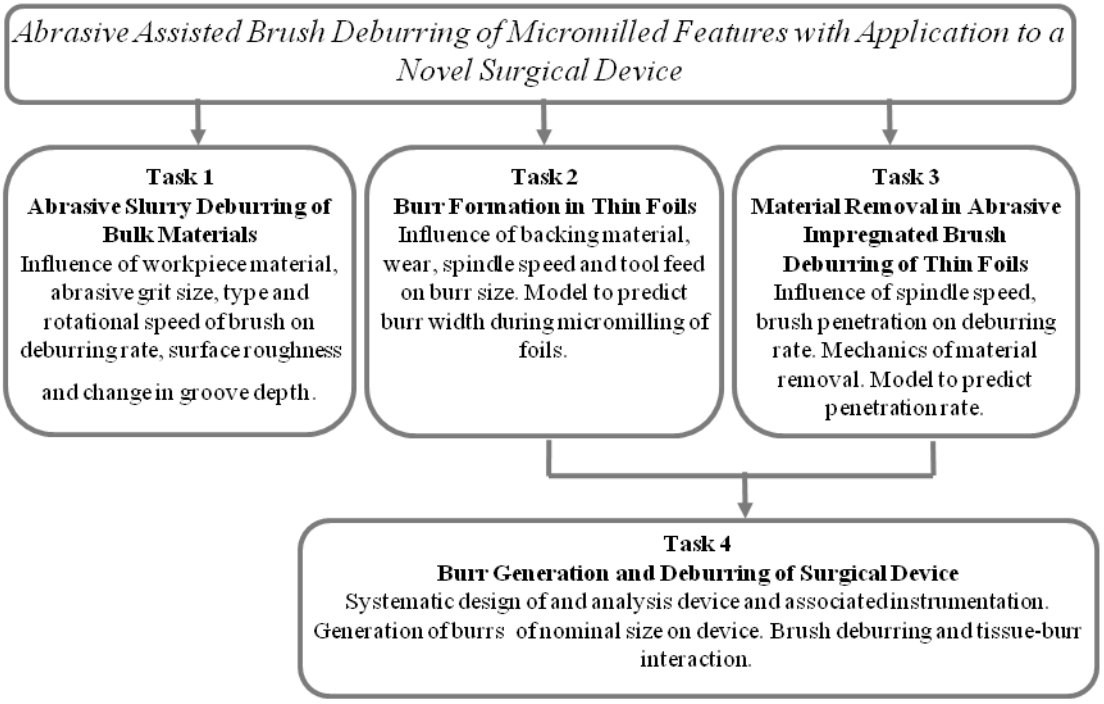

Figure 1: Overview of research approach

CHAPTER 2

LITERATURE SURVEY

Burrs are defined as “all material extending past the theoretical intersection of the two surfaces that surround the burr” [20]. Typically burrs are associated with plastic deformation during cutting or shearing in a machining operation. Sometimes the term is also used to describe flash and redeposited material in processes such as casting or electrical discharge machining respectively.

Burr Formation

Burr formation in conventional scale milling has been studied since the 1970s [21]. Based on formation mechanics, they have been classified into Poisson, entrance, rollover and tear burrs Figure 2. Poisson burrs are caused due to unintentional lateral flow of material due to compression of the workpiece by the tool edge. Entrance burrs are similar except they form during the initial contact of the tool and the workpiece. Tear burrs occur when the material tears in tension rather than being sheared as a chip. Rollover burrs form at the exit of a cut where the chip bends rather than shears under the action of the tool.

Burr Formation in Macroscale Machining

Orthogonal cutting experiments were used to classify burrs on two alternate basis namely, the cutting edge and the mode or direction of formation [22]. Based on the cutting edge, the burrs are classified and indicated by a symbol as major (M) and minor (C), while based on the direction of formation they are classified into backward (B), sideward (S), forward (F) and leaning (L). The experiments also indicated that the size of sideward burrs (Figure 2d) decreased with decreasing undeformed chip thickness,

decreasing shear strain, increasing the included angle and turning the cutting force direction towards the workpiece. Shear strain of the chip can be reduced by a high rake angle, high cutting speed, use of lubricant and coldworking of the workpiece.

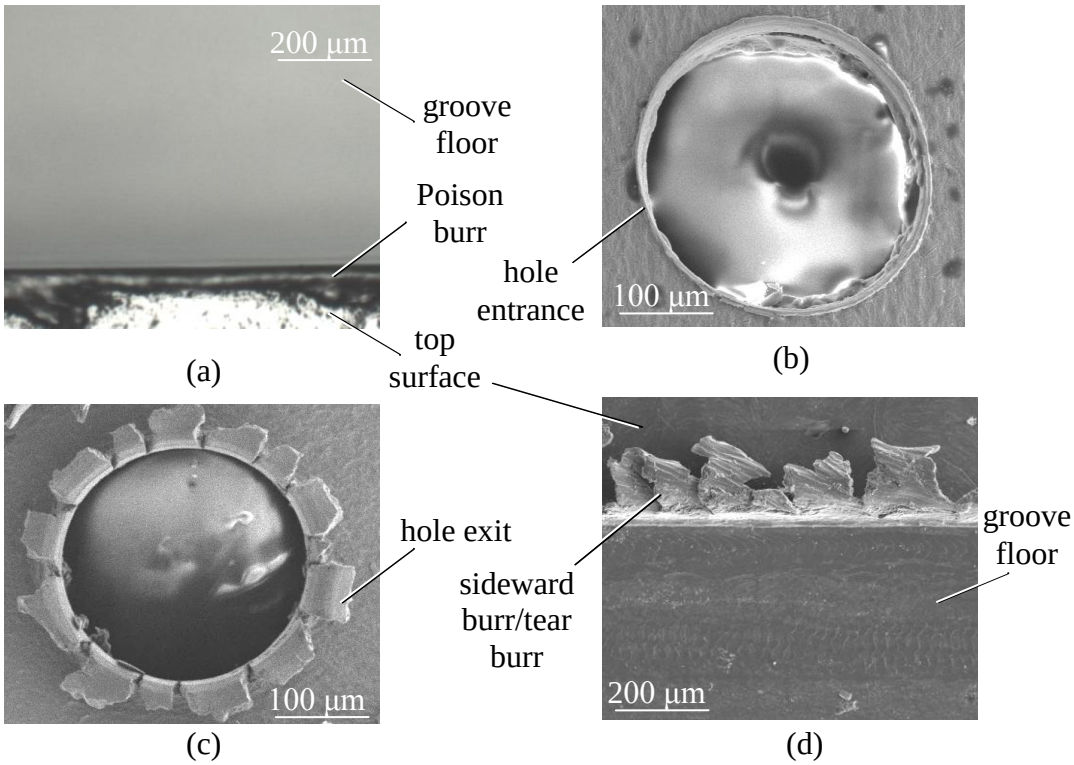

Figure 2: Types of burrs (a) Poisson burr (b) Entrance burr (c) Rollover burr (d) Tear burr

A model for describing the mechanics of material flow during formation of rollover burrs in soft materials (such as copper) in an orthogonal cutting process as the tool approaches the edge of the workpiece was developed based on the minimum energy principle [23]. As the tool approaches the edge of the workpiece, a negative shear zone develops between the tool and the workpiece edge and the material flow transitions from shear (causing chip formation) to plastic bending which causes the material to rollover and form a burr. An equation for the distance from the workpiece edge at which this transition takes place is developed based on measured initial negative shear angle, tool-chip contact length, shear angle and cutting force and good agreement was found with

experimental values. The model indicates that burr size reduces with increasing cutting speed.

Rigid-plastic finite element method (RPFEM) [24] was used to understand the effect of inclination angle on rollover burr formation in oblique cutting of mild steel. It was found that the chip forms a breakout region (fracture) in addition to a burr for high feed (50 μm for the tool and material used in the study) and that the exit burr size increased with increase in inclination angle. The orthogonal model in [23] was further extended to include oblique cutting by modifying Rubenstein's chip formation model [25, 26] and found to be applicable to materials that do not show significant chip distortion. The model can be used to predict the extent of breakout region. Burr formation was studied both experimentally and using RPFEM implemented in ABAQUS for orthogonal cutting of ductile and brittle materials [27]. It was found that while crack formation and fracture in breakout occurs along the primary shear zone for ductile materials, it occurs along the negative shear zone for brittle materials. As a result, ductile materials form a positive burr while brittle materials form a negative burr. Video footage of burr formation on samples with a mesh pattern sputtered on them was recorded to observe the strain in the material as the burr formed. As feed into the workpiece increases, the plastic deformation zone lengthens and the pivot point moves deeper into the material. The depth also increases as the tool edge radius increases. Burr size also increases with feed and edge radius.

Another finite element model of orthogonal cutting that included adiabatic heat generation during chip formation was implemented using the ductile failure criterion feature in ABAQUS-Explicit [28, 29]. The appropriate ductile failure criterion were identified for the different burr formation steps, namely steady state cutting, initiation to pivoting and pivoting to burr formation. It was found that reducing the exit angle and increasing the rake angle reduces the burr thickness. However, these criterion also lead to increased tool wear. This suggests that an optimum should be sought at which savings

due to reduced tool wear are balanced by expenditure on deburring. A thick backing material placed at the exit of the tool effectively reduces burr formation by causing a shearing (Mode II) fracture at exit although care should be taken to avoid a gap being formed between the backing material and workpiece. A detailed review and suggestion of future trends in modeling of burr formation can be found in [30, 31]. Material properties of burrs have received some attention in studies of exit burrs during grinding of A2 tool steel showing that the burr is harder at the root than the base material or the rest of the burr due to quenching [32]. The properties of burrs formed in milling, and for machining where there is negligible heat build-up and in materials that cannot be hardened by quenching, are yet to be studied.

Burr formation in drilling with a backup material using a 3D model in the commercial FEA package ABAQUS-Explicit showed that the use of a bushing reduced burr size in drilling while the use of a solid backing material was not as effective [33]. The model can also be used to predict the drilling forces and torques and demonstrate that lower forces cause lower delamination and reduce the burr size. A study of burr formation of drilling through stacked sheets of aluminum resulted in the design of a spring loaded pad to prevent gap formation during drilling [34]. A model was developed based on Sofronas model for burr formation and predicts the trend of change in burr height with feed.

Burr Formation in Micromachining

There is no clear consensus of what size marks the transition from macroscale to microscale tools. Tools as large as 1 mm have been reported in micromachining literature [35] while tool manufactures include tools up to 2 mm in their micro-tool catalogs [36]. In this study, tools less than 1 mm are treated as microscale tools. Burr formation in microdrilling of materials with different grain structure indicates that single crystal materials show large burrs because of higher ductility while materials with large grain

size (few grains in the drilled area) have smaller burrs probably because of reduced ductility at the grain boundaries [37]. Another study showed that burr height in microdrilling of 304 stainless steel reduced with feed until a feed of 12 μm per revolution and then increased [38]. Burr height also increased with reduced exit angle and increased speed and tool wear (measured by the number of holes drilled by a particular tool).

A qualitative study using SEM images of burrs produced in micromilling of aluminum and copper indicated that burr size increases with feed and a lesser extent with depth of cut [39]. It was suggested that the tool initially compresses the material due to its finite radius and then begins to cut the material once the major cutting edge contacts the workpiece. Burrs are larger on the downmilling side because the material flow direction is towards the downmilling side. The entrance and exit burrs are larger than those at the macroscale in comparison to the groove width. Flat ended blind holes were milled in 304 stainless steel with a 254 micron tungsten carbide tool and the effect of cutting speed, feed and cutting edge radius on burr height was studied [3]. The comparatively larger burrs at the microscale than at the macroscale (with respect to feature size) is attributed to ploughing caused by the substantial size of the edge radius with respect to the feed per tooth. Burr height increases as feed per tooth increases. It also increases as cutting speed increases at higher feeds. At lower feeds (3.2 microns per tooth), the burr height reduces as speed increases. This reduction is explained by showing that at high speeds a built-up edge is formed on the tool that reduces wear of the tool and causes metal flow around the tool to become more laminar and results in a smaller chip height. As the ratio of axial feed to cutting edge radius increases, burr height increases and there is a sudden increase in burr height before the tool fails. Empirical equations were arrived at to relate burr height and tool life (described as number of holes drilled before tool breakage) with cutting speed and feed per tooth.

Another qualitative study was conducted on milling of grooves in aluminum with 40 μm laboratory manufactured, semicircular, zero rake angle endmilling tools and a

hypothesis was suggested that burrs are formed as material is plastically deformed to produce a ridge in front of the tool which fractures in the middle of the groove to form burr on either side [40]. If these fracture, thin feathery burrs are formed. In some cases the burrs formed on the downmilling side may be removed along with the chips. It was also noticed that at feeds greater that 5 μm/tooth, fracture does not occur. It is unclear whether in this case only plastic deformation was observed which would lead to tool breakage. While this study provides insight into burr formation mechanics at low feeds for a zero rake angle tool and highlights the distinct nature of burr formation in micromachining in comparison to marcoscale machining, it does not explain the dependence on burr height on feed. The study emphasizes the need for a quantitative and rigorous study of burr formation at the microscale for popular commercially available negative rake tools.

Micromachining differs from macroscale machining in that the chip thickness is comparable to the tool cutting edge radius resulting in increased ploughing and higher specific cutting energy at low uncut thickness values (size effect) [39, 40]. In cases where the cutting velocity is low, the tendency for built-up edge formation and ploughing increases. Another phenomenon noticed in micromachining is the minimum chip thickness effect, which is observed when the undeformed chip thickness (determined by the feed per tooth) is less than a critical value for the material. This effect is characterized by ploughing of material instead of chip formation via shear [41]. In slot/groove milling, the chip thickness varies from zero at tooth entry to a maximum at the center and then back to zero at exit. As a result, there is significant ploughing at tooth entry and exit. The increased tendency for ploughing due to the aforementioned causes results in the material being pushed over to form a rollover burr instead of forming a chip.

Burr Formation in Micromilling of Thin Foils

As discussed in the preceding sections, research has been conducted on the related field of drilling of sheets however, literature on micromachining of sheets and foils is sparse. The industrial convention, though not completely consistent is to label as foils material thinner than 0.8 mm [42]. A study of microdrilling of printed circuit boards suggested that burr size increased with feed. It was suggested that a hard backing material, reduced machining temperatures and forces would result in smaller burrs. An experimental study of 0.35 mm thick M-19 electric steel micromilled with 1.5 mm nominal diameter tools used peak burr height and percentage of edge that have burrs as metrics of the quality of the machined grooves [35]. It was found that higher feeds (7 μm/tooth) and speed (80,000 rpm) produce smaller burrs and this was attributed to reduced ploughing.

Milling of thin foils is often performed by sticking the foil to a backing material [43]. Hence, milling of these laminate structures differs from machining of homogeneous materials due to the possibility of delamination of the foil from the backing material. Moreover, the flow of chips is discontinuous at the foil-backing material interface. While shearing is the primary mode of material removal in homogeneous materials, it is expected that the foil would have a tendency to tear due to the machining forces. The review of published research presented above suggests that while the dependence of burr formation on machining parameters has been observed and explanations for some of these phenomena proffered, a more comprehensive understanding of burr formation in micromilling of thin foils is absent.

Machining of Nitinol

An experimental study of high speed milling of an $Ni_{50.6}Ti_{49.4}$ alloy indicated that increased cutting speed, lower depth of cut and lower feed per tooth reduced work hardening of the material [44]. However, beyond a cutting speed of 200 m/min tool flank

wear (measured using SEM images) increases. There is no significant change in phase during machining. The study concludes that the hardened layer induced in the material during high speed milling is shallower than that induced during conventional milling, EDM or laser machining. Another experimental study evaluated the performance of an austenitic and a martensitic NiTi alloy during lubricated conventional turning, drilling and deep hole drilling [45]. It was found that chip breakage and burr formation are significant challenges in machining NiTi due to its high ductility and that subsurface hardening is more evident in the martensitic alloy because of the lower plateau stress of twinned martensite. The influence of lubrication on subsurface hardening was not specified although it was stated that the use of lubricant reduces cutting forces and wear and it may be deduced that this would reduce hardening.

Micromachining of austenitic $Ni_{50.8}Ti_{49.2}$ with and without lubricant indicated that a feed of 12 μm/tooth, radial feed of 40 μm and depth of cut 10 μm provides the best tool life, surface and edge conditions [46]. It was reported that there is a strong tendency of adhesion of NiTi to the TiAlN coated solid carbide tool and that burr formation is unavoidable. A comparison between three axis and five axis milling with a chip-grid method to optimize chip load while machining $Ni_{50.2}Ti_{49.8}$ showed that a tool inclination of 50° was optimum [47]. Drill wear in deep hole drilling was primarily due to adhesion and wear was exacerbated in single lip drills due to asymmetric forces causing the drill to rub against the drill pad. Twist drills were reported as the preferred tool for drilling NiTi from wear considerations.

It can be concluded from these studies that while NiTi has typically been machined using EDM and laser machining, micromachining could result in faster material removal while inducing strain hardening to a lower depth. Burr formation during this process however, is a serious challenge and identifying machining process parameters which reduce burr formation as well as appropriate deburring techniques is important.

Abrasive Impregnated Brush Deburring

Analysis of abrasive impregnated brush deburring can be split into two areas: analysis of the brush characteristics (including interaction of workpiece with brush) and analysis of interaction of grits with workpiece. The research in each of these fields is presented in the subsequent sections.

Analysis of Brush Characteristics

An expression for stiffness of a filament of a wheel brush was derived based on large displacement analysis [48]. The filament was modeled as clamped at the hub and having zero moment at the other end. The equation for the moment in the beam was solved numerically, assuming that the length of the beam does not change (no axial deformation) to obtain the displacement of the filament, the force at the end of the filament, the release angle of the filament, the contact zone (the length along which the filament is in contact with the workpiece) and the total number of filaments in contact with the workpiece. Knowing the total number of filaments in contact with the workpiece and the stiffness of each filament, the force at the end of each filament and the deflection of each filament, the total stiffness of the brush was calculated. A rapid decline of the initial stiffness was noted for each of the response curves. At larger penetration depths, however, approximately constant brush stiffness was obtained. The deformed configuration of the filament was reported to be independent of the flexural rigidity EI (probably a consequence of the way the boundary conditions were specified); filament tip force, however, is noted to vary in direct proportion with the flexural rigidity.

An idealized geometry of a radial brush was created by calculating the total number of filaments in the brush [49]. Experiments were conducted to measure the normal and shear forces of the carbon steel brushes on a flat plate to calculate the coefficient of friction between the plate and the brush. An equation for the ratio of normal forces for the two brushes was derived based on the assumption that the normal forces are

proportional to the number of filaments in contact with the surface and the moment of inertia of the filaments. Normal force increased with penetration depth and speed. Shear force increased with penetration depth, but actually reduced at high speeds. A comparison was made with forces obtained from a mechanics model in [50] and [51]. The coefficient of dynamic friction between the brush and the surface was between 0.15 and 0.45. The actual geometry of the contact zone was found out experimentally and was to be symmetric about the center of the width of the brush. Converse to the assumption, the filaments bend out of the plane of the wheel brush and hence the penetration depth reduced. The effect of this non planar motion on the ratio of shear force and normal force was captured by a brush width distortion parameter.

The geometry of the contact area in wheel brushing was described using shape functions and measurements of the contact zone including brush distortion were made by brushing a flat polymeric plate [52]. The contact zone was assumed to be symmetric about the vertical axis. Nodal points were selected around the boundary of the profile and incomplete polynomial shape functions were used to interpolate the contact shape. At high speeds, the width distortion reduced. As penetration depth increased, the height of the contact zone increased.

A dynamic model for the bristles was formulated using a lumped viscoelastic model to capture the response of a nylon/SiC abrasive brush to a burr modeled as a step input and an ARMA model to capture the brush response to a random penetration [53]. The inputs to these models were found out experimentally for cases with and without material removal and the poles of the system obtained by both methods. Burr height reduction calculated by the ARMA model matched well with experimental results. There was a decay in the force over time due to reduction in burr height. The viscoelastic time constants for the brush were observed to decrease with speed. It was conceded that an understanding of the material removal mechanism does not exist although it is suggested that it was due to the interaction of the grits with the material.

A similar dynamic model of a honing tool was developed consisting of a wheel brush with abrasive spheres at the end [54]. The filament was discretized into linear rigid elements with torsion springs at the interfaces. Interface forces, moments and centrifugal forces were included and solved for the force exerted by the sphere on the interface, torque and maximum stress in the fibers. It was found that for low penetration the stress gradient at the tips was high and at low speeds the increase in torque with speed was low but no comparisons were made with experimental data. The need for an understanding of mechanics of material removal was emphasized.

The effect of centrifugal force on filament spacing and flaring for a cup brush was analyzed [55]. The filaments were again modeled as rigid links with torsion springs at the interface. The model predicted high stresses at the root of the bristles, retraction of the bristles and changes in bristle spacing that could lead to a non-planar working surface. A Lagrangian discretized model of rotating bristle contacting a flat rigid workpiece was used to study the initial impact of the filament on the workpiece and their subsequent contact mechanics [56]. The model predictions for average brush force were compared with experimental data and found to be in good agreement. It also predicts infinite forces at the tip during impact for a high level of discretization which suggests plastic deformation and fracture of the tips which is however not captured in the model. Five nondimensional parameters are suggested to capture the behavior of the bristle.

The viscoelastic equation from [53] was used to characterize the nylon/abrasive deburring process experimentally (Master Curves) [57] . The inverse time constant parameter was then used to calculate the brush feed along the edge required for complete burr removal. (Brush feed is analogous to the inverse of deburring time for a given section of a groove). The force variation along the contact region of a steel wheel brush was analyzed by gradually feeding the brush past a force sensor and measuring the force profile [58]. The force increased at contact and then remained constant. It then reduced gradually as the brush moved off the sensor. The contact forces between the filaments

and the workpiece were highest at the point of initial contact of the filaments with the workpiece. This force reduced gradually until the filaments lost contact with the workpiece. Plots of force gradient along the contact length were shown to indicate that the point of maximum gradient is close to entry of filaments. The population density of the filaments was maximum at the point of entry. Average coefficient of friction (ratio of shear force to normal force) was almost constant because a hard workpiece is used. Material removal depends on both maximum force magnitude and rake angle. Hence, the point of maximum material removal is closer to the middle of the contact region for lower brush speeds (< 3000 rpm) and not at the point of maximum force (entry region). However at higher speeds, the point of maximum material removal moves closer to the entry region. The reason for this shift was stated as unclear.

Analysis of Interaction of Grits with Workpiece

An optical microscope study was conducted on the effects of attack angle on the transition from rubbing to cutting with a single point carbide tool, lead workpieces under constant load and traverse velocity [59]. The mean pressure required to displace material and the coefficient of friction on the surface was evaluated by the Eldredge-Tabor method. The critical attack angle was found to be about 60° but takes place over a range of angles. Forces in these two regions were calculated using Merchant's equations for cutting and Bowden-Tabor's equation for ploughing. A case was made for mechanical abrasion as the mode of material removal in polishing [60]. The abrasive gets embedded in the cloth and scratches the surface. Factors that affect the material removal rate were identified as the force which is applied to contacting abrasive particles, the number of contacting abrasive particles, the shape of their contacting points, the critical attack angle for cutting, and the proportion of contacting points that are oriented with a favorable attack angle and the coefficient of friction between the specimen and the contacting points but a model was not attempted.

A review of fundamental research on the mechanics of friction with a brief outline on the major views of mechanics of wear and lubrication was presented [61]. It was suggested that friction is caused due to adhesion and ploughing, depends on the load and is independent of the size of the bodies. For purely plastic deformation, the area of contact is proportional to the load *w*, while for purely elastic deformation it is proportional to $w^{2/3}$. In reality it will be in between those two values.

The mechanics of material removal in polishing and lapping both in terms of mechanical and chemical effects was approached in terms of the interactions between the four components of the process, namely the lap, fluid, grits and workpiece as pairs and triplets [62]. It was proposed that if the loads are such that the yield stress is not exceeded during workpiece-grit interaction then only elastic deformation occurs while if it exceeds the yield stress then the material is either ploughed, forms a chip, forms a wedge or initiates fracture. Low penetration and high negative rake increased ploughing and hence thrust force. In the case of soft pads touching the workpiece, the contact area was proportional to the applied load and effective pressure at the contact junctions was constant. In general, in polishing increasing the concentration reduces the load per grit and the polishing rate was independent of grit concentration and size. For small grit size and low concentrations material removal was proportional to size and concentration. Large grits under low load tended to roll, reducing material removal. High concentration resulted in material removal being proportional to the load. In lapping very small particles (< 3 μm) removed material in the form of platelets instead of ribbons. Transition from cutting to ploughing depended on penetration depth and the ratio of penetration to contact radius but was independent of shear strength.

The only study of material removal during brushing studied short (< 4 inch) bristle brushes and developed an analytical equation for qualitative understanding (Eq. 1) where Z is the material removal rate, F_c is the tangential cutting force, V is the surface cutting speed, v_t is the specific cutting energy for the workpiece and C is a constant of

proportionality, but did not verify the equations experimentally [63]. While this is the only attempt to model material removal in brushing, it does not capture the effect of material properties and brushing parameters separately but lumps them into a proportionality constant and specific cutting energy and also lacks experimental verification. Centrifugal stiffening is factored in as a coefficient which is also left unquantified. It was found that rise in temperature (to about 150°C) reduces stiffness of the brush. Also, increasing brush pressure beyond 2.5 psi reduces material removal rate due to heating and out of plane deflection of bristles.

$$Z = \frac{CF_c^n V^m}{\upsilon_t} \quad \textbf{(1)}$$

From the preceding discussion it can be concluded that while there is a fairly large body of literature on brush dynamics, the need for an understanding of the mechanics of material removal is quite rudimentary while the need for such a study has been underscored often. The dynamic models do not take into consideration the initial contact force of the bristles while experiments suggest that the maximum force and hence, the maximum force would be at this point. Furthermore, these models require considerable experimentation to obtain the viscoelastic damping parameters required as inputs. A strong case can be made for the dominance of mechanical material removal during the abrasive impregnated brushing of metals over chemical phenomena and that the Hertzian 2/3rd power law can be used to model the interaction of the grit with the workpiece.

Biomedical Device Design and Analysis

As mentioned in Chapter 1, the knowledge of burr formation and deburring is applied to a biomedical device made from the shape memory NiTi alloy that is used in the surgical correction of Age-related Macular Degeneration (AMD). This section presents a review of the state of the art of treatment of this disease as well as a review of devices using thermal adhesion to manipulate tissue and modeling techniques for shape memory properties NiTi required to characterize the device.

Age Related Macular Degeneration

Age-related macular degeneration is commonly referred to as either “dry” or “wet”. Dry AMD or atrophic AMD (aAMD) occurs when there is a loss or attrition of the retinal pigment epithelium (RPE), Bruch's membrane, and the inner choroid (Figure 3). Wet AMD or exudative AMD (eAMD) leads to a more rapid decrease in macular function by the leakage or exudation of fluid from neovascularization (new blood vessel growth) originating in the choroid, and developing in the sub-retinal space. These blood vessels are fragile, may break or bleed, thus leading to photoreceptor damage and dysfunction along with scarring and inflammation. The RPE is a key monocellular layer under the retina and is responsible for transporting nutrients from the blood vessels in the choroid to the photoreceptors. In addition, the RPE is also responsible for transporting waste-products from the photoreceptors, re-processing the material, and moving the waste products away from the region via the choroidal circulation. Bruch's membrane is a thin, semi-permeable membrane that separates the RPE from the inner choroid. Therefore, damage to the RPE under the macula interferes with both the supply of nutrients to the macula, as well as waste-removal. The loss of both critical functions leads to clinical AMD.

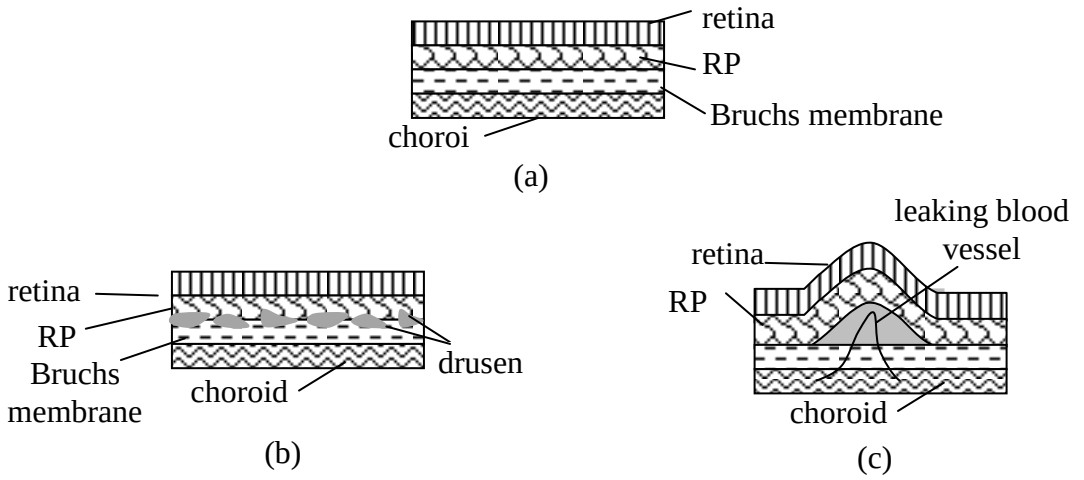

Figure 3: Cross section view of macular tissue (a) Normal eye (b) Dry AMD or aAMD (c) Wet AMD or eAMD

Wet AMD is currently treated using direct injections of anti-angiogenic medications, but this treatment is extremely expensive. The on-label use of current treatments costs approximately $2,000 per vial of drug plus the clinic, imaging, and injection fees. This therapy needs to be repeated monthly, and is estimated to cost the US economy about $10 billion annually [64]. No effective therapies are available for aAMD [65]. Finally, many eyes continue to deteriorate despite therapy and 20-30% do not respond to medical treatment. The proposed surgical correction of AMD offers a possibility of a treatment for both eAMD and aAMD [18, 66-68]. The procedure usually involves re-supplying the macula with healthy RPE-Bruchs-choroid using 3-port par plana vitrectomy techniques [69]. The damaged tissue under the macula is replaced with a healthy tissue. This graft typically originates from another portion of the eye although it could theoretically be derived from a human donor, a synthetic graft, or even from animal source. An objective of the surgical procedure is for the neurosensory retina and photoreceptors of the macular region to remain in their original position. Only the sub-retinal tissues are replaced. Details of the surgical technique can be found in [70].

Development of a mechanical device to support the delicate tissue avoids folding, injury, or loss of polarity of the translocated tissue [18]. In previous efforts, such a graft has been translocated using a spatula or with forceps. This often leads to damage and bleeding of the tissue [19]. Furthermore, studies have shown that the size of graft is limited by the size of the forceps used [18]. Therefore, we predict that the success of such a procedure would be increased by using a stable support structure that holds the tissue in its natural polarity and shape during translocation. The structure is also used to correctly orient the tissue under the fovea.

Shape Memory Effect

Shape memory structures require heat to transform them from a deformed shape to the shape that they have been taught. This transition occurs due to a diffusionless phase transformation occurring in the material. In a stress free, high temperature state, the structure consists of an austenitic phase. When the structure is deformed, the induced stresses cause a phase transformation to martensite. This process takes place by a process of twinning rather than by other modes of deformation such as slipping as long as the strains are below about 6 to 8%. Since the deformation mechanism is twinning, removal of the load causes the transformation back to austenite and the original, undeformed crystal structure to be regained. This phenomenon allows SMA materials to demonstrate the ability to recover from large strains (6-8%) and ability regain its undeformed shape.

The start temperature for austenite to form is referred to as A_s while the temperature at which the microstructure is completely austenite is referred to as A_f. Similarly, the temperature at which the material begins to transform to martensite is referred to as M_s while the temperature at which it is converted completely to martensite is referred to as M_f. In order to cause recovery of the trained shape, the structure needs to be heated beyond A_f. The difference between the start and end temperatures is typically

about 10^0C. Transformation from the deformed shape to the trained shape is achieved by heating the structure above A_f.

Shape memory alloys were discovered in the 1970s and models of the behavior of these materials have been studies since the 1980s [71, 72]. Tanaka developed a model describing the stress-strain behavior of SMA materials based on phase transformation kinetics of the material due to temperature and stress. Brinson and Lammering developed a one-dimensional finite element model for shape memory alloys and used it to calculate the stresses induced in simple structures such as rings and to find the frequency response of a composite structure embedded with SMA wires [73]. SMA structures have also been modeled using hyperelastic material models for rubber [74]. However, these models do not capture the temperature dependence of the material properties or the directionality of the loading (i.e. whether the material is being loaded or unloaded). Gong et al. modeled a superelastic stent in ABAQUS based on the model developed by Aurichio [75, 76]. Terriault et al. modeled a linear shape memory wire embedded in an aerofoil using a user defined material model algorithm in ANSYS [77]. This model based on the work of Müller and Xu [78] captures both temperature based effects as well as directionality of loading. The effect of temperature is captured by changing the material properties as a function of temperature. These properties are the elastic modulus of austenite (E_A), direct transformation modulus (E_{td}), martensite start transformation stress (σ_{Ms}), martensite finish transformation stress (σ_{Mf}) and austenite start transformation stress (σ_{As}). Three zones are defined in the model, namely, elastic, direct transformation and inverse transformation (Figure 4). The model identifies the direction of transformation based on the stress state in the prior iteration.

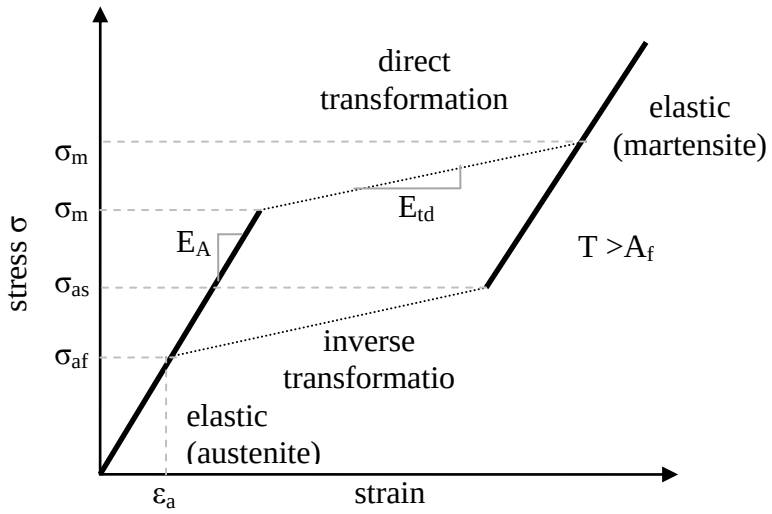

Figure 4: Three zones of model developed used by Terriault et al.

Thermal Adhesion

Thermal adhesion of tissue has been utilized in direct and indirect heat induced attachment and detachment (HIAD) devices [79, 80]. With direct HIAD, adhesion is achieved by passing high frequency AC through the tissue. Vankov et al. [79] measured the force and extension after adhesion of chicken tissue to a 50 µm diameter wire with direct HIAD and found it to be on the order of about 30 to 40 mg (300 to 400 µN). Tissue damage was limited to a 10 µm region around the electrode. With indirect HIAD, short DC pulses are applied to a molybdenum resistance element to cause it to stick to the tissue. Tissue damage due to this device was not evaluated. Knulst et al. [80] studied the amount of energy required for attachment and detachment of pieces of chicken tissue using an indirect HIAD with a 50 µm molybdenum wire.

The mechanism of adhesion between the metal and tissue is unclear. However, theories have been suggested to link the adhesion to hydrogen bonds, dipole interactions, Van der Waals forces and the presence of adhesive groups on denatured proteins [79-82]. These phenomena have been observed to take place when the electrode temperature is about 70°C. Tissue shrinkage has also been reported at temperatures between 55 and

65°C [83]. The bond between the tissue and metal is found to break down at about 100°C [84].

Thermal models of a normal eye and the response of the eye to laser radiation have been developed [85, 86]. A review of research on experiments and modeling of radiofrequency ablation for several different organs and tissues was conducted by Berjano [87]. Temperature rise and electric field for a ring electrode used for reshaping the cornea due to a short electric pulse has been studied [88]. It was seen that current density is the main determinant of tissue temperature rise and that there is a high current density at the edges of the electrode. There was also an increase in tissue temperature as the area of contact between the electrode and the cornea was reduced. Factors considered in the simulation were electrode thickness, diameter and conductivity. Dehydration of the tissue at ≈ 100°C was used as the criterion to evaluate lesion depth. In-vitro tests with radiofrequency resistive heating showed a lesion depth of about 360 μm in 20 seconds.

Summary

From the above discussion, the following can be concluded:

- While brush deburring has been successful and some of its aspects studied in detail at the macroscale, its applicability to the microscale has never been formally evaluated. This is piquant given that it has been suggested as the first process to be attempted while deburring microfeatures,
- Mechanics of burr formation in micromilling of thin foils and is significantly different from both macromilling and micromilling of bulk materials and understanding of this process is important for all materials but more so for NiTi due to its propensity to form burrs. However the present grasp of the subject is mostly speculative.
- While a large body of literature is present on brush dynamics, the need for understanding of the mechanics of material removal in abrasive

impregnated or assisted brush deburring is noted as an important and mostly unaddressed area of research. An experimentally verified model that captures the effect of material properties and brushing parameters would be a significant addition to the current knowledge in this field.

- There is a need for a minimal invasive device that facilitates tissue translocation for surgical correction of Age-related Macular Degeneration.
- Finite element analysis with a bilinear kinematic model is a potential method of analyzing unidirectionally loaded shape memory devices.

These potential areas of significant contribution to the current knowledge motivate the current study and are addressed in the following chapters. In the next chapter abrasive slurry assisted brush deburring is experimentally evaluated for its applicability to micromachined grooves in bulk materials.

CHAPTER 3

ABRASIVE SLURRY ASSISTED DEBURRING

In this chapter, we seek to deburring rate in abrasive assisted brush deburring is experimentally characterized as a function of the process parameters. The process parameters considered in this study are the abrasive grit size, abrasive type and spindle speed. A previous study of the process focused on the time taken for complete deburring of micromilled grooves [89]. Since the time for complete deburring varies with process parameters, their effect on surface finish and change in groove depth is confounded with deburring time. This difficulty is overcome in the current study by keeping the deburring time constant. Moreover, the present study takes into account the effect of initial burr height on the deburring rate and examines two different workpiece materials.

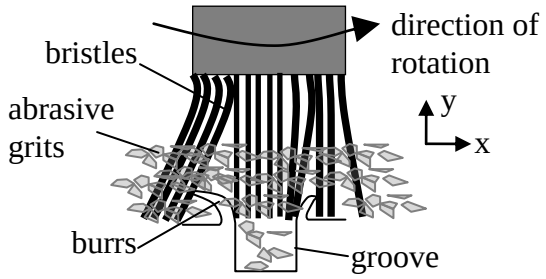

Figure 5: Schematic of abrasive assisted brush deburring process. Brush reciprocation in z direction.

Experiment Design

A full factorial experiment was conducted to quantify the effects of abrasive grit type, size and spindle speed. The brush was rotated at a spindle speed that is limited at the lower end by machine capability and the desired burr removal rate. It is limited at the higher end by flaring of the bristles, which also reduces burr removal rate and damages the brush. When abrasives are used, high rotational speeds result in the particles being

swept away from the area where burrs need to be removed. The lowest spindle speed possible in the setup used is 5,000 rpm, while the highest speed recommended by the brush manufacturer is 15,000 rpm. Hence, the three speeds chosen for the experiment were 5,000 rpm, 10,000 rpm and 15,000 rpm.

Abrasive slurry was applied to the groove to increase the deburring rate. Commonly used abrasives are diamond, silicon carbide and alumina. Alumina is usually used for very small amounts of material removal in polishing operations [90]. Diamond slurries have long life and usually yield a much better surface finish. However, they are expensive. In this study, silicon carbide (Black SiC, Washington Mills) and diamond (Advanced Abrasives Corp.) abrasive particles were used to assist the brushing process. Two nominal grit sizes (1.25 μm and 3 μm) were considered for the process. The slurry consisted of one part by weight of abrasive powder in 10 parts by weight of de-ionized water. This ensured that the material removal is by purely mechanical means and not by chemical action. The de-ionized water also helps to cool the brush and extend brush life.

Burr properties and removal rates vary with the hardness of the work material. Hence, burr removal in copper alloy 110 (99.9% Cu, 95 HV) and A2 tool steel (215 HV) are studied in this paper. All experiments were replicated three times.

The abrasives used for deburring were characterized in a dynamic light scattering system (Zetasizer Nano, Malvern Instruments) yielding the measurements listed in Table 1. The mean sizes are close to the specified grit sizes. Polydispersity index measures the dispersion of particle sizes. Values above 0.7 indicate a broad distribution of particle sizes. Note that larger particles have a much higher dispersion than smaller particles. The zeta potential measures the likelihood of the grits agglomerating. Potentials whose absolute values are above 30 mV are considered stable and hence less likely to agglomerate. Diamond shows much better stability than SiC. The SiC grits exhibit a mild tendency to agglomerate.

The normal force applied by the brush was limited at the lower end by very low burr removal rates leading to long process times. It was also limited at the higher end by excessive buckling of the nylon bristles of the brush and damage to the workpiece. The buckling of the bristles causes the sides of the bristles instead of their ends to come into contact with the workpiece. A prior study [89] indicated that deburring time is more sensitive to changes in speed than changes in the normal load. Hence, in this study, the normal load was fixed at 1N.

Table 2: Characteristics of abrasive grits used for deburring

	SiC		**Diamond**	
	3µm	**1.25µm**	**3µm**	**1µm**
Zeta potential (mV)	-29.8	-26	-31.1	-35.5
Mean size (µm)	2.93	1.08	2.16	1.22
Polydispersity Index	0.628	0.244	0.698	0.305

Experimental Procedure

Sample Preparation

Micro-grooves were milled using a micro milling machine designed and built in-house and are shown schematically in Figure 6a. The artifact to be deburred consists of a 5 mm long groove that is 50 µm deep and is cut in a single pass by a 500 µm diameter, two flute carbide end mill (PMT, TR-2-0200-S) spun at 60,000 rpm with a feed rate of 500 mm/minute. The entry and exit portions of the groove and associated burrs are affected by tool entry and exit dynamics. Hence, entry and exit sections are provided in the grooves to allow the 5 mm section being studied to remain unaffected by entry and exit transients. Since groove depth can be affected by workpiece positioning errors and surface irregularities, the grooves were produced on a pre-milled reference surface.

The burr removal rate was evaluated by partially deburring the grooves for a fixed time. The difference in burr height before and after deburring was then calculated. Since

the deburring time is fixed, the difference in burr height can be used to calculate the burr reduction rate.

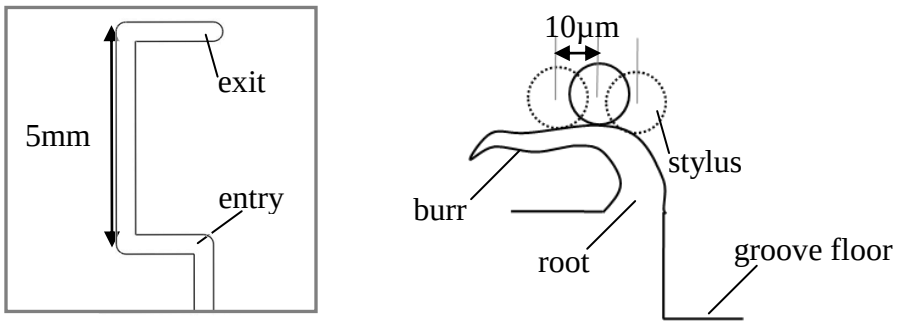

Figure 6: (a) Top view of artifact to be deburred (b) Burr measurement

Abrasive assisted brush deburring is a fairly quick process. Hence, if the burrs produced in micro milling are small, they will be removed in a very short time and the difference in burr height reduction due to change in the process parameters cannot be easily measured. In order to accentuate the effects of these parameters, it was necessary to produce fairly large burrs. Burr height generally increases with tool wear and feed [3, 21]. Hence, the tool used for machining the reference surface was also used for machining the grooves at a high feed, thus wearing-in the tool. This resulted in much larger burrs than would be seen if a new tool was used at feeds recommended by the tool manufacturer.

Burr Measurement

Nominally, the calculation of burr removal rate requires the volume of the burr to be known. Typical approaches for burr measurement include optical, tactile and destructive methods [91]. Optical methods include the volume under the rollover burrs commonly seen in micromilling [40], leading to an error in the calculated volume. Tactile measurement devices give line traces of the surface and hence, cannot be used to calculate the burr volume but can quantify burr height. Destructive methods such as

sectioning [91], makes subsequent deburring impossible. Hence, there is no reliable method to calculate burr volume. Material removal rate in macroscale deburring has been calculated by measuring the weight of the sample before and after deburring [92]. The abrasive assisted brush deburring process also involves a polishing process. Hence, measuring the sample weight yields a measure of the total material removed by polishing and deburring.

A metric often used to characterize burr size [21, 93] and burr reduction rate [53, 94] is the burr height, which can be measured accurately by a profilometer or a laser scanner either in-process or off-line. This feedback can then be used in the subsequent deburring operation to predict deburring time. Hence, in this study, deburring rate has been characterized by the change in burr height during the operation.

The initial burr height in turn depends on tool wear. Consequently, there will be some variation in burr height from the first groove to the last groove machined using the same tool. Hence, subsequent grooves in the order of machining are deburred at different spindle speeds. Thus, any variation in burr height due to tool wear is distributed more or less equally over all speeds. Moreover, the model used to evaluate the effect of speed separates the effects of burr height from the effects of spindle speed.

Burr height is measured before and after deburring using a surface profilometer (Taylor-Hobson, Form Talysurf) with a 397 μm diameter spherical sapphire stylus. The large size of the stylus tip makes it easier to pick out the high points of the burr in a small region. The stylus was aligned with the length of the groove and positioned on top of the burr using a microscope under 50X magnification.

The burr height at any point along the groove length varies in the direction of the groove width. Hence, in order to find the highest point of the burr at any point along the length of the groove, three traces offset 10 μm from each other in the direction of the groove width were taken. The burr height at any point was taken as the highest value for that point among the three scans (see Figure 6b). Burr heights were measured on both the

upmilling and downmilling sides of the groove. Similarly, groove depth was measured before and after deburring with the same profilometer but with a 2 μm effective diameter diamond stylus tip.

Deburring

The micromilled grooves were deburred using a nylon end brush (Dremel, Bristle brush 405) mounted in a Dremel spindle (Dremel 4000). The brush had a diameter of 3.5 mm and 50 μm diameter bristles. It was positioned above the artifact to be deburred and spun at the required speed and reciprocated along the groove length at 300 mm/min. A few drops of abrasive slurry were applied on the artifact. The normal force exerted by the brush was kept constant at 1 N using a counterbalance weight system. The spindle is free to move vertically in a lubricated bushing. The spindle weight is balanced by the counterbalance and the normal force between the workpiece and the brush. Hence, the normal force between the brush and the surface can be controlled by changing the counterbalance weight. The normal force was monitored using a piezoelectric force platform (Kistler MiniDyn 9256C2).

Deburring experiments were carried out for a constant duration of 65 seconds in all experiments reported here. This duration was selected such that deburring was stopped before complete burr removal, thus allowing for the estimation of burr height reduction. The burr reduction rate was calculated by dividing the burr height reduction by the deburring time. The effects of spindle speed, grit size and abrasive type on burr height reduction rate were then evaluated.

Experimental Results

Burr Types

Figure 7 and Figure 8 shows the typical burrs observed in micromilling of tool steel and copper respectively. The burr size seen in copper is much larger than that seen

in tool steel because copper is more ductile [20]. The burrs in the grooves can be categorized as tear and Poisson burrs. Tear burrs are caused when material tears apart instead of being sheared by the tool [20]. Poisson burrs form where the material is plastically ploughed up near the edge instead of being sheared to form a chip. Typically, in both materials the burr is a combination of tear and Poisson burrs. The tear burr is attached to the groove edge at the burr root. At the root, the burr is formed by material being ploughed by the tool edge. As a result, the root is much thicker than the rest of the burr and also the toughest to remove. The root region gets exposed during deburring and can be seen clearly on partially deburred edges. Since tool steel is harder and less ductile than copper, the tool steel burrs have a much more well defined shape than the copper burrs. It can also be seen that burrs on the downmilling side of the groove are larger than burrs on the upmilling side. This is because the torn burr gets cut on the upmilling side and is swept towards the downmilling side. On the upmilling side, the burrs are mostly of the Poisson type, although a few small tear burrs are also present.

Visual Inspection of Deburred Grooves

Figure 7 shows images of a groove in tool steel deburred with 3 μm SiC grits at 15 krpm for 65 seconds. It can be seen that burrs on the down milling side are larger than on the up milling side. The burrs are feathery with a mostly thin cross section except at the root. It can be seen that machining marks on the top surface of the groove have been removed by the deburring process. However, machining marks on the groove base are still present after deburring. Note that, prior to imaging, any residual abrasives on the deburred surfaces were removed using isopropyl alcohol and a light brush (Crayola 3515).

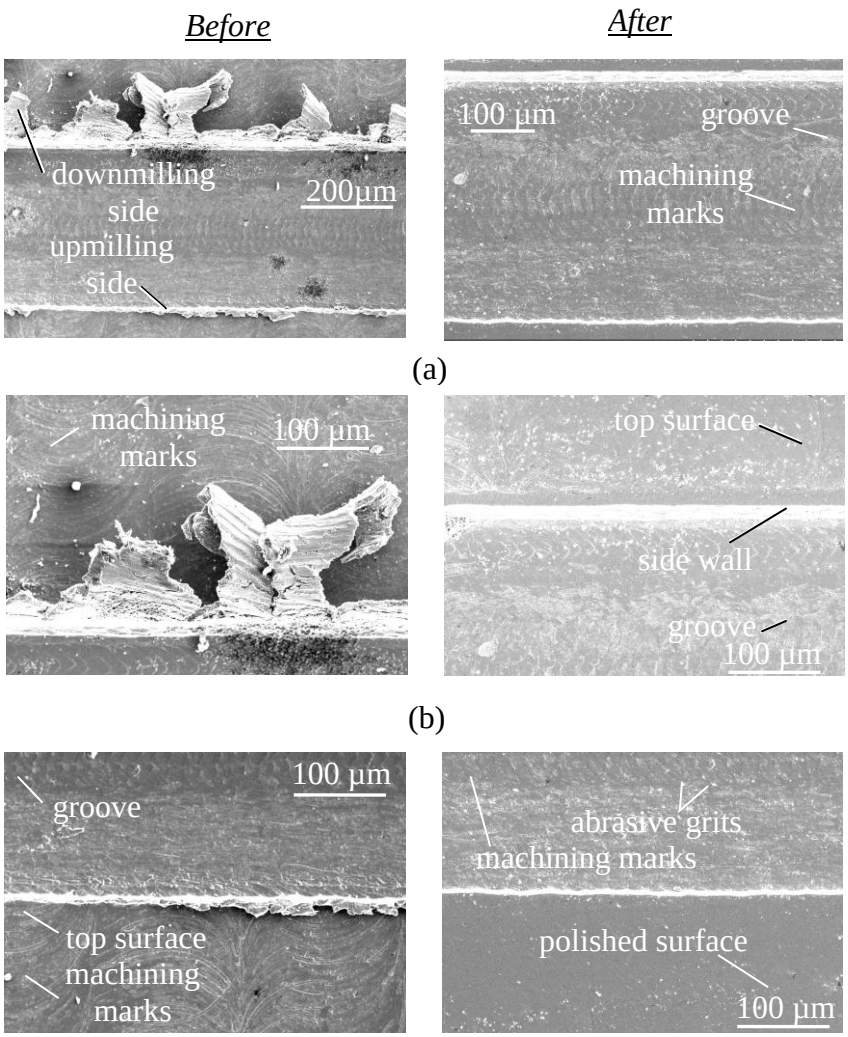

Figure 7: Burrs in milling of A2 tool steel before and after deburring with 3 µm SiC grits at 15,000 rpm (a) both sides of groove (b) down milling side (c) up milling side

Figure 8 shows a groove in copper before and after deburring with 3µm SiC grits at 15krpm rpm for 65 seconds. A much larger residual burr is seen in this case because the initial burrs were fairly large. The downmilling side burrs have a smoother surface after deburring. This suggests that while the slender burrs are removed by breaking or tearing, thicker burrs and burr roots are gradually removed by abrasive action of the grits. The upmilling side burrs are removed quickly due to their slender shape to give a well

defined edge. Machining marks have been removed from the top and bottom surfaces of the groove. However, unlike tool steel, scratch marks on the surface due to action of the abrasive grits are much more pronounced. This is due to the fact that copper is softer than tool steel.

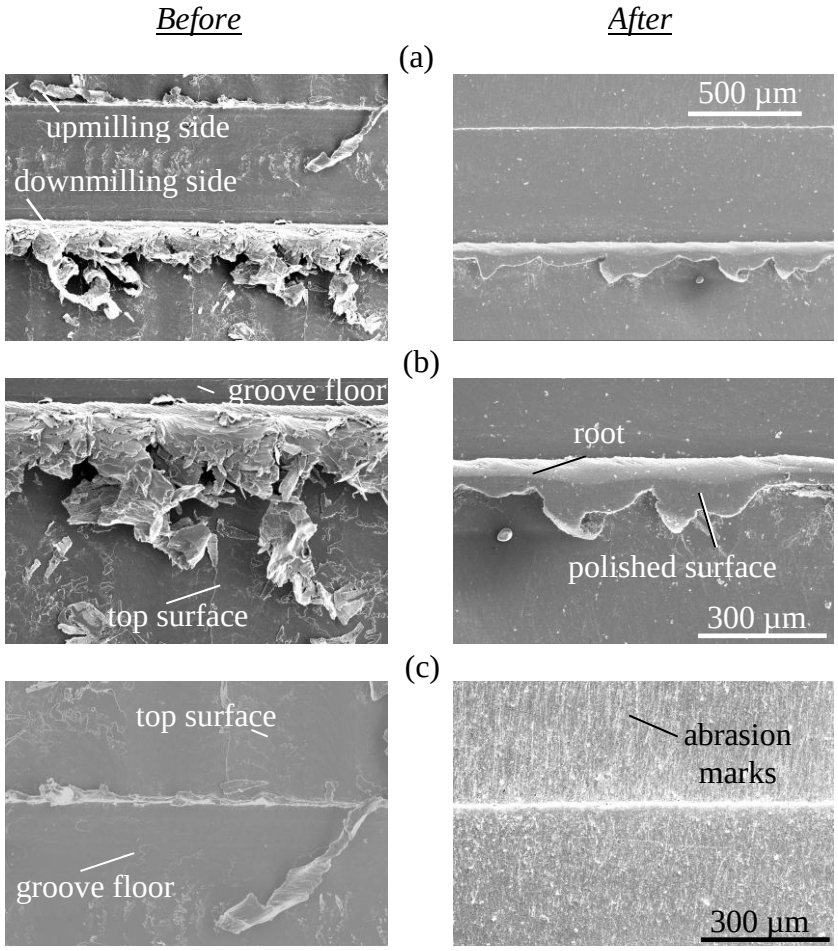

Figure 8: Burrs in milling of copper before and after deburring with 3 µm SiC grits at 15,000 rpm (a) both sides (b) down milling side (c) up milling side

Figure 9 a shows an unbrushed area next to the burrs (Region I). This can be explained by noting that in the presence of a large burr, the bristle follows the trajectory shown in Figure 9 c. When it contacts the burr it bends and travels along the top of the burr. When the tip of the bristle reaches the end of the burr it is released and follows a curved path until it contacts the workpiece again at the start of Region II. Hence, there is

a small region near the burr that is shielded from action of the abrasives embedded in the bristles. A consequence of this is that the unshielded region gets abraded more than the shielded region. This causes a depression in the top surface from the groove edge towards the outer edge of the brushed area. This incline can be seen in a fully deburred groove shown in Figure 9 b. It is also seen that Region II is abraded more than Region III edge although both surfaces are exposed to abrasives for the same time. The bristle in Figure 9 b behaves like a bent cantilever spring that is released from the burr. It is hypothesized that the excessive abrasion in the unshielded region is due to the impact of the bristles against the surface after being released from the burr. For the section shown in Figure 9 b, bristle impact causes a depression about 5 μm in depth.

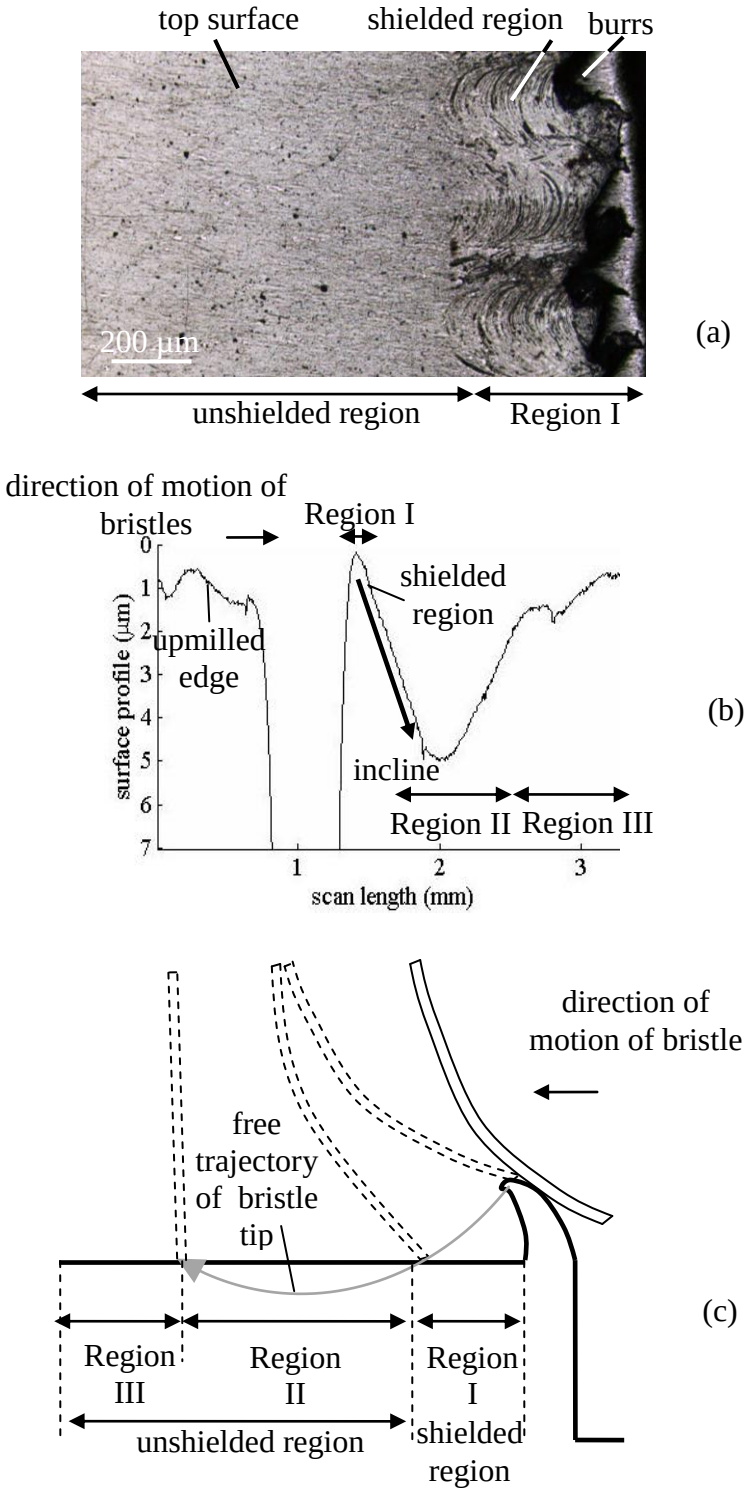

Figure 9: Effect of shielding of surface by burrs. (a) Image of surface (b) Trace of surface of a completely deburred groove (c) Schematic of motion of brush

Burr Reduction Rate

A trace of a downmilled tool steel edge deburred with 3μm SiC grits and 15 krpm spindle speed is shown in Figure 10. It can be seen that there is significant reduction in burr height in a very short time. While the initial burr height varies significantly, the height of the residual burr is fairly constant. Hence, for the same deburring time, the height reduction is greater for tall burrs than for short burrs. Hence, it is inferred from the plot that burr height reduction is proportional to initial burr height.

This behavior can be explained by examining the shape of the burrs shown in Figure 7. The burrs in A2 tool steel tend to be slender and tear-off or break upon contact with the bristles and/or abrasive leaving only the burr root behind. If the burr root height is nearly the same for both large and small burrs, then when a tall burr is broken by the combined action of the bristles and abrasives it results in a larger burr height reduction than when a small burr breaks. Hence, tall burrs show a higher burr reduction rate than short burrs. However, it is expected that this trend will change when the burr root is removed. In this case, the deburring rate will be proportional to the area of the root in contact with the brush.

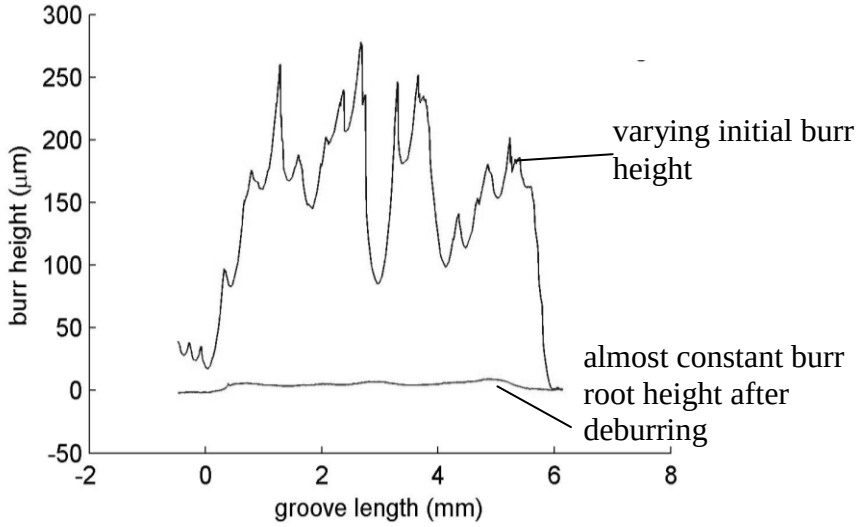

Figure 10: Sample trace of groove edge before and after deburring of A2 tool steel at 15krpm with 3 μm SiC grits

These findings are consistent with the work of other researchers [95] who suggest that there are two types of burr removal mechanisms: extensive yielding (Type 1) and abrasive wear (Type II). Extensive yielding occurs for thin sheet-like burrs that bend under the action of the deburring force and undergo failure at the root when the stress exceeds the failure stress of the burr material. For an average pressure P_0 acting on a burr of height x, thickness t_b and inclined to the reference surface at an angle θ, the stress σ generated at the root during Type 1 mechanism is given by Eq. 2. It can be seen that the stress is proportional to the burr height x when all other factors are constant. For Type II mechanism, it is suggested in [95] that the burr root material is plastically deformed without any material removal by stress concentration beyond yield. The abrasion marks on the surface of the material seen in Figure 7 and Figure 8 however seem to suggest that material is removed by chip formation. In this case, the proportionality between burr removal rate and initial burr height will not hold. Furthermore, it has been observed in the present study that removal of sheet like burrs occurs due to mode I and III fatigue fracture at the burr root.

$$\sigma = \frac{P_0 t_b x^2}{c^2} sin\,\theta \quad (2)$$

Statistical Model for Burr Reduction Rate

A quantitative evaluation of deburring speed can be obtained by fitting a linear regression model to the burr reduction rate y in µm/min. It is to be noted that this is by no means a 'model' in the sense of a physical explanation based on first principles but rather a 'regression model' in the sense of a statistical description of the effect of factors that would be expected to affect burr reduction rate. The factors in the statistical model given by Eq. 3 are the initial burr height x in µm, spindle speed N in krpm, abrasive grit size a in µm and abrasive grit type b [96]. The effect of grit type is captured by setting b to 0 if SiC grits are used and to 1 if diamond grits are used. Since the burr height reduction rate at every point along the groove edge depends on the initial burr height at that location and

the initial burr height cannot be chosen *apriori*, the initial burr height is a covariate for burr height reduction rate.

$$y = \alpha_0 + \alpha_1 x + \alpha_2 N + \alpha_3 a + \alpha_4 b + \alpha_5 N{\cdot}a + \alpha_6 N{\cdot}b + \alpha_7 a{\cdot}b + \epsilon \quad \textbf{(3)}$$

A comparison between the regression fit to the experimental data for deburring of A2 tool steel with 3µm SiC abrasives at 15krpm is shown in Figure 11 a. An almost linear dependence of burr reduction rate on the initial burr height can be observed. A cursory look at Figure 11 may suggest that the model does not fit the data accurately. However, note that the linear model is fitted to the data for the entire experiment design while the 2D plot in Figure 11 allows for only one subset of the data. The fitted equation has an R^2 value of 0.76. This value is low probably due to the uncontrolled nature of the free abrasives based process. A possible remedy to this problem is to use abrasive impregnated brushes for better process control.

The regression analysis in Table 3 indentifies initial burr height *x*, brush rotational speed *N* and grit type *b* to be statistically significant at a 10% level. Similar results are presented for copper in Table 4. It is interesting to note that the coefficient of the initial burr height α_1 is about 0.5 for both copper and tool steel. This is explained by the typical shape of the burrs, which tend to be thick at the root and thin away from the root. Therefore, they are more prone to bend and/or break right above the root. The value of the coefficient α_1 seems to suggest that the burr either breaks or bends at about half its initial height. The analysis also indicates that diamond abrasives have a higher burr reduction rate than SiC. Changing from SiC to diamond grits causes an increase in deburring rate of about 13µm/min in tool steel and of about 19µm/min in copper. This can be explained by noting that diamond grits are harder than SiC grits and maintain their sharpness longer than SiC.

Table 3: Coefficients for linear regression model for burr reduction rate for tool steel

	Symbol	Coefficients	p-value
Intercept	α_0	-7.68	0.28
Initial burr height (µm)	α_1	0.49	0
Speed (krpm)	α_2	1.02	0.1
Size (µm)	α_3	-1.54	0.59
Type (SiC=0, Dia=1)	α_4	13.05	0.05
Speed*Size	α_5	0.3	0.23
Speed*Type	α_6	-0.79	0.11
Size*Type	α_7	0.03	0.99

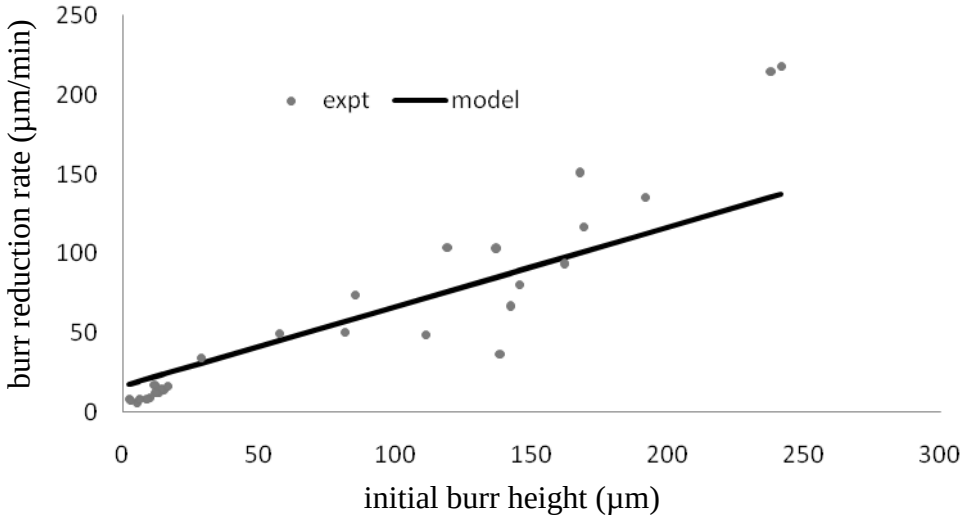

(a)

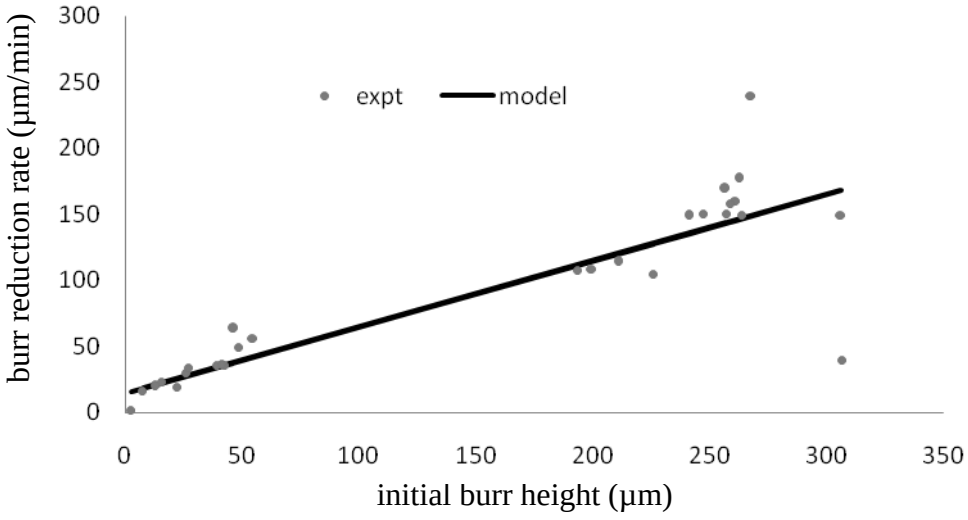

(b)

Figure 11: Burr height reduction rate as a function of initial burr height for deburring at 15krpm with 3 µm SiC grits (a) A2 tool steel (b) copper

Table 4: Linear regression model coefficients for burr reduction rate in copper

	Symbol	Coefficients	p-value
Intercept	α_0	-41.89	0
Initial burr height (μm)	α_1	0.53	0
Speed(krpm)	α_2	2.43	0.03
Size (μm)	α_3	4.28	0.42
Type (SiC=0, Dia=1)	α_4	19.34	0.12
Speed*Size	α_5	0.17	0.7
Speed*Type	α_6	1.04	0.26
Size*Type	α_7	1.81	0.64

The deburring rate also increases with speed as indicated by the positive coefficient α_2. A higher brush rotational speed implies a higher number of passes of the brush over the burr per unit time for a constant feed along the length of the groove. This implies a higher number of passes of the abrasives on the burr and hence a higher burr reduction rate. This increase in material removal sufficiently overcomes any reduction in material removal due to scattering of the grits by the centrifugal forces. In polishing 90% material removal is assumed to come from two body interaction and only 10% from three body interaction [97]. Hence, material removal is assumed to occur due to abrasives embedded in the bristles (Figure 12). The centrifugal forces are not strong enough to disengage the grits embedded in the bristles as observed from images of the bristles after deburring. Furthermore, the rotational kinetic energy of the grits should be high enough to overcome the resistance offered by the densely packed bristles. Since speed and type are significant, for tool steel the speed-type interaction term is also indicated as being slightly significant.

Models used for polishing may be applied to analyze abrasive assisted brush deburring since both are free abrasive processes that use a soft backing media. It has been suggested in [60] that in polishing involving material removal (i.e. chip formation instead of bulk plastic flow), the Mulhearn model [97] used for polishing with emery paper may apply, which suggests that the material removal rate is proportional to the depth of

penetration of the abrasive. A similar microcutting model [98] based on Archard's wear equation is shown in Eq. 4, which shows that the material removal rate $\frac{dV}{dt}$ is proportional to the relative velocity v_r between the grit and the workpiece (L is the load on the abrasives, H is the hardness of the workpiece, and k_w is a constant). This is in agreement with the experimental results presented in the present study. It is also suggested in [98] that the depth of penetration is proportional to hardness of the grit. Based on Mulhearn's model, increased penetration would also mean higher material removal rate, which supports the findings in the present study that the harder diamond grits yield a higher burr reduction rate than SiC.

$$\frac{dV}{dt} = \frac{k_w L v_r}{H} \quad \textbf{(4)}$$

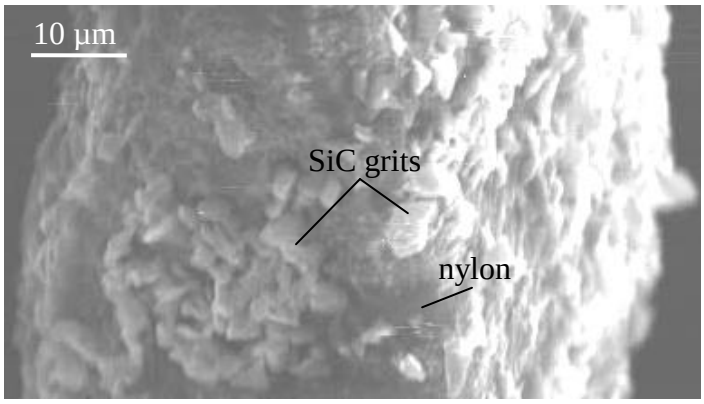

Figure 12: SEM image of a nylon bristle with 3µm SiC abrasive grits embedded in it

It is surprising to note that the effect of grit size is not very significant. While this warrants further investigation, one probable explanation is that for a constant grit concentration by mass, smaller grits would have a larger number of abrasives in contact with the workpiece. However, larger grits also remove more material per pass for similar indentation depth. It has been shown that abrasion rate in polishing is independent of grit size up to a critical grit size below which abrasion rate is proportional to grit size [97]. For the experiments in [97] the critical value was 50µm. However, the load in this case

was much higher than in the present study at (about 5N with SiC abrasives paper on a cold-drawn steel workpiece). Another possibility for the insignificance of grit size could be the narrow range of sizes used in the experiment. Note that a wider range of abrasive grits sizes cannot be used in this study due to excessive damage caused to the micro-scale feature by larger grit sizes under the deburring conditions used. It has been observed that 6 μm diamond grits can cause over 50% reduction in the groove depth, which is clearly undesirable.

A comparison between the regression model coefficients for tool steel and copper shows that the coefficients for copper are much higher than tool steel for all the factors. The effect of speed is much more pronounced in copper as indicated by the much lower p-value for copper. The higher sensitivity of copper to the deburring parameters is attributed to the lower hardness of copper. A regression fit for only the significant factors is performed on the data and the resulting equations are shown in Eq. 5 for tool steel and Eq. 6 for copper. The speed-type interaction factor has been retained for copper for the sake of consistency. Surface roughness in all cases improves by at least 100 nm and the mean change in depth is usually about 2 μm with a maximum of 4 μm for 3 μm diamond abrasives used on a copper workpiece at 15 krpm.

$$y = -10.45 + 0.49\,x + 1.62\,N + 13.04\,b - 0.79N{\cdot}b + \epsilon \quad (\mathbf{5})$$

$$y = -33.72 + 0.54\,x + 2.78\,N + 22.86\,b + 1.04\,N{\cdot}b + \epsilon \quad (\mathbf{6})$$

Verification

The deburring rate predicted by the model in Eq. 3 is verified experimentally for tool steel and copper. The conditions chosen for this experiment are 3μm SiC grits with a spindle speed of 15krpm. The deburring rate for these conditions is given by Eq. 5 for tool steel and Eq. 6 for copper. A trace of the burr height for a groove is taken and the time *t* in minutes required for complete deburring of the edge is obtained by dividing the

burr height *x* by the deburring rate as shown in Eq. 7 and 8. The grooves are deburred for the highest value of time obtained from these equations. For tool steel, this time comes to be 107 seconds while for copper it is 81 seconds. Note that even though the burr reduction rate *y* is always proportional to the initial burr height *x*, deburring time *t* may have a positive or negative exponential relationship with initial burr height depending on the values of the coefficients in the model. However, in both cases, the quantity of interest is the maximum time required to deburr a particular edge i.e. the maximum value of *t* from Eqs. 7 or 8 given the values of *x* along the edge.

$$t = \frac{x}{-10.45 + 0.5\,x + 24.3} \quad \textbf{(7)}$$

$$t = \frac{x}{-33.72 + 0.54\,x + 41.7} \quad \textbf{(8)}$$

The burr height before and after deburring is shown in Figure 13 for the downmilling side of the groove, which is generally characterized by larger burrs. It can be seen that most of the groove has been completely deburred. There is a significant residual burr at the beginning and end of the groove where the tool rounds the corner of the entry and exit section (see Fig. 2a). The model drastically underestimates the time taken to deburr this region (Figure 13a and b). This can be explained by the fact that the portion of the burr at the corners is heavily strain hardened and hence the root of the burr for this region is much thicker than the straight portion of the groove. In calculating the coefficients of the model, about 80% of the data comes from the straight portion of the groove instead of the corner. Hence, the model predicts the time for deburring the straight portion of the groove much better than the corners. Unlike tool steel, the copper specimen shows an almost uniform and complete removal of the burrs. Some small residual burrs of the order of 3μm are visible at the ends of the groove for reasons similar to those discussed for tool steel.

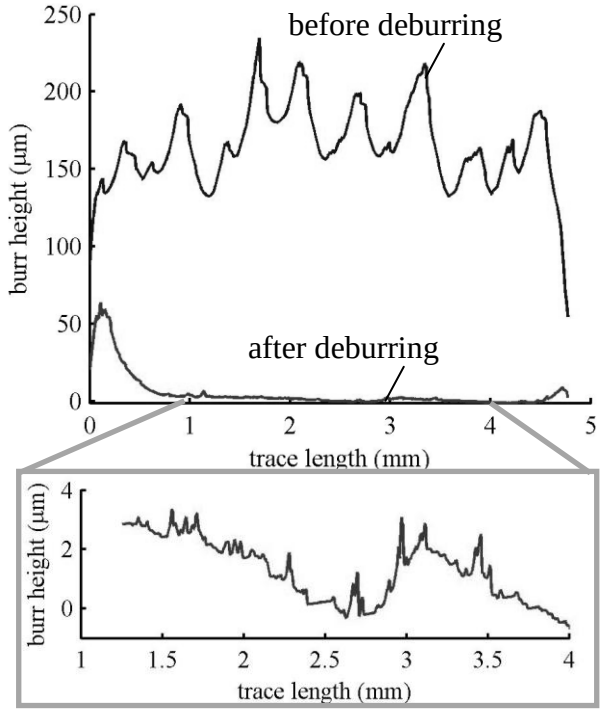

(a)

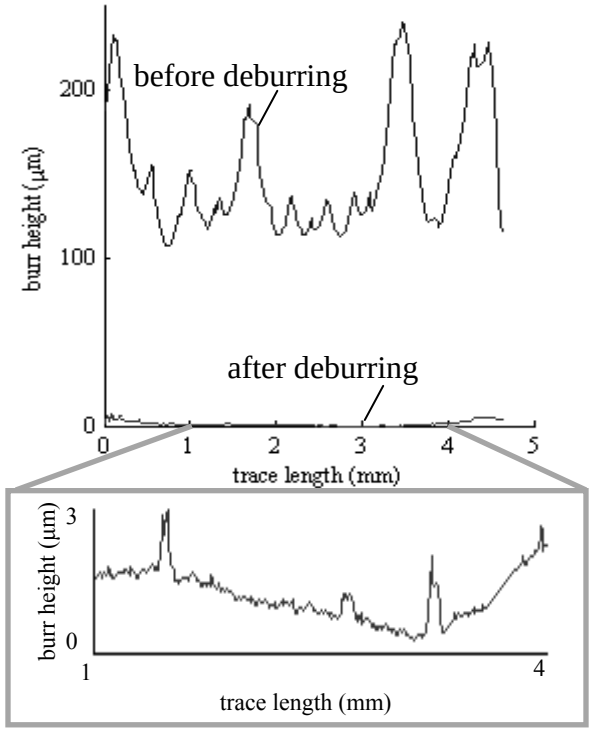

(b)

Figure 13: Verification of model: Full deburring with 3 µm SiC grits at 15krpm for predicted time. (a) burr height before and after deburring for tool steel (b) burr height before and after deburring for copper

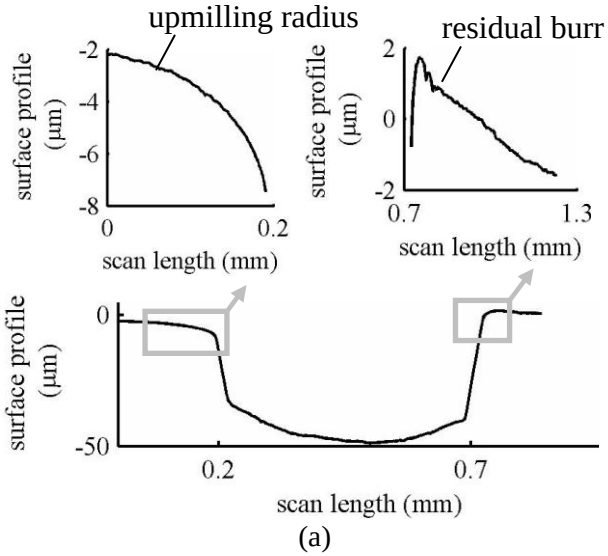

(a)

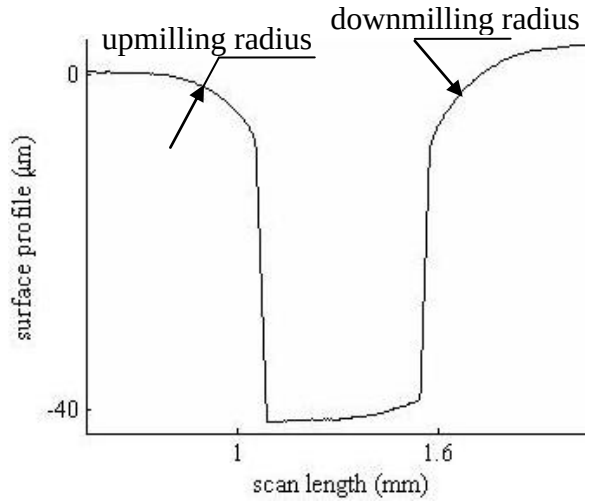

(b)

Figure 14: Verification of model: Edge condition after full deburring with 3 μm SiC grits at 15krpm for predicted time. (a) tool steel groove cross section profile after deburring (b) copper groove cross section profile after deburring

Note that the straight portion of the groove lies between 1 and 4 mm of the trace along the groove edge. This portion is almost completely deburred. Table 5 summarizes the characteristics of the burrs in this region before and after deburring. It can be seen that there are a few residual burrs in this region with a maximum height of about 3.5 μm for tool steel (Figure 14 a and b). Thus, the model for tool steel slightly underestimates

the burr reduction rate in this region. This is due to the fact that the burr root is much more difficult to remove than the feathery burr. It is interesting to note that even though the burr root was not explicitly considered by the model, most of the root has been removed (the standard deviation of the edge height is about 1μm). The edge condition after deburring for copper in the straight portion (between 1 and 4 mm) of the groove length has undulations of the order of a few microns which is about half the size of the abrasive grit used for deburring and may be because of abrasive marks. Both copper and tool steel show a slight dip in the profile towards the center due to less strained material and smaller burrs towards the center. SEM images scan of the groove are shown in Figure 15. The burrs in copper have been completely removed from both edges. Irregularities along the edge are mostly due to irregularities along the wall of the groove. The mean change in groove depth is 1.3 μm for tool steel and 3.4 for copper.

Table 5: Burr characteristics for region between 1 and 4 mm of trace length

	tool steel		**copper**	
	before	**after**	**before**	**after**
mean (μm)	173	1.3	143	1.24
standard dev. (μm)	23.6	1.1	31.1	0.6
max (μm)	234.5	3.5	239.6	3.04

As mentioned earlier, the brush is much larger than the groove and the burrs on the downmilling side are larger than on the up milling side. Hence, the upmilling side is deburred for a longer period than required. The edge radius was measured by taking four profilometer traces across the groove width (Figure 13 c and d) and the results are summarized in Table 6.

The residual burr size was measured from the zero datum, which is the level of the unbrushed region. The surface to the right of the residual burr drops below this datum because of material removal from the top surface as discussed earlier (Figure 9). It can be seen from Figure 15 that the radius is about 6 μm and is fairly constant. The maximum initial burr height on this edge is about 90 μm, which gives a predicted deburring time of

60 seconds. The groove was deburred for 132 seconds. Hence, in the remaining 72 seconds, the edge radius obtained is about 6 μm. Unlike the tool steel specimen, both edges in the copper specimen show edge radii. Table 6 indicates that the edge radius on the upmilling side is larger than on the downmilling side because it has smaller burrs.

Table 6: Residual burr and edge radius for region between 1 and 4 mm of trace length along the straight portion of the groove

material	**tool steel**		**copper**	
groove side	**downmilling**	**upmilling**	**downmilling**	**upmilling**
radius/residual burr	**residual burr**	**radius**	**radius**	**radius**
mean (μm)	2.2	6.1	6.1	5.8
standard dev. (μm)	1.3	0.5	1.6	3.6

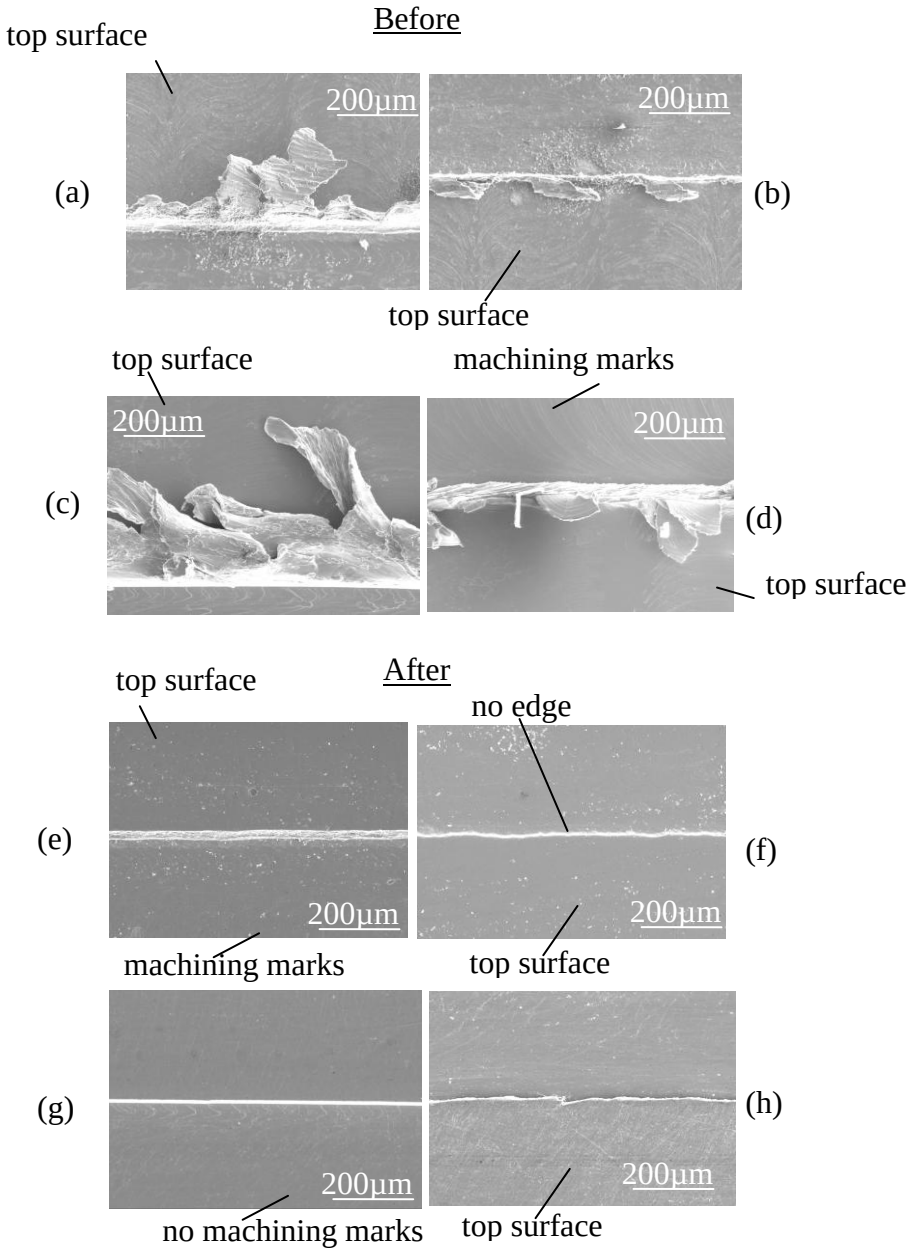

Figure 15: Burrs in milling of before and after full deburring time predicted by model for 3 µm SiC grits at 15,000 rpm. Before deburring: (a) A2 Tool steel, down milling side (b) A2 Tool steel, up milling side, (c) Copper, down milling side (d) Copper, up milling side. After deburring: (e) A2 Tool steel, down milling side (f) A2 Tool steel, up milling side, (g) Copper, down milling side (h) Copper, up milling side

CONCLUSIONS

This chapter focused on experimentally evaluating the applicability of abrasive assisted brush deburring to micromilled grooves and quantifying the effects of material hardness, spindle speed, grit size and type on the rate of burr height reduction. From this study, the following conclusions can be drawn:

- A linear regression model can be used to predict the time required for completely deburring a micromilled groove based on the maximum initial burr height present, brush rotation speed and grit type. In these experiments, the model slightly underestimates the deburring time for the harder material (tool steel) and slightly overestimates the time for the softer material (copper).
- The deburring rate is proportional to the initial burr height with an almost constant proportionality for the conditions chosen in this study. An inference drawn from this is that the burrs either bend or break at about half the initial burr height. Deburring rate increases with spindle speed and is higher for diamond than SiC. No clear trend is evident for the influence of grit size.
- Groove depth change was small for all conditions examined in this study and was maximum for the largest diamond grit at the highest speed. The edge of the groove on the upmilling side exhibits a small radius due to the action of the abrasives.
- Large burrs shield some of the area next to them from the action of bristles resulting in a slope in the surface and a depression in the unshielded region.
- The study showed that brush deburring can effectively remove large burrs in a few minutes with improvements in surface finish but the precision of the process is adversely affected by the large brush-workpiece interaction area and lack of control of the number of grits interacting with the workpiece.

The regression model can be further improved by considering Type I and II phases separately and developing a regression equation for each. The process can also be improved by concentrating the action of abrasives to the burrs and using brushes with impregnated abrasives to achieve better process control. These improvements and further mechanistic modeling are incorporated in Chapter 5 and applied to thin foils. The study of the deburring mechanism would benefit from an understanding of the properties of burrs produced during micromilling of thin foils and mechanisms of their formation and this is undertaken in the next chapter.

CHAPTER 4

BURR FORMATION IN THIN FOILS

In this chapter a detailed experimental study is conducted on the effects of spindle speed, feed per tooth, backing material and epoxy used to attach a thin nickel-titanium alloy (Nitinol) foil to the backing material on the burr size. This knowledge can be used to either reduce burr size or generate burrs of a particular nominal size to serve as micro-hooks for tissue manipulation applications.

Experiment Design

Table 7 summarizes the experimental plan. A feed per tooth below the tool cutting edge radius will tend to cause significant rubbing and generate large burrs. A new micro endmill has a typical cutting edge radius of 1-5 μm [39]. The tools used for these experiments were measured using a microscope (Nikon Microphot) and the cutting edge radius was found to be about 2.5 μm. Hence, a feed of 1 μm/tooth was chosen as the lower level of feed while the higher feed was limited by the tool strength to 10 μm/tooth.

The backing material affects the burr size due to its deformation under the cutting forces and also due to the interaction of chips with the tool (e.g. built-up edge and chip ejection). The adhesion strength of the glue can also vary with the backing material used. Aluminum 6061-T6 and PMMA were chosen as the two backing materials because of significant differences in their rigidity and adhesion strength.

The adhesive used to bond the foil to the backing material forms a thin interlayer between the two. It is expected that cyanoacrylate glues would bond much more strongly to PMMA than to aluminum and reduce delamination, thus resulting in smaller burrs. On the other hand a two part epoxy made for metal bonding applications can prevent delamination from aluminum. These epoxies also tend to be harder and form a thicker

interlayer than cyanoacrylates, which can affect the mechanics of cutting at the interlayer. Hence, a cyanoacrylate glue (Gorilla Super Glue) and a two-part epoxy (DP-420, 3M Corp.) were used to evaluate the effects of epoxy and delamination on burr height.

Table 7: Experimental plan

Factor	**Levels**	
Speed (rpm)	30,000	60,000
Wear	new	worn
Backing material	PMMA	aluminum
Adhesive	cyanoacrylate	epoxy
Feed (µm/tooth)	1	10

The spindle speed was varied to study the effect of strain rate. The maximum spindle speed possible on the micromilling set up used in this work is 60,000 rpm. Hence, this waschosen as the high speed while 30,000 rpm waschosen as the low speed. Tool wear increases the cutting edge radius. Hence, the tool was worn by touching it with240 grit emery paper for 3 seconds while spinning at 60,000 rpm. This tool was then used to machine groovesin the foil to evaluate the effect of wear on burr size.

Response measured was the burr height, which was measured by a stylus profilometer (Talysurf 112, Taylor Hobson) with a sapphire sphere stylus (φ = 0.774 mm). The large size of the stylus allows it to pick the highest points. The burr height varies along the width of the groove. Hence, three measurements were taken 50 µm apart along the width to locate the highest points of the burrs (Figure 16). Images of the burrs were also recorded with an SEM (S 3700N VP, Hitachi) to qualify the shape and type of the burr under different conditions.

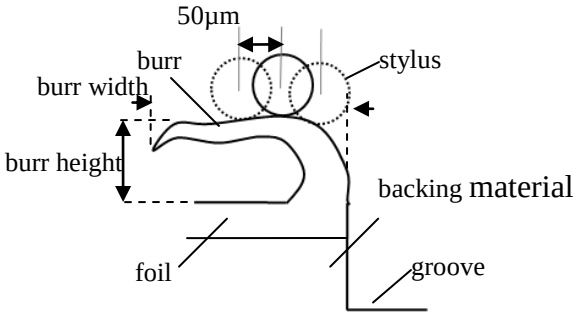

Figure 16: Burr measurement

Experimental Procedure

Straight grooves nominally 500 µm in width and 6 mm in length were micromilled in 25 µm thick shape memory NiTi alloy foils (55% Ni, As=50°C) using a 500 µm diameter, 2-flute, flat endmill (PMT TR-2-0200-S) on a custom-built desktop micromilling machine shown in Figure 17.The system consists of a high speed spindle (FS-33/60, SLF-Fraureuth) and nanopositioning stages (ALS-130, ANT-4V, Aerotech). The PMMA backing material deforms under machining forces. Hence, if insufficient axial depth of cut is used, the foil simply deforms along with the PMMA backing material and is not cut by the tool. Sufficient axialdepth of cut was experimentally found to be 300 µm and was used in all tests with PMMA backing. On the other hand, this depth of cut is too high for aluminum backing for which the tool undergoes catastrophic failure. Hence, in all experiments involving aluminum backing material, the axial depth of cut was limited to 100 µm. This difference in depth of cut for the two backing material cases does not affect the burr size because the effective depth of cut for the foil is always equal to its thickness (25 µm). A single tool pass was used for all the experiments because multiple passes tend to weaken the adhesive bond due to fatigue, which leadsto extensive delamination.

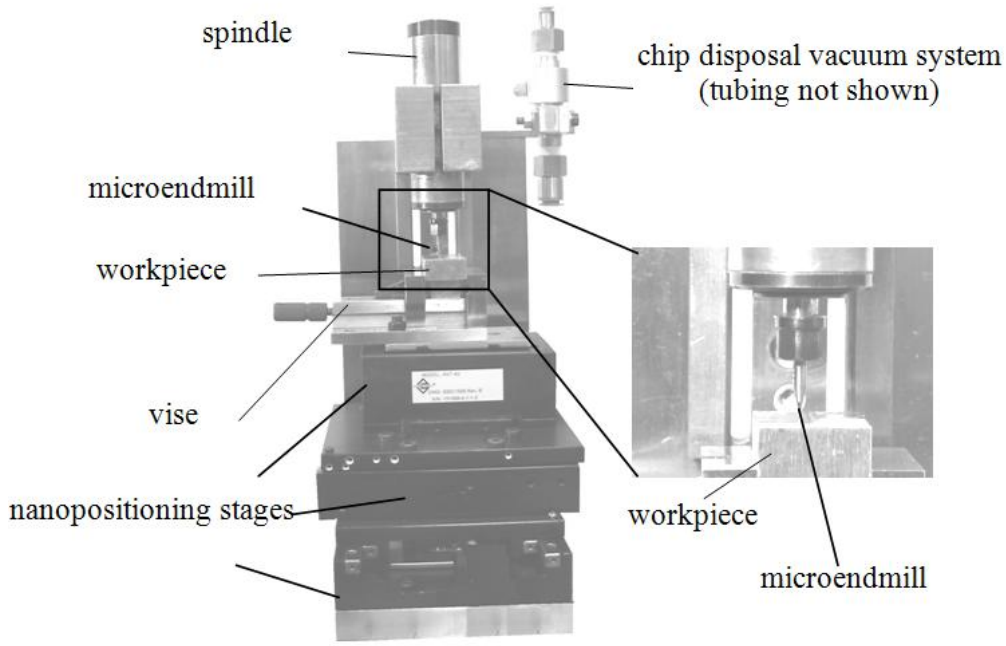

Figure 17: Experimental set-up.

A block of backing material was mounted in the vice and a reference flat was machined with a 2 mm endmill to correct for any tilt errors. The surface was then hand polished without disturbing the setup with 240 grit emery paper to remove the machining marks and obtain a uniform, roughened surface parallel to the machine axes. The foil was then heated to about 150°C to remove,via the shape memory effect, any wrinkles in it. It was then glued to the backing material while taking care to avoid the formation of voids or bumps on the surface. Grooves were then cut in the foil under the specified cutting conditions.

SEM images were taken to study the burr shape and occurrence of delamination. The foil was debonded from the backing material using an appropriate solvent (Loctite X-NMS for cyanoacrylate and Hughes Attack™ for epoxy). During micromilling, the foil tends to delaminate and bend at the groove edges. This delamination introduces errors in the measurement of burr height. Hence, the foil was heated to remove this deformation from the unmachined portion of the foil by shape memory. The burrs are strained beyond the shape memory limits and are therefore not affected by this step. The foil is then

attached to a flat surface using double sided tape and the burr height and width are measured using the stylus profilometer.

Experimental Results

Tool Wear

Figure 18 shows images of a new tool, a tool after cutting grooves in the foil with PMMA backing and cyanoacrylate adhesive, and a tool worn by usingabrasive paper. It can be seen that the used tool (Figure 18b) is chipped at the end. However, the portion of the edge that cuts the foil is higher up on the flute and is not chipped (Figure 18c). Built-up edge from cutting the soft PMMA is seen in this region, which could lead to intermittent ploughing as the built-up edge is formed and removed by the foil. In contrast, the worn tool in Figure 18d and e exhibits a chipped edge all along the flute and would plough the material much more than the used tool.

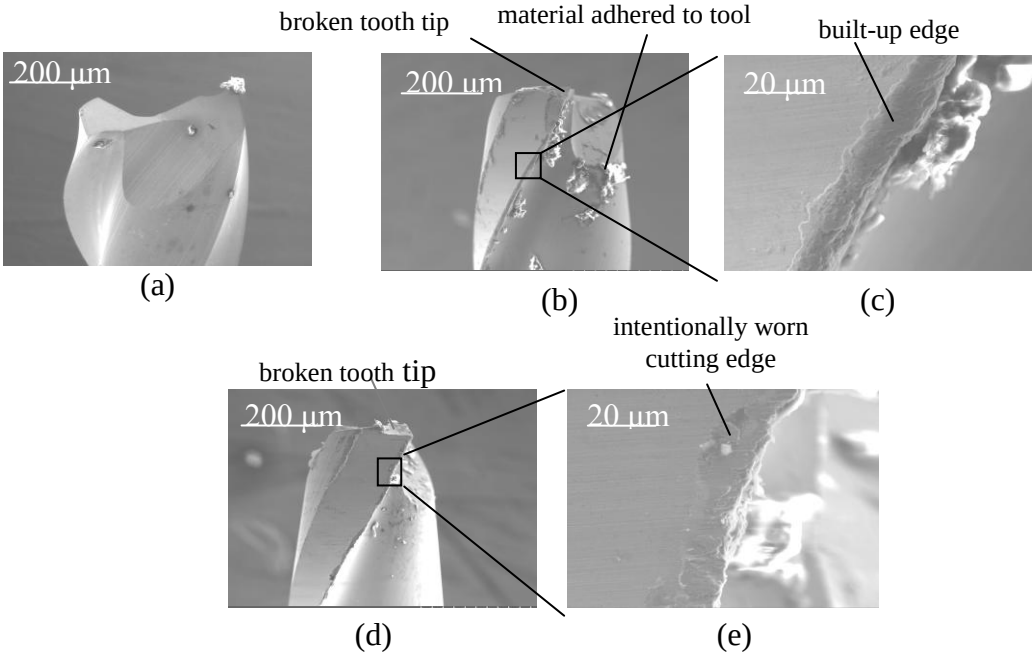

Figure 18: Tool wear (a) New tool (b) Used tool (c) Used tool (portion that contacts foil) (d) Worn (e) Detail view of worn tool

Adhesive Bond Strength

The peel strength of the bond between the foil and the backing was tested in accordance with ASTM D903 [99] in order to determine the effect of the backing-adhesive combination on burr height. The test procedure requires a 25 mm x 203.2 mm foil specimen, which is prohibitively expensive. Hence, a smaller 5 mm x 30.48 mm specimen was used in the tests. The foil specimens were glued to the aluminum and PMMA backing blocks whose surface was first milled flat and then polished with 240 grit emery paper in a manner similar to the blocks used for the milling tests. The blocks were then held in a vice, which was mounted on a piezoelectric cutting force dynamometer (Kistler Model 9256C2). The assembly was clamped in a surface grinding machine (Figure 19a). The free end of the foil was gripped in a jaw attached to the grinding wheel spindle and the spindle was then moved up to create a separation rate of 152 mm/min as per the ASTM D903 standard and the mean force was measured. This procedure was repeated four times for each combination of backing material and adhesive.

The results of the peel test are summarized in Figure 19b. It can be seen that, for a given backing material, the cyanoacrylate has a stronger bond. Similarly, for a given adhesive, aluminum has a higher bond strength. It is expected that weaker bonds will result in larger burrs.

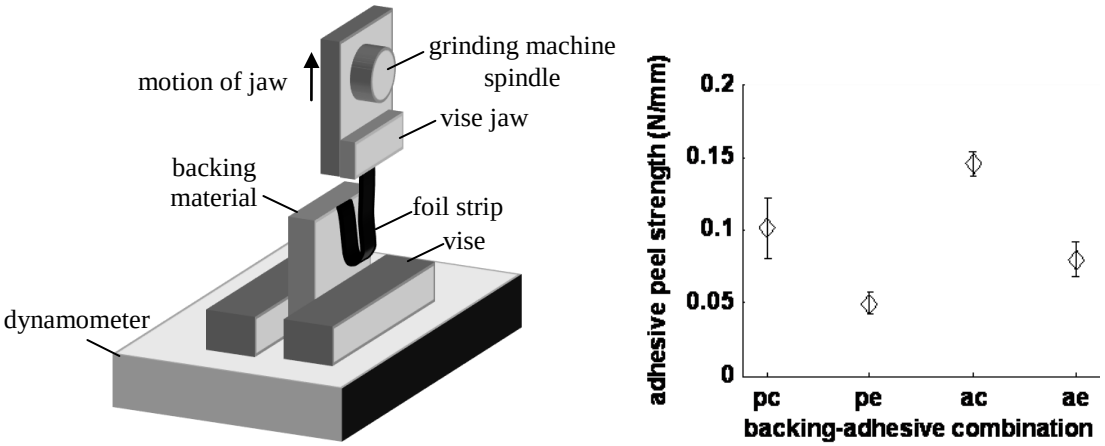

Figure 19: Measurement of peel strength (a) test set-up (b) comparison of peel strength, p= PMMA, a=aluminum, c= cyanoacrylate, e= epoxy

Burr Formation

Figure 20 shows a high speed image of burr formation on the downmilling side when micromilling the nitinol foil with PMMA backing and cyanoacrylate glue with a two flute, 500 μm diameter end mill spun at 60,000 rpm and fed radially at 10 μm/tooth. It can be seen that the foil initially bends up and plastically stretches in front of the advancing tool to form a semicircular wall (Figure 20a). As the tool advances, the tensile strength of the foil is exceeded and it tears roughly in the middle of the groove (Figure 20b). The tooth tends to rip the foil at the beginning of the cut at the upmilling side and sweep the material towards the downmilling side. This can be clearly seen from Figure 20c, which shows the tool from the upmilling side. As a result, most of the burrs are found on the downmilling side while the upmilling side of the groove shows small or no burrs. Note that this mechanism of burr formation is significantly different from the side-flow phenomenon responsible for burr formation in bulk materials.

Sometimes, the burr on either side of the groove may get caught in the flute of the mill. This can cause the crack at the base of the burr to extend along the edge until it

intersects with the other edge of the burr and the burr is removed from the base material. In this case, no burr is found on that side of the groove (Figure 20d and e).

Foil delamination plays an important role in burr formation. If the bond between the foil and the adhesive is strong, chips are formed instead of tearing of the material (Figure 20f). In this case very small burrs were found on the edges, whichcan be explained by noting that the chip load in milling is small at the beginning and end of cut leading to more rubbing instead of cutting.

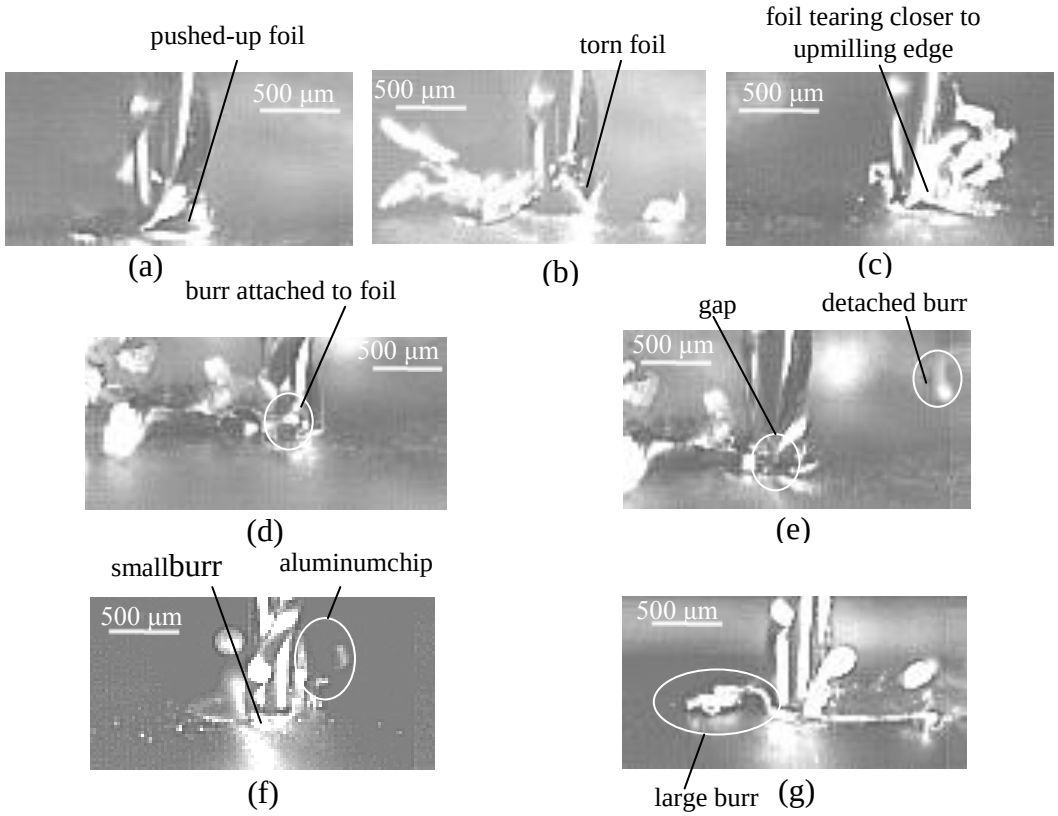

Figure 20: High speed video stills of burr formation(a)stage 1: foil pushed up (b) stage 2: foil tearing (c) stage 3:foil tearing closer to upmilling side (d) burr fracture (before) (e) burr fracture (after) (f) Foil machining by chip formation(g)burr formation with slow feed viewed from upmilling side

Figure 20g shows the formation of a burr on the upmilling side for a feed of 1 µm/tooth. As mentioned before, the material forms a plastically deformed wall in front of the tool and tears close to the upmilling side leaving behind a small burr. The material

may also tear on both the upmilling and downmilling sides forming a large strip of material in front of the tool. The crack on the upmilling side then progresses towards the downmilling side and a burr significantly larger than the groove width is left on the downmilling side.

Figure 21 shows the interaction of chips from the foil, adhesive and base material. Figure 21a shows a PMMA chip caught between the tool and the pushed up foil. The entrapped chip can potentially apply a tensile load to the foil and cause it to tear. Figure 21b and c show larger chips of PMMA and aluminum, respectively, attached to the tool and being swung around by it. Such large chips could break-off any loosely attached burrs on the foil.

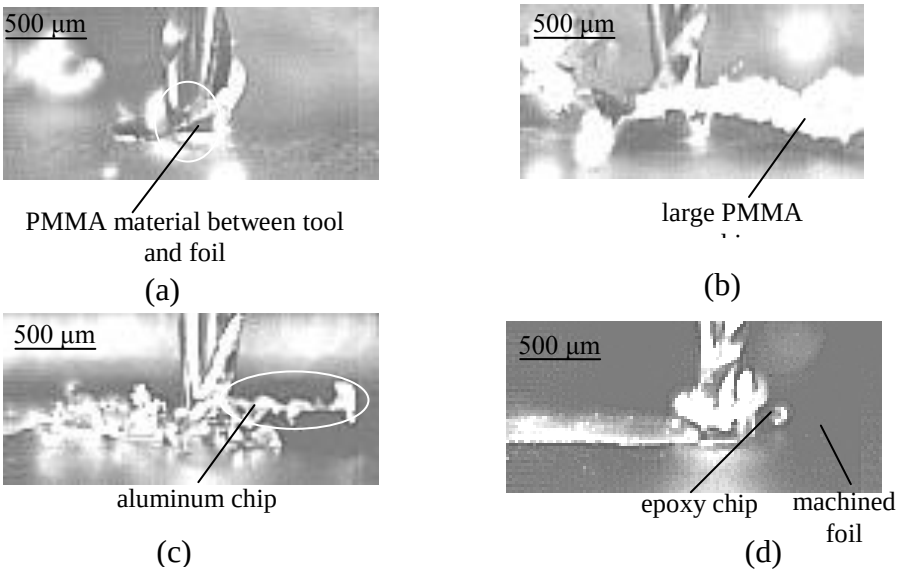

Figure 21: Chip formation: (a) PMMA chip, foil interaction (b) large, continuous PMMA chip (c) large continuous aluminum chip (d) epoxy chip and machined foil

Epoxy forms a much thicker layer between the foil and the backing material due to its higher viscosity in comparison to cyanoacrylate and hence, during cutting, chips of epoxy are formed. This is clearly seen in the case where aluminum is the backing material as in Figure 21d. The chip being swung around by the tool shows a level of

flexibility and luster that cannot be attributed to the foil or the backing material and hence must be because of the epoxy. As mentioned in the previous discussion, this is also the case where the foil gets cut rather than torn. It is difficult to distinguish the foil and aluminum chips since they look very similar. It is reasonable to believe that the base material produces larger chips as seen in Figure 21c while the smaller chips in Figure 21d are from the foil. It may also be that the tool removes chips that are a combination of all three materials (i.e. without delamination).

Factors Affecting Burr Shape

SEM images of burrs formed under various machining conditions are shown in Figure 22. Three main shapes of burrs can be identified from the images, namely, rollover type, feathery type [40] and wall type (Figure 22a, b and c, respectively). Rollover type burrs are formed when the foil tears in front of the tool and gets deposited on either side of the groove (Figure 23a). These are the most commonly seen burrs in the present set of experiments.

Formation of feathery burrs differs from rollover burrs in that they are chips cut from the foil rather than being parts of material that were torn. These chips are not completely cut off from the base material and remain attached to the downmilling side of the groove. This behavior can be explained by noting that ploughing dominates at the beginning and end of the cut and hence, towards the end of the cut, the material gets pushed and bent over rather than cut. There is a higher tendency for these burrs to form in micromilling of thin foils because of their flexibility.

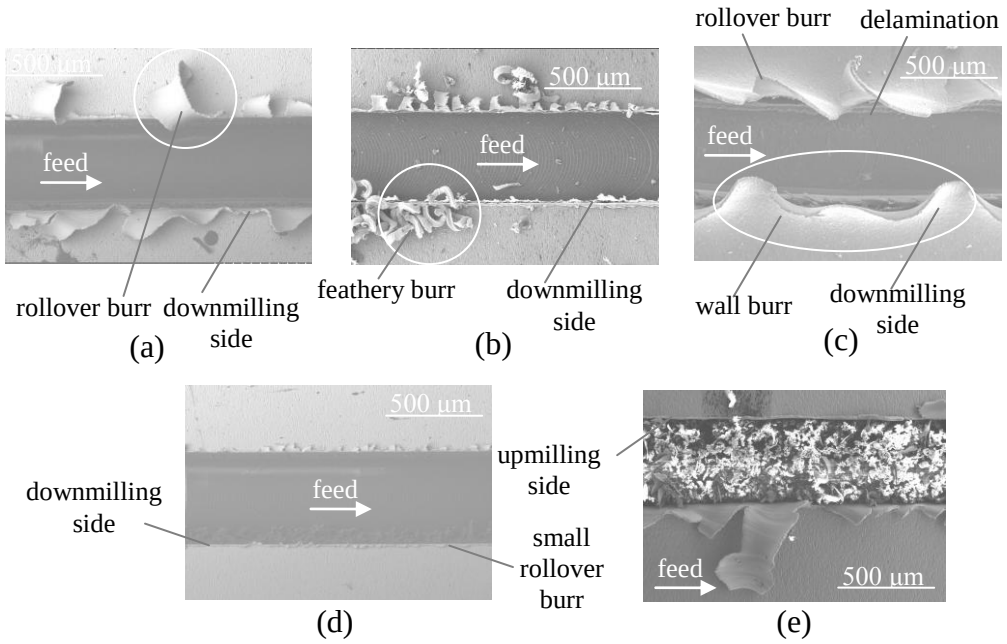

Figure 22: Burr shapes: (a) Rollover type (b) Feathery type (c) Wall type (d) Small, evenly spaced rollover type, 10 µm/tooth (e) Small, evenly spaced rollover type, 1 µm/tooth

In the present set of experiments, feathery burrs were seen almost exclusively on sections of the downmilling side of the groove when machining the foil with aluminum backing and using a new tool at 60,000 rpm and 10 µm/tooth with both adhesives. The only exception was a very short section of the groove machined with PMMA backing using a new tool at 60,000 rpm and 10 µm/tooth with cyanoacrylate adhesive. The presence of these burrs at higher feeds with a new tool is expected since these are the required conditions for cutting the material instead of tearing it.

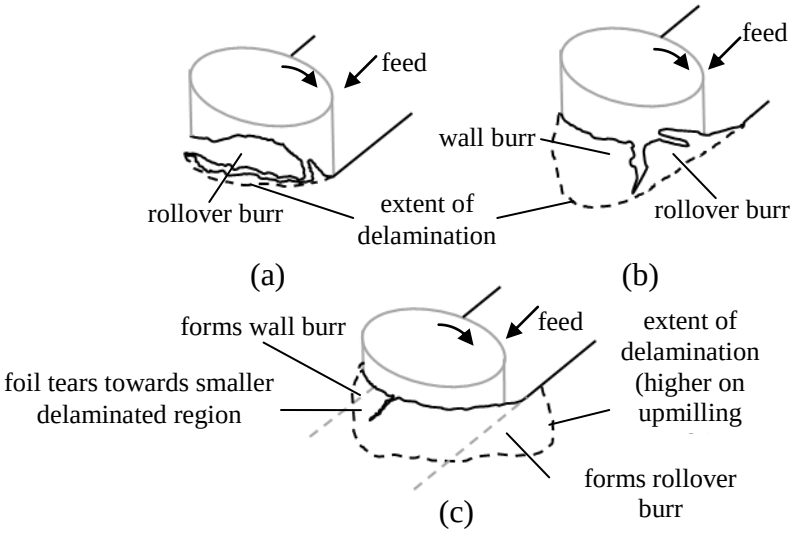

Figure 23: Schematic of burr formation (a) rollover type (b) wall type (c) wall type with low feed

Wall type burrs are burrs where the foil is bent upwards on the side of the groove forming a continuous ribbon of material without any cracks or discontinuities (Figure 22c). These are formed by foil tearing in front of the tool (Figure 23b). However, unlike rollover burrs, in this case, the foil always tears towards one side of the groove leaving a continuous wall of material along the other edge. Hence, these burrs are always accompanied by rollover burrs on the other side of the groove. In three of the experiments, these burrs were found to be exclusively on the downmilling side when using a worn tool at a feed of 10 μm/tooth. When using a worn tool at high feeds, the cutting forces are significantly higher causing more delamination along the edges as seen in Figure 22c where the base material is clearly exposed. Due to wear, the frictional forces are high leading to tearing of the foil closer to the upmilling side as mentioned in the previous section. However, due to high delamination, the foil does not tear along the width of the groove but rather along the length towards the upmilling side leaving a bent foil forming a wall on the downmilling side (Figure 23b).

Considering the application for tissue grasping and manipulation, one would prefer hook shaped rollover burrs with consistent spacing. These are formed with a new tool spun at 60,000 rpm and 10 μm/tooth feed with PMMA backing and cyanoacrylate adhesive on both the upmilling and downmilling side (Figure 22d). They are also formed on the upmilling side under the same conditions with both types of adhesives. At 1 μm/tooth feed, only aluminum backing with epoxy adhesive produces these burrs on the upmilling side of the groove (Figure 22e).

Factors Affecting Burr Height

Burr height varies significantly along the length of the groove as seen in Figure 22. Without loss of generality, histograms of burr height under various machining conditions are shown in Figure 24 to study the frequency distribution of burrs machined with PMMA backing using a new tool and cyanoacrylate glue. Since the burr height in these experiments can never be less than zero, the distribution is not symmetric. In some cases, two modes are present, which may be due to the presence of two types of burrs (as in the case of Figure 22b) or due to the burrs being broken off by the tool and leaving a gap (as in the case of Figure 22a). It is difficult to fit any of the standard distributions to the data, although they resemble a normal distribution with a positive or zero skew or a χ^2 distribution. The high speed, low feed burrs are the closest to a normal distribution. It is to be noted that for the positively skewed distributions, the range of burr sizes (x-axis of histogram) represented by the shift is much smaller than for the remaining portion of the plot. It is also seen from the histograms for other conditions (not shown for brevity), that the conditions which produce larger burrs (e.g. with a worn tool) are much more symmetric. For the application of gripping tissue with these burrs, it is reasonable to assume that the larger burrs would have a greater chance of snagging the tissue. Hence,in this case, the positive skewness may be assumed to be insignificant.

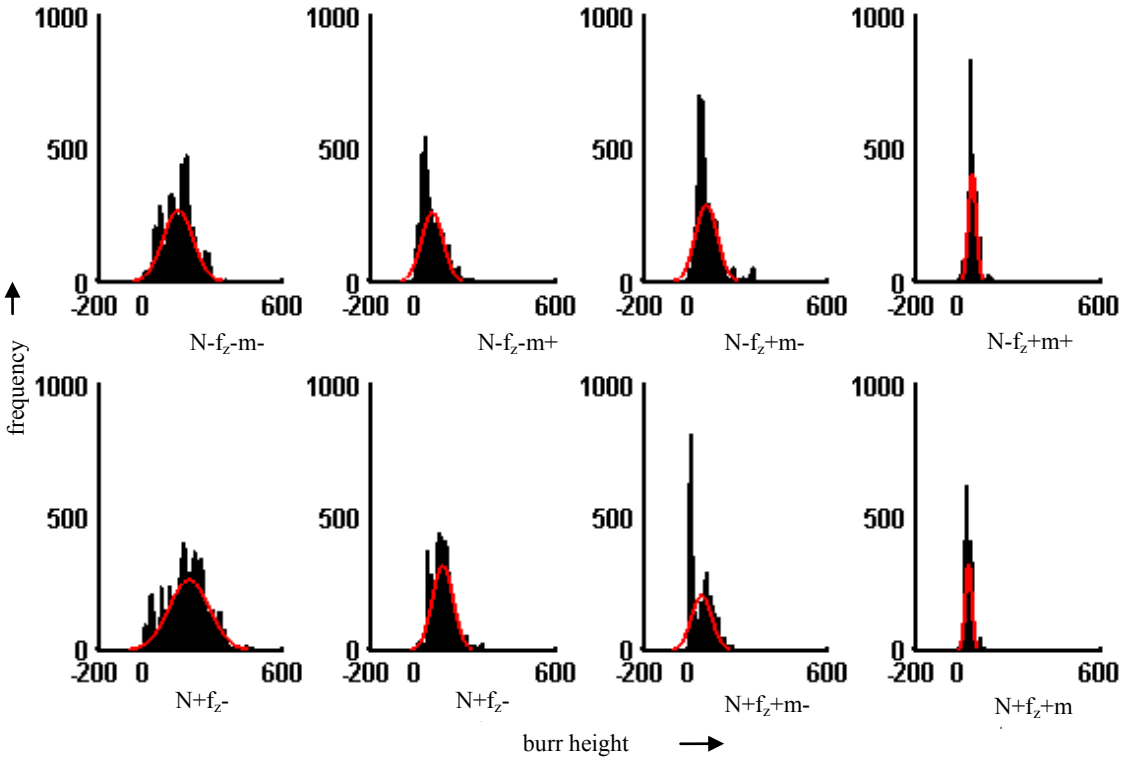

Figure 24: Histogram of burr height for grooves milled with PMMA backing, cyanoacrylate adhesive and a new tool

(N = spindle speed: - = 30,000 rpm, + = 60,000 rpm, fz = feed: - = 1 µm/tooth, + = 10 µm/tooth, m= milling side: - =downmilling, + = upmilling)

For this application, the information of most interest is the mean burr height and the variance. This is effectively shown using the boxplots in Figure 25. The top and bottom limits of the boxes are the 75% and 25% percentiles respectively, the line in the middle of the box is the median, lines at the end of the dashed line indicate 1.5 times the interquartile range (IQR) and the black boxes are outliers. These plots can alsobe used to compare the effect of change in machining parameters on the burr characteristics. Several outliers (black boxes) can be seen in these plots. However, they represent a very small percentage of the total number of data points (~ 5%). The entire experimental data produces 64 such plots, whichare not shown here for brevity. However, the main observations derived from them are discussed below. The effects of adhesive used (*A*),

spindle speed (N), feed per tooth (f_z) and side of groove (m) (upmilling or downmilling) on the burr height are summarized in Figure 26.

Effect of Milling Direction

The largest change in burr height is noted for the side of groove. Burrs on the downmilling side (m-) are larger than those on the upmilling side (m+) in almost all cases. This is due to the foil being cut or torn closer to the upmilling side and remaining attached to the base material on the downmilling side as discussed earlier. It can be noted that the difference in mean burr heights for the two sides is much smaller at higher feeds. The maximum size difference between the downmilling and upmilling burrs is noted for cutting with a worn tool at 60,000 rpm and 1 µm/tooth feed with aluminum backing and epoxy adhesive. In this case, the foil rips very close to the upmilling side as seen in Figure 23b due to the strong bond between the epoxy and foil.

An interesting (and only) exception to this rule is the burrs produced when milling with aluminum backing, cyanoacrylate adhesive, and a worn tool spun at 30,000 rpm and fed at 10 µm/tooth. In this case, the rollover burrs formed on the upmilling side are consistently much larger than the wall type burrs formed on the downmilling side. The mechanism of burr formation in this case is depicted in Figure 23c. Ploughing forces at the tool tip are much higher on the upmilling side because the workpiece is moving against the tool. Hence, it is suggested that the foil delaminates more on the upmilling side than on the downmilling side. It is also suggested that the foil will tear along the shortest path from the point where the tool contacts the foil to where it contacts the backing material. In this case, the path would be along the downmilling side rather than the upmilling side (compare Figure 23b and 7c).Hence, the foil tears closer to the downmilling side leaving a large rollover burr on the upmilling side with a smaller wall burr on the downmilling side. This mechanism does not occur at the higher spindle speeds because the high feed rate (mm/min) does not allow enough time for the foil to get

sufficiently delaminated. It is also seen only when using aluminum with cyanoacrylate adhesive because the bond strength is significantly lower in this case.

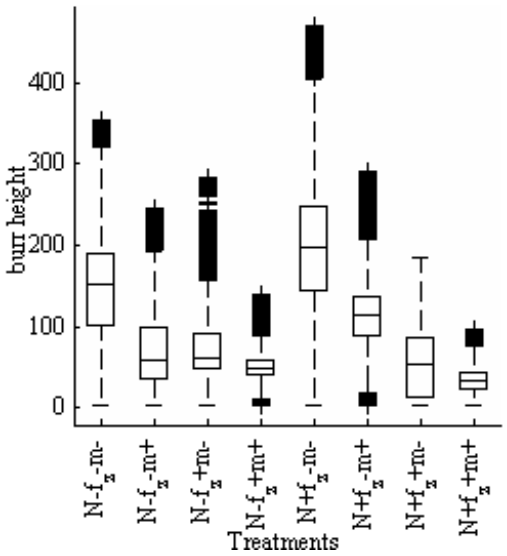

Figure 25: Boxplot of burr height for grooves milled with PMMA backing, cyanoacrylate adhesive and a new tool

(N = spindle speed: - = 30,000 rpm, + = 60,000 rpm, fz = feed: - = 1 µm/tooth, + = 10 µm/tooth, m= milling side: - =downmilling, + = upmilling)

Effect of Tool Wear

Another significant factor affecting burr size is tool wear. Burrs formed by a worn tool are much larger than those formed with a new tool. This is to be expected since a worn tool will typically cause material removal by tearing rather than chip formation via shear. In addition, the cutting forces will also increase significantly due to the higher frictional forces obtained with a worn tool. This in turn would lead to increased delamination and the formation of large wall or rollover type burrs.

Figure 26 indicates that the overall effect of increasing the feed is to increase burr height. However, further insight is obtained by considering the interaction of wear and feed (Figure 27). It can be concluded that increasing the feed when machining with a new

tool actually reduces the burr size. This behavior is expected because if the feed per tooth is smaller than the tool cutting edge radius, the foil is torn rather than cut and this leads to large burrs. In groove milling, the undeformed chip thickness starts at zero at the beginning of cut and increases to a maximum at the center of cut and then reduces to zero at tooth exit. Hence, for higher feeds, ploughing occurs only at the beginning and end of cut to form burrs. In the portion of cut where the undeformed chip thickness is higher than the tool edge radius, a conventional chip is formed and the material is removed leaving comparatively small burrs along the edges (Figure 22d). This also explains why the difference in burr heights for upmilling and downmilling are smaller at higher feeds. For a worn tool, however, material removal by conventional chip formation never occurs and hence this behavior is not observed. Furthermore, as the feed increases, the machining forces obtained with a worn tool increase, which causes increased delamination and hence, larger burrs via the mechanisms illustrated in Figure 23b and 7c.

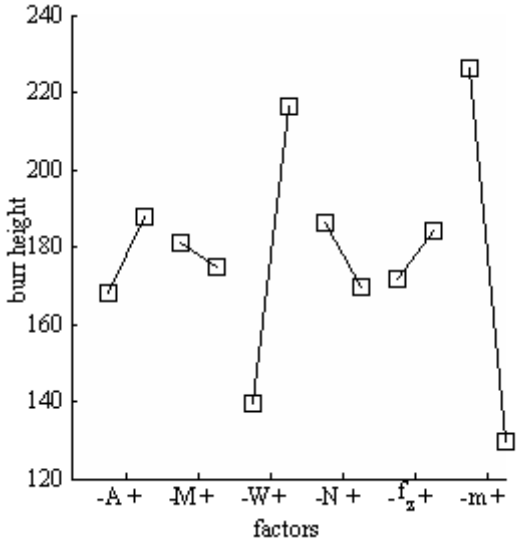

Figure 26: Mean effects plot (A = adhesive: - = cyanoacrylate, + = epoxy, M: backing material: - = PMMA, += aluminum, W= tool wear: - = new tool, + = worn tool, N = spindle speed: - = 30,000 rpm, + = 60,000 rpm, fz = feed: - = 1 µm/tooth, + = 10 µm/tooth, m= milling side: - =downmilling, + = upmilling)

Effect of Cutting Speed

Figure 26 indicates that lower cutting speeds produce larger burrs. This may be explained by noting that slower speeds allow for longer time for delamination and bending of the foil resulting in larger burrs similar to the mechanism in Figure 23c. This theory is supported by the wear-speed interaction shown in Figure 27. It can be seen that for a worn tool, the effect of speed is considerably pronounced. On the other hand, for a new tool, the effect is not very significant. This suggests only a minor effect of strain rate. This is to be expected since even at high angular velocities, the peripheral velocity of the tool is low (1.57 m/s) due to the small tool diameter.

Effect of Backing Material

From the main effects plot, it is noted that the PMMA backing material results in larger burrs. PMMA is much softer than aluminum and has a lower melting point (~150°C).As a result, it tends to soften and flow due to the heat generated at the tool tip. Figure 18b shows a built-up edge on the tool used to machine the foil with PMMA backing. This can lead to increased ploughing. Figure 21b also shows that PMMA forms much larger chips which would further impede cutting of the foil.

Effect of Adhesive

Epoxy results in larger burrs than if cyanoacrylate was used as the adhesive. This suggests that cyanoacrylate adheres better to the foil. Another factor that needs to be considered when using epoxy as the adhesive is that it forms a much thicker layer between the foil and backing material due to its higher viscosity. As seen in Figure 21 chips of epoxy are formed during milling, which may interfere with cutting of the foil. Typically, the bond strength is a function of the material being bonded. Hence, it is reasonable to expect an effect of the adhesive-backing material interaction (Figure 27). For any given backing material, changing from cyanoacrylate to epoxyproduces an

increase in the burr height. Changing from PMMA to aluminum with cyanoacrylate does not change the mean burr height. Changing from PMMA to aluminum with epoxy reduces the mean burr height. Comparing these trends with those for the adhesive peel strength in Figure 16b, it can be seen that a lower peel strength results in a larger burr height. This supports the statement that increase in foil delamination leads to larger burrs.

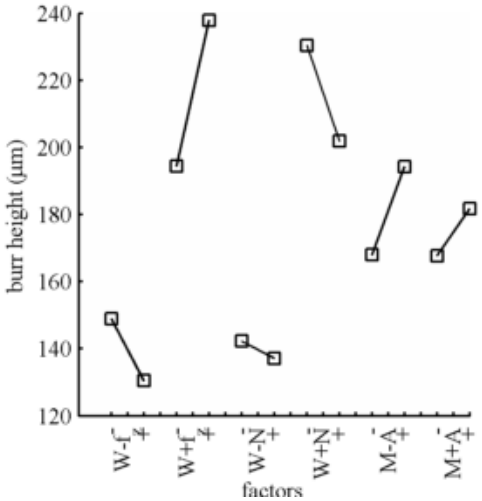

Figure 27: Interaction effects plot

These trends are further quantified by conducting an ANOVA including up to three-factor interactions with $\alpha=0.05$. The p-values indicate that all interaction terms are significant except the material-speed and adhesive-speed-feed terms.This suggests that strain rate effects when machining the backing material do not significantly affect the burr height. The adhesive-speed-feed term may be interpreted as the interaction between the adhesive and feed rate (mm/min) and is shown to be insignificant in these experiments

The boxplots in Figure 25 can also be used to study the variation in burr height for each case represented by the distance between the dashed lines. The highest variation (700 µm) is noted for the burrs on the downmilling side of grooves cut with aluminum backing, cyanoacrylate adhesive and a worn tool at 60,000 rpm and 10 µm/tooth feed, which also has the highest mean burr height for the present set of experiments. The

smallest variance is observed for the burrs on the upmilling side of the groove cut with PMMA backing, cyanoacrylate adhesive with a new tool spun at 60,000 rpm and 10 µm/tooth feed. From a practical standpoint, one would want the variance to be as low as possible while still achieving the target burr height.

Effect of Feed

The change in burr height with feed is studied over a range of feedsfrom 1 µm/tooth (120 mm/min) to 100 µm/tooth (12,000 mm/min). Grooves were milled with a new tool on foil attached to PMMA backing with cyanoacrylate adhesive at 60,000 rpm and the burr height was measured. Figure 28 a and b show the change in burr height with feed. It can be seen that initially the burr height on the downmilling side is high until the feed reaches 5µm/tooth (600 mm/min). At this point the burr height decreases until the feed reaches 10 µm/tooth (1200 mm/min) and then increases until the burr height reaches a mean value of about 500 µm, which is the width of the groove. This trend can be verified by the SEM images in Figure 29a to h. Visual observation suggests that below 5µm/tooth and above 10 µm/tooth the sum of the length of the burrs on both sides of the groove is greater than the width of the groove. This suggests that the foil tears instead of forming chips. At 5 µm/tooth and 7.5 µm/tooth feeds the burr lengths are much smaller than the groove width implying material removal via chip formation. Above 50 µm/tooth, the foil tears on the upmilling side. The crack propagates along the length of the grooveand terminates on the downmilling side leaving a large patch of foil while hardly any burrs are formed on the upmilling side. For high feeds (beyond 50 µm/tooth in these experiments), this explains the presence of small burrs on the upmilling side and the less pronounced effect of feed on burr height.

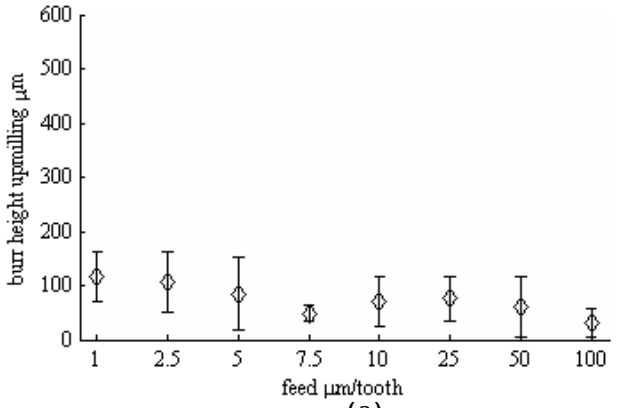

(a)

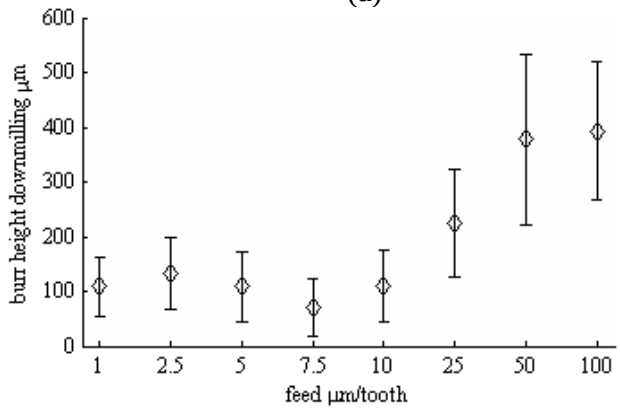

(b)

Figure 28: Effect of feed on burr height (a) upmilling side (b) downmilling side

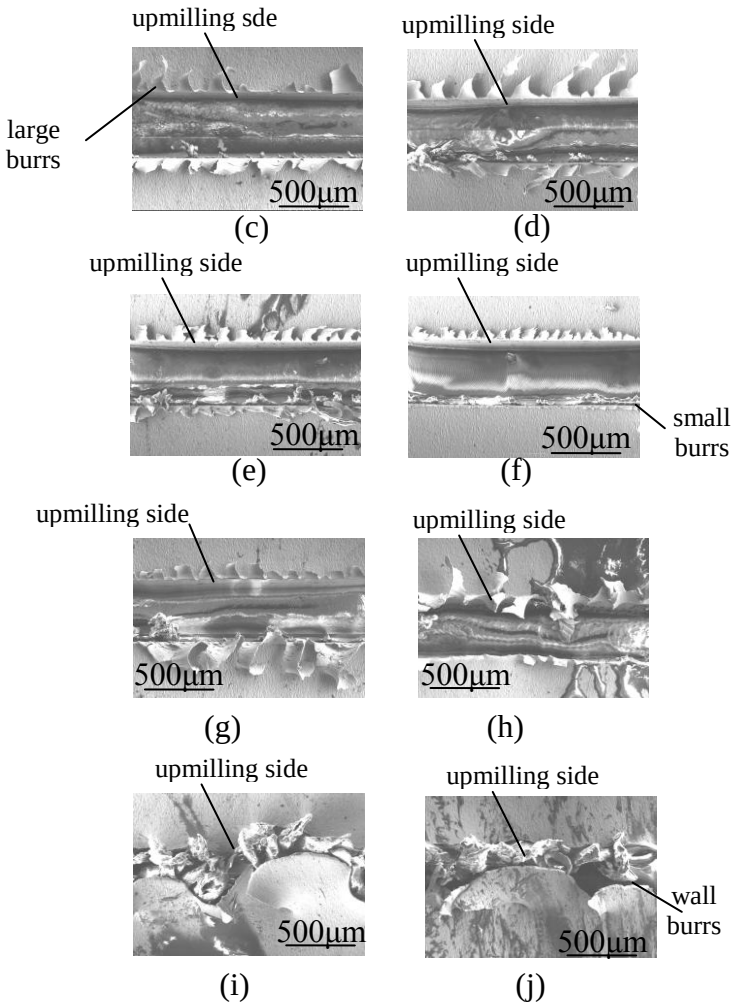

Figure 29: Effect of feed on burr height (a) 1 µm/tooth (b) 2.5 µm/tooth (c) 5 µm/tooth (d) 7.5 µm/tooth (e) 10 µm/tooth (f) 25 µm/tooth (g) 50 µm/tooth (h) 100 µm/tooth. Images oriented with upmilling side towards the top.

Burr Formation Model

A kinematic model has been developed to predict the burr widths (Figure 16) in micromilling of thin foils. Figure 35a and b show the tooth at the beginning of cut while Figure 35c shows the geometry at the tool tip. The tip with radius *r* begins to penetrate the foil, which is a circular arc with radius *R*. The tip initially ploughs into the foil, which deforms to accommodate the tool geometry inducing a tensile stress σ_t in the foil that is

balanced by the adhesive forces between the foil and the backing material. The force F_t due to the stress σ_t in the foil can be resolved into components perpendicular to the edge F_p and along the edge of the foil F_s. The force F_p induces a force per unit length σ_p in the adhesive along the edge of the foil, which causes the foil to peel from the backing material. The force F_s causes the foil to shear from the backing material. Experimental tests show that the foil fails by peeling from the backing. If σ_p is greater than the peel strength σ_{pf} of the adhesive, the foil delaminates. The delaminated foil subtends an angle γ with the undeformed foil. As delamination progresses, γ becomes smaller which in turn reduces F_p until equilibrium is reached when σ_p is equal to σ_{pf}. The stress $\sigma_t$is associated with a strain ε_t in the foil. If ε_t reaches the tensile failure strain of the material ε_f the material fails and the foil begins to tear. The associated stress at failure is σ_f.

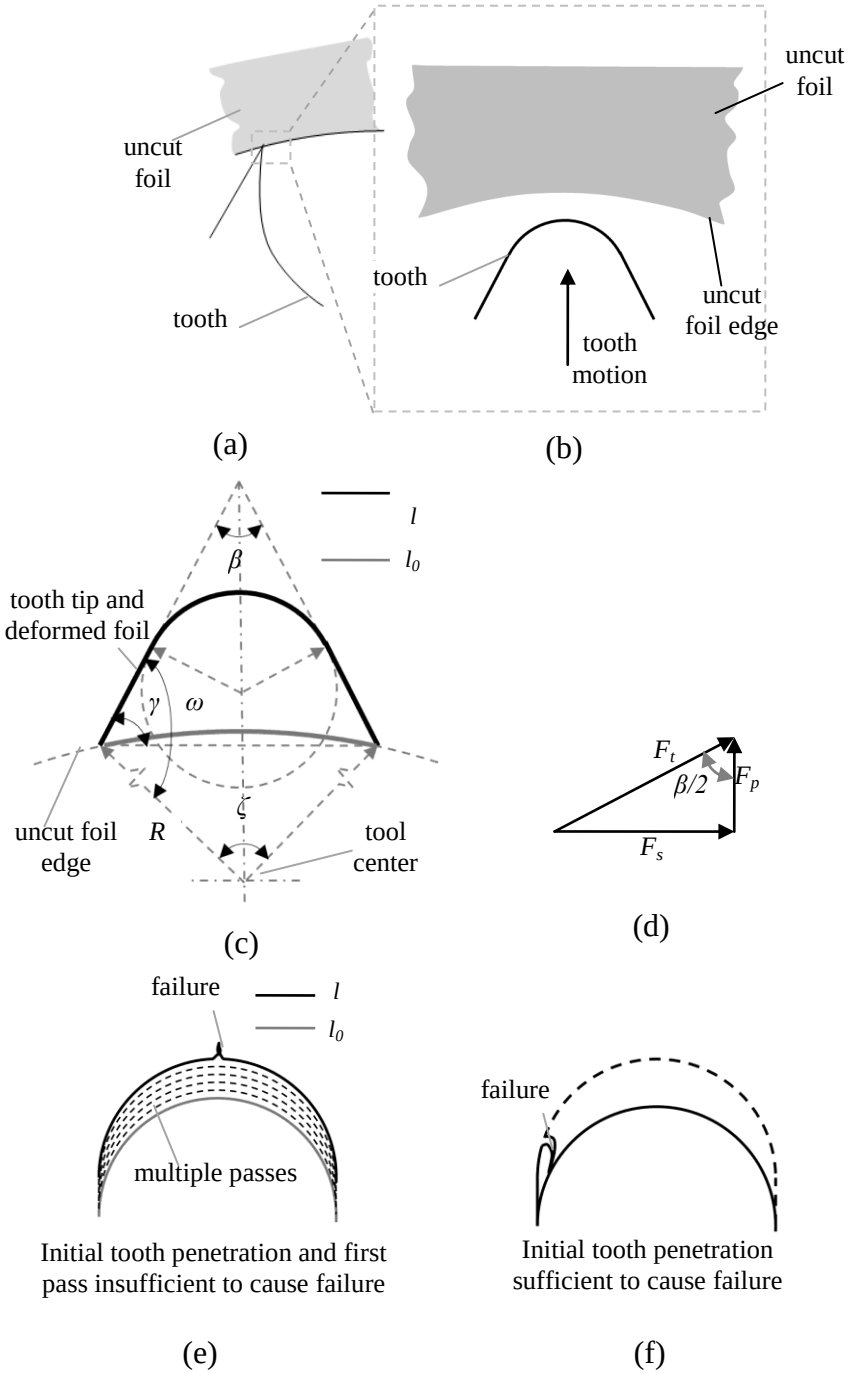

Figure 30: Burr formation model (a) schematic of tooth engaging with foil (b) enlarged view of tooth before penetration into foil (c) kinematics of foil at tooth tip (d) force balance in foil (e) undeformed length and strained length at failure when $\varepsilon_t < \varepsilon_f$ (f) Foil failure at initial penetration when $\varepsilon_t > \varepsilon_f$.

At low feeds, ε_t is less than ε_f and the foil merely deforms but does not tear. The cutting tooth proceeds along the circular path with radius *R*and delaminates the entire foil along the tooth path. For the delaminated foil to fail in tension, the strain in the entire delaminated length should reach the failure strain ε_f . Comparing Figure 35c with Figure 35d, it can be noted that the initial undeformed length l_0 is much greater in the low feed case. Hence, the tooth progresses through multiple rotations before the strain in the foil reaches ε_f. The foil fails at its weakest point, which is dictated by microcracks that are produced by the previous pass and forms burrs on either side of the groove. For simplicity, it is assumed in this model that the foil cracks at the midpoint of the tooth path giving a burr width equal to half the strained length l of the foil at failure. For higher feeds, ε_t is greater than ε_f and the foil fails in tension at the tooth tip. It leaves a small burr on the upmilling side with a width equal to the delaminated length l (Figure 35e) while removing the rest of the foil as a chip. Hence, no significant burrs are found on the downmilling side at high feed (Figure 28e and f).

Mathematical treatment of this phenomenon is based on the following assumptions:

1. Deformation of the delaminated foil at the tool tip equals the feed per tooth.
2. Foil is thin and has negligible bending stiffness.
3. Stress in the cross-section of the ploughed foil is assumed to be constant and directed along the top edge of the delaminated foil (Figure 31a).
4. Compressive stresses due to the tool tip are negligible compared to the tensile stresses induced by stretching of the foil thereby implying a plane stress condition (Figure 31b).
5. The foil fails at the middle of the delaminated region (Figure 30c, Figure 31b).
6. Material is homogeneous and isotropic.

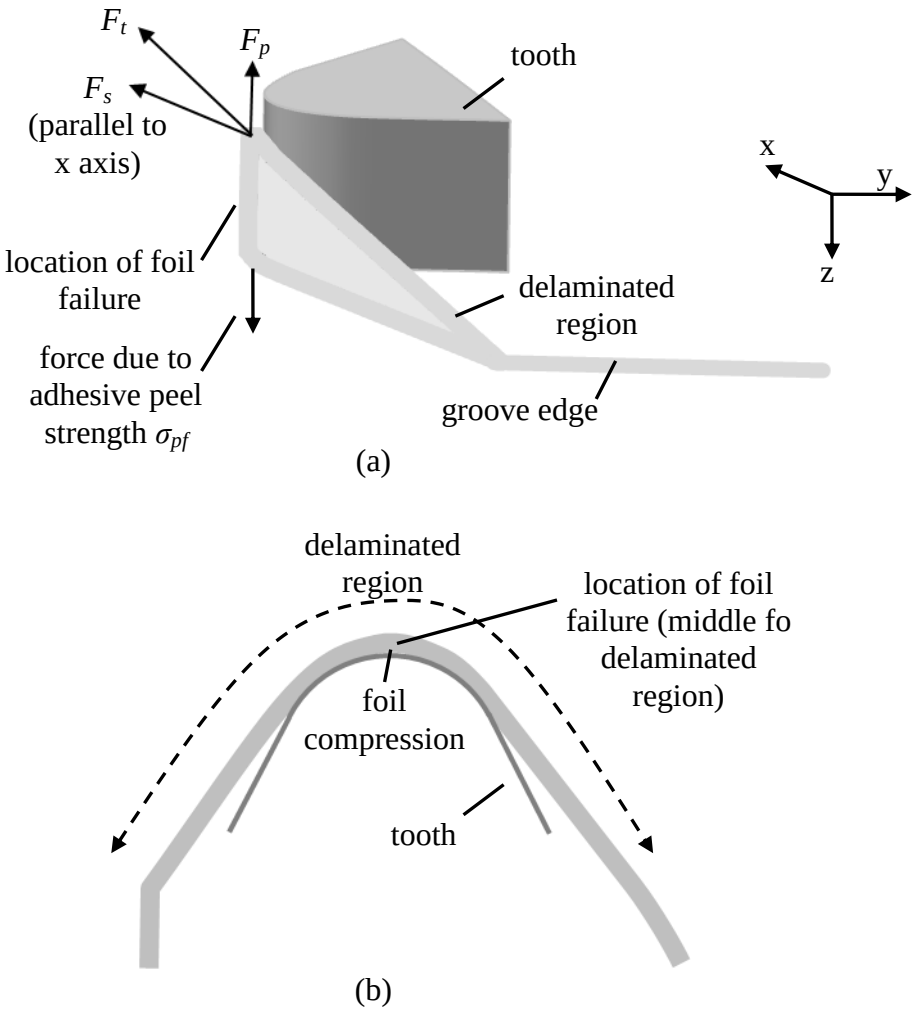

Figure 31: Assumptions in model (a) Forces acting at the tool tip (b) Location of foil failure if feed is sufficient to cause failure at tip

Assumption 1 and 4 are based on the absence of wrinkling of the foil as examined by high-speed video (see Figure 20a). Assumption 2 limits the validity of the model developed here to thin foils that on delamination bend upwards as seen in Figure 20a and 20b. Assumption 3 is an approximation that is valid given that the foil is ploughed up by a few microns, which allows the variation of stress over this distance to be neglected. Assumption 5 is a simplification required in the absence of a model that would predict

crack initiation during burr formation, which would require a crack-free material with no surface defects.

The burr width is calculated by first estimating ε_t for a given feed per tooth d using Eq. 9 to 18, which are obtained from the geometry shown in Figure 30c (refer Figure 32). If $\varepsilon_t<\varepsilon_f$, then Eq. 18 to 20 are used to calculate the number of tooth passes n before $\varepsilon_t>\varepsilon_f$ (Figure 30e) and the burr width is given by $0.5l$. If on the other hand, for a given d, $\varepsilon_t>\varepsilon_f$ then the burr width is given by Eq.15. Equation 16 is obtained by a force balance between F_t and F_p. Equations 19 and 20 represent a system of implicit equations and are solved numerically. The developed model is applied to the case of milling NiTi foil using the values in

Table 8. Grooves were milled in a foil with PMMA backing and cyanoacrylate adhesive at feeds shown in Figure 33. The burrs were then flattened and their width measured in a microscope. Figure 33 shows that the measured and predicted mean burr widths are in good agreement.

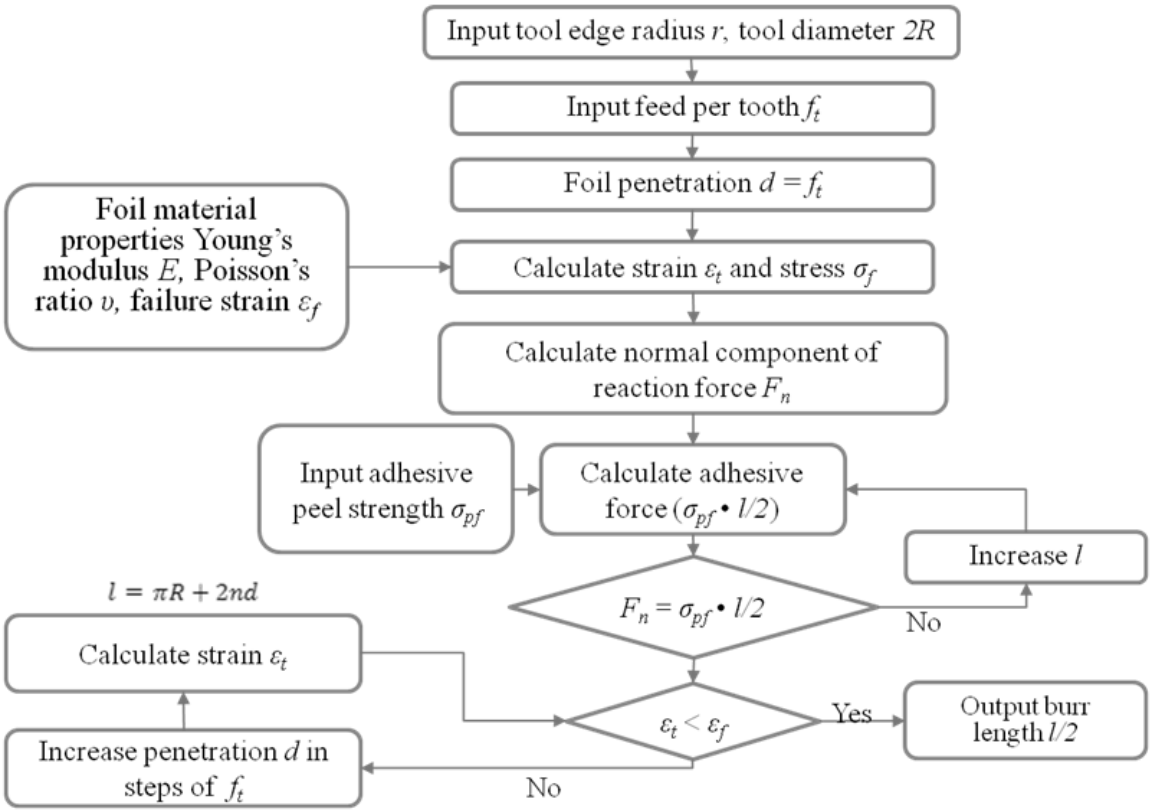

Figure 32: Schematic explaining the modeling methodology for burr formation.

$$a = r\left(1 - \operatorname{cosec}\left(\frac{\beta}{2}\right)\right) \quad \textbf{(9)}$$

$$\omega = \sin^{-1}\left[\frac{R + d + a}{R}\sin\left(\frac{\beta}{2}\right)\right] \quad \textbf{(10)}$$

$$\gamma = \frac{\pi}{2} - \frac{\beta}{2} \quad \textbf{(11)}$$

$$\zeta = 2\left(\pi - \frac{\beta}{2} - \omega\right) \quad \textbf{(12)}$$

$$C = \left\{R\left[1 - \cos\left(\frac{\zeta}{2}\right)\right] + d + a\right\}\sec\left(\frac{\beta}{2}\right) \quad \textbf{(13)}$$

$$D = r\cot\left(\frac{\beta}{2}\right) \quad \textbf{(14)}$$

$$l = r(\pi - \beta) + 2(C - D) \quad \textbf{(15)}$$

$$l_0 = R\zeta \quad (16)$$

$$\beta = 2\left[\cos^{-1}\left(\frac{\sigma_{pf}\, l}{2\,\sigma_f[(1-\vartheta)\varepsilon_t]^2\, t\, d}\right)\right] \quad (17)$$

$$\varepsilon_t = \ln\left(\frac{l}{l_0}\right) \quad (18)$$

$$l = \pi R + 2nd \quad (19)$$

$$l_0 = \pi R \quad (20)$$

Table 8: Values used for burr prediction model

Property	Value	Source
R (µm)	250	Measured
r (µm)	2	Measured
σ_{pf}(N/mm)	0.1	Measured
σ_f (MPa)	1400	[100]
ε_f	14	[100]
υ	0.33	[101]
t (µm)	25	Manufacturer

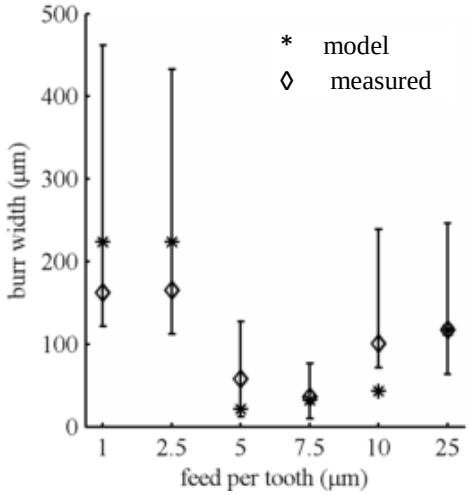

Figure 33: Predicted vs. experimental burr width

The developed model is tested for generalization and scalability by varying one input while keeping the others (shown in Table 8) constant as shown in Figure 34. The model suggests that as foil thickness increases, burr width also increases. This is a

consequence of the model requiring the force due to failure stress in the foil to be balanced by the adhesive bond. As the foil thickness increases, the force in the foil also increases leading to increased delamination and larger burrs. This behavior is physically valid so long as the foil has negligible bending stiffness as stated in Assumption 2. As the thickness increases, however, a point is reached where this assumption becomes invalid and the foil no longer bends as in Figure 20a. This limiting thickness is expected to depend on the machining forces involved as well as the material of the specimen. For NiTi the value could be less than 150 μm based on available foil specimens, however, verification of this value is left to future work.

Burr width reduces as peel strength increases due to a reduced tendency for delamination. The burr width for a feed that causes chip formation (5-7.5 μm/tooth in this study), remains unaffected by the tool size as would be expected when the burr is formed due to material deformation at the tip of the tooth. For feeds less than the cutting edge radius (<5 μm/tooth), the burr size would be proportional to the tool radius since the foil rips in the middle of the groove with no chip formation (Figure 20b, Figure 23c). A material with a lower ultimate tensile strength of 300 MPa (material number 2) would not require a large force to cut as compared to NiTi (material number 1), leading to reduced delamination and smaller burrs while a highly ductile material with a failure strain of 0.3 (material number 3) would result in much larger burrs because the material would deform more before it fails at the tooth tip (Table 9). The effect of using a material with a lower ultimate tensile strength and higher ductility (e.g. copper, material number 4) leads to almost similar sized burrs as NiTi due to a compensation caused by the opposite trends of these two material properties.

Table 9: Material properties used in generalization

Material number	σ_f (MPa)	ε_f (%)
1	1400	14
2	300	14
3	1400	30
4	300	30

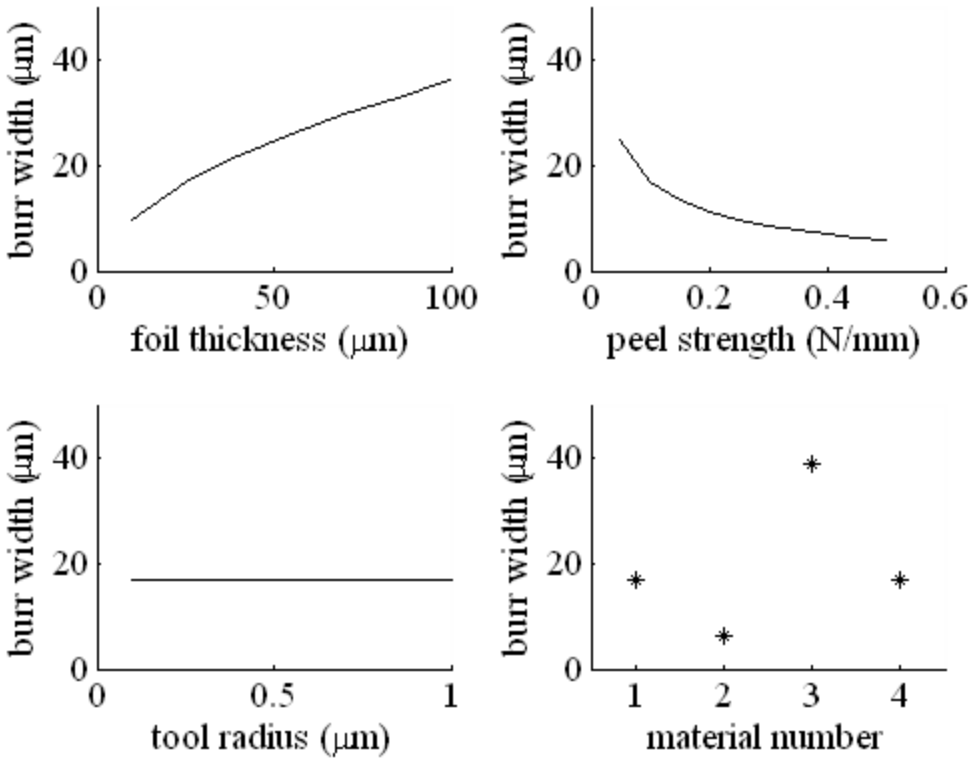

Figure 34: Effect of model parameters on burr size

Conclusions

This chapter focused on presenting a fundamental understanding of the mechanics of burr formation in micromilling of a thin nitinol foil adhered to a backing material. The following conclusions can be drawn:

- Burrs are formed due to ploughing as the tool initially penetrates the foil, delamination and insufficient chip thickness. If initial penetration is

sufficient to cause the foil to fail in tension, the foil tears with the crack starting closer to the upmilling side and thereby resulting in larger downmilling burrs. If penetration is insufficient, the foil plastically deforms until it tears typically at middle of the tool.

- The kinematic model developed captures the effects of feed per tooth, tool tip radius and adhesive peel strength to predict the burr width and is shown to be in good agreement with experimental data.
- At higher feeds, with a new tool and a strong adhesive bond, chips of the material are formed leading to very small burrs on either side of the groove.
- Three types of burrs were identified: rollover, feathery and wall type. Feathery burrs are produced only on the downmilling side while cutting with sufficient chip thickness and moderate bond strength with a new tool. Wall burrs are formed with worn tools at higher feeds due to moderate delamination on the downmilling side. Rollover burrs were formed in all other cases.
- The effects of spindle speed, feed, adhesive type, backing material, tool wear and side of groove (upmilling vs. downmilling) on burr height were studied. The effect of downmilling is most pronounced except in the case where there was significant delamination on the upmilling side.
- Wear of the tool results in larger burrs. Increasing the feed from insufficient chip thickness (< 5 μm in these experiments) to sufficient chip thickness (5 to 10 μm in these experiments)reduces the burr height if the tool is new, whereas it increases the burr height if the tool is worn.
- Spindle speed (strain rate effect) does not have a significant effect on the burr height for a new tool. For a worn tool, a lower spindle speed (more time for delamination) results in larger burrs.

- PMMA is softer and produces larger burrs and has a higher tendency for forming a built-up edge, which produces larger burrs.
- A weak adhesive bond with the backing material also leads to larger burrs.
- Variation in burr height is smallest for sufficient chip thickness, high bond strength and cutting with a new tool.

It is also seen that burrs cannot be eliminated even by varying feed over a wide range and devices produced by micromilling of thin foils would need to be subjected to subsequent deburring. Abrasive impregnated brush deburring could be a potential improvement over the abrasive slurry assisted brush process studied in Chapter 3 and is applied to grooves machined in foils in the next chapter.

CHAPTER 5

DEBURRING OF THIN FOILS

In this chapter experiments are conducted to study the mechanics of material removal during removal of burrs produced during micromilling of 25 μm thick NiTi foil using abrasive impregnated nylon brushes. High speed video images are used to capture the interaction of the brush bristles with the workpiece surface and burrs. Scanning electron images show the deformation and removal of material from the workpiece. The effect of brush speed and penetration on deburring rate is quantified. Understanding obtained from these preliminary experiments is used to create a model based on Hertzian contact mechanics under the action of brush stiffness and impact forces that can be used to predict deburring rate. This model is also used along with fracture mechanics to predict the number of brush passes required to deburr a groove edge. The accuracy of these models are verified experimentally.

Experiment Plan

Experiment Design

A schematic of the deburring process is shown in Figure 35. An abrasive impregnated nylon brush is spun while the workpiece is reciprocated with respect to it (Figure 35 a). The brush is positioned so that the bristles touch the burrs on the edge of the machined groove (Figure 35 c). Brush penetration Δ_n is defined as the distance the brush is moved normal to the workpiece surface after it touches it (Figure 35 d). The brushes used in this study are 0.75 inch, nylon brushes impregnated with FEPA grit 120 (109 μm) ceramic aluminum oxide grits (Scotch-Brite Mini Brush, 3M Corporation).

Each brush has 30 curved bristles that taper from 0.020 inches at the hub to 0.018 inches at the tip and are arranged staggered on each side of the hub (Figure 35 b).

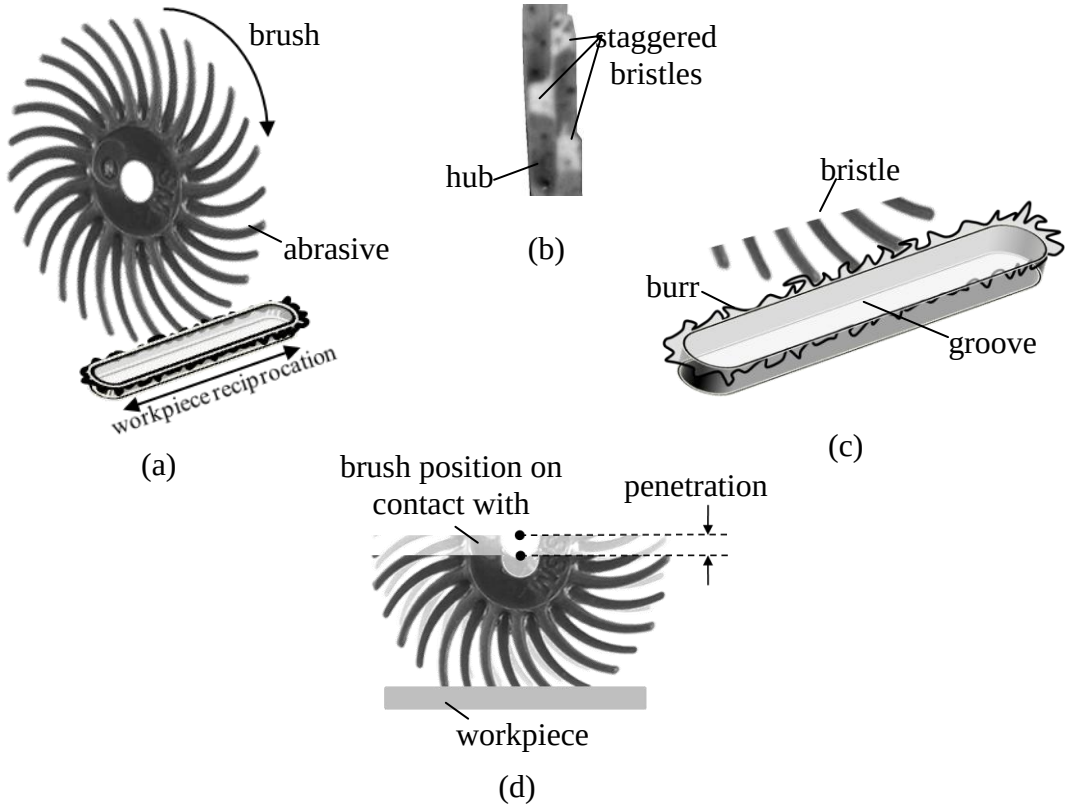

Figure 35: Schematic of deburring process (a) Elements of system (b) Detailed view of hub (c) Detailed view of burrs (d) Brush penetration

The experiment plan is shown in Table 10. Factors that affect material removal rate are decided based on prior work in brush analysis and abrasive polishing as workpiece material, workpiece reciprocation speed, brush matrix material, abrasive grit size, concentration, shape and attack angle [58, 60]. Most researchers who have studied deburring brushes have typically focused on brush speed and penetration [52, 54, 58, 63]. Brush penetration affects the force between the bristles and the workpiece and therefore the indentation of the abrasive. Low penetration results in lower forces and would reduce brushing efficiency. Excessive penetration would lead to the sides of the brush contacting the workpiece rather than the tips. It would also lead to excessive deflection of the bristle,

causing it to stray from the intended path along the edge of the groove. The industry practice for macroscale deburring with relatively larger brushes (above 4 inch diameter) is to penetrate the brushes to a maximum of 0.125 inches (~ 3 mm) [5]. The brushes used in this study are much smaller and for the same penetration would deflect away from the groove much more than typical industry brushes. Hence, after preliminary tests, penetration values of 0.5 mm and 1 mm were chosen for this study.

Bristle tip velocity affects the number of bristles passing over a particular region of the workpiece in a given time as well as the force on impact of the bristle tip on the workpiece and in turn, abrasive indentation. It is controlled by changing the brush rotation speed. The lowest speed in this study is 5000 rpm (2.36 m/s at bristle tip) and is set based on the lowest speed of the spindle used (Dremel 4000). The maximum spindle speed is limited due to excessive brush degradation at 15000 rpm (7.02 m/s at bristle tip). The workpiece material used in this study is a 25 μm thick, NiTi foil (55% Ni, 45% Ti, Johnson-Matthey Medical Components) with an austenite transition finish temperature of 50 °C. Workpiece reciprocation speed is held at 100 mm/s. Variation of reciprocation speed changes the number of bristles that interact with a burr. However, since this is already controlled using the brush rotation speed, changing the reciprocation speed does not provide any additional information.

Table 10: Experiment design

Factors	**Levels**	
Penetration (mm)	0.5	1
Spindle speed (rpm)	5000	15000

Experiment Procedure

Microgrooves, 500 μm wide and 6 mm long are machined with a single pass in 25 μm NiTi foil supported by gluing it to PMMA backing using cyanoacrylate adhesive (Figure 36a,b). The grooves are machined using a 500 μm, two-flute, endmill (PMT TR-

2-0200-S) spun at 60,000 rpm in a high speed spindle (SLF Faureuth, FS33-60) and fed at 1 μm/tooth. This feed, speed, adhesive and backing material combination is selected based on results of a prior study [102] to achieve relatively large burrs that would help accentuate the effects of the deburring process parameters. The grooves are milled on a laboratory micromilling set-up (Figure 17) which consists of three stacked high precision linear motor stages (Aerotech ANT4V, ALS130) with submicron resolution and accuracy.

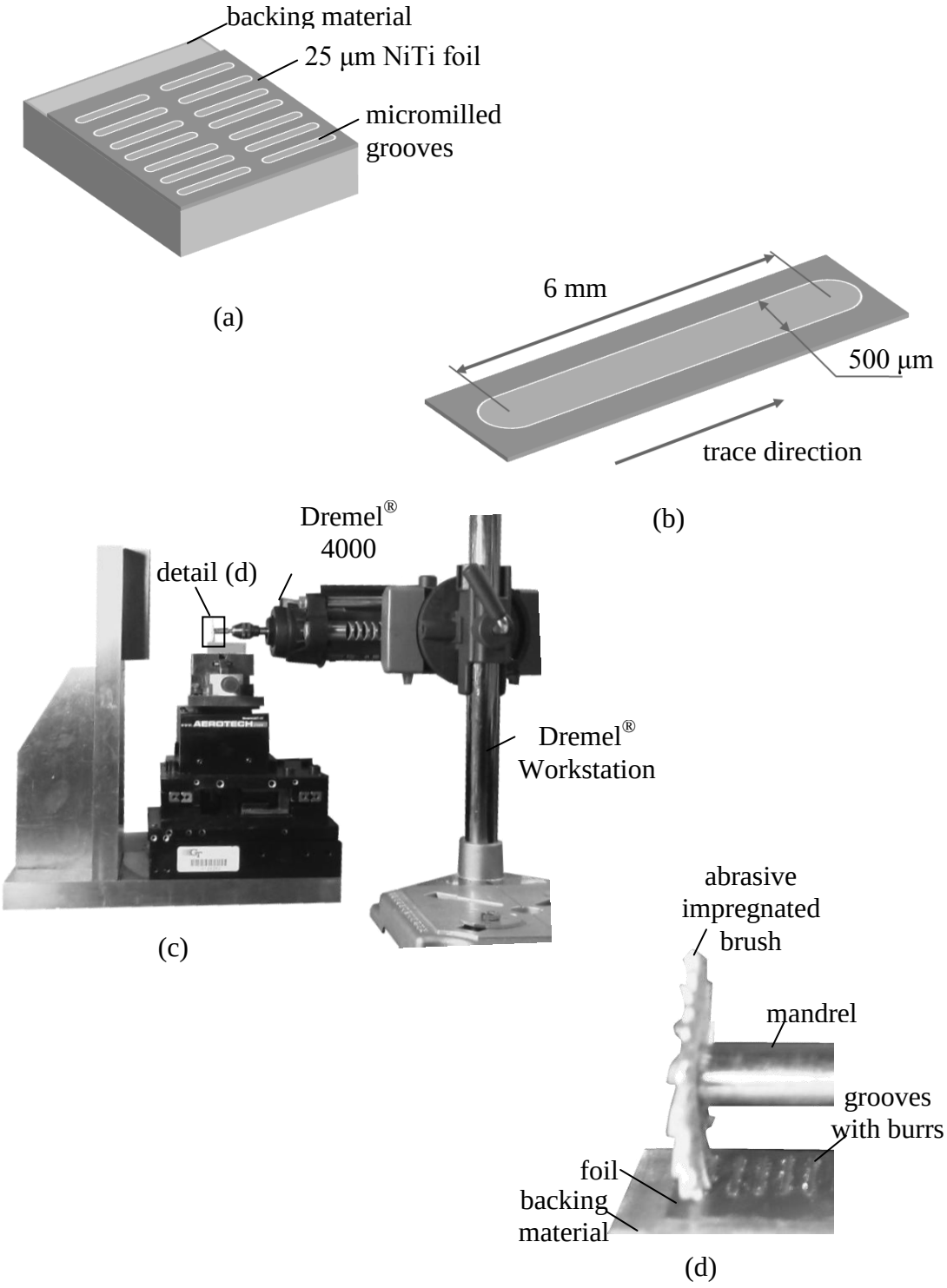

Figure 36: Experimental set-up (a) Workpiece to be deburred (b) Groove dimensions (c) Deburring set-up (d) Detail view of brush in set-up

Burr height on both edges of the milled grooves is measured using a stylus profilometer (Taylor-Hobson, Tallysurf 112) using a 800 μm spherical sapphire stylus positioned on top of the groove edge using a 50x microscope (Edmund Optics). Three parallel traces are taken 50 μm apart to ensure that the high points of the burrs are captured (Figure 16).

PMMA is a soft backing material and preliminary experiments showed that it deforms noticeably during deburring, warping the foil causing delamination and changes in the nominal penetration. Hence, the foil is then debonded from the PMMA backing using a solvent (Loctite XNMS), and bonded to an aluminum backing with cyanoacrylate adhesive in preparation for deburring. The spindle and spindle holder in Figure 17 can be removed to accommodate a horizontal spindle (Dremel 4000) held in a spindle holder (Dremel Workstation) for deburring with an abrasive impregnated nylon radial brush (Figure 36c and d). The brush is rotated at a speed to obtain the required tip velocity (Table 10). The brush is adjusted so that it just touches the workpiece and penetration is controlled using the nanopositioning stages. Upmilling and downmilling sides of the groove are deburred individually.

Earlier studies [95, 103] showed that burrs are removed in two phases. The first phase involves burrs breaking off leaving a burr root which in the second phase is either flattened plastically or abraded away. Hence, the grooves in this study were deburred in two phases each involving one reciprocation of the workpiece at 120 mm/min (Figure 35a). Preliminary experiments showed that the foil edge warps during deburring due to plastic flow of the material. The residual burr root at the end of the second phase was too small to be accurately separated by the stylus profilometer from the warpage but could be identified using a white light interferometer (Zygo NewView 200). Hence, interferometer measurements were taken after the first and second phase of deburring. Burr height after the first phase was also measured using the stylus profilometer to compare it with readings before deburring. It may be noted that reflectivity of burrs improves after

brushing making them detectable by interferometry. Unbrushed burrs have poor reflectivity and cannot be detected by white light or laser interferometry and need to be measured by a stylus profilometer. Burr height change at each point along the groove was calculated at the end of each phase for the different deburring conditions shown in Table 10. Each condition was replicated three times. Scanning electron images (Hitachi S-3700N) were also taken of the grooves before and after each phase. Foil thickness change in the brushed region at each phase was measured by placing the foil in between a ground tool steel block and an electronic indicator (Mhar Extramess 2001) with a 1 mm diameter spherical carbide ball tip. Surface roughness of the brushed region was also measured before and after each phase.

High speed video recordings were used to capture bristle interaction with burrs and also with a flat surface. Material removal rate was quantified by running the brush on a foil strip without grooves adhered to an aluminum backing with cyanoacrylate adhesive at the different conditions in Table 10 and noting the time and location of complete penetration though the thickness of the foil. Red die was applied on the backing material to aid detection of penetration under a 50x microscope (Edmund Optics). The workpiece was not oscillated to capture and explain the behavior noted in [58] of the location of highest brush force shifting from the middle of the brush contact area to the beginning of the contact area with increase in brush rotation speed. Three replications were conducted in these experiments.

Experimental Results

Bristle Characterization

Figure 37a shows a 3D confocal microscope (Olympus LEXT) images of a brush bristle that has been sliced in half along the length to expose the grits. It can be seen that there are only one or sometimes two large abrasive grits per section along the length of

the bristle. The grits are randomly shaped but have rounded points (Figure 37b). Although the brushes are specified as FEPA 120 (109 μm), abrasive grits as large as 180 μm and as small as 40 μm are seen. Comparison of a bristle before and after brushing (Figure 37c and d) shows that the bristle contact area is on side that is closer to the hub at the region A shown in Figure 37a and c. The reason for this asymmetric tip wear can be understood from Figure 37d and e which show high speed images of the brush in contact with the foil. It is seen that the bristle not only deflects vertically in the plane rotation, but also laterally out of the plane, touching the foil only on the side close to the hub. Wear of the nylon exposes the embedded grits leading to material removal. Some of the nylon delaminates from the bristle but remains attached to it and can interfere with the grit contacting with the workpiece. The high speed images also show that there is no detectable bristle 'bounce' [50] probably because the bristles in this study are thicker, shorter and therefore, stiffer than those typically seen in radial brushes for macroscale applications. No interaction between the bristles was seen as they traversed the foil surface due to the gap between them and the staggered configuration which improves the consistency of the process.

The static stiffness of the bristle was measured by mounting a brush with only one bristle in the spindle (Figure 36d) with the bristle tip touching a precision weighing scale (AWS AMW-100) which has a least count of 10 milligrams (~0.1 millinewton). The stage is moved up in increments of 100 μm and the reading on the scale is noted and the stiffness calculated as a function of deflection (Figure 38). The plot shows a clear nonlinear trend as would be expected with a curved beam that is deflected over 15% of its length and allowed to deflect in the lateral direction. A third degree polynomial was fit to the data and is used to model the normal force F (in N) of the bristle (Figure 38a) as a function of penetration Δ_n (Eq. **21**, Δ_n in mm).

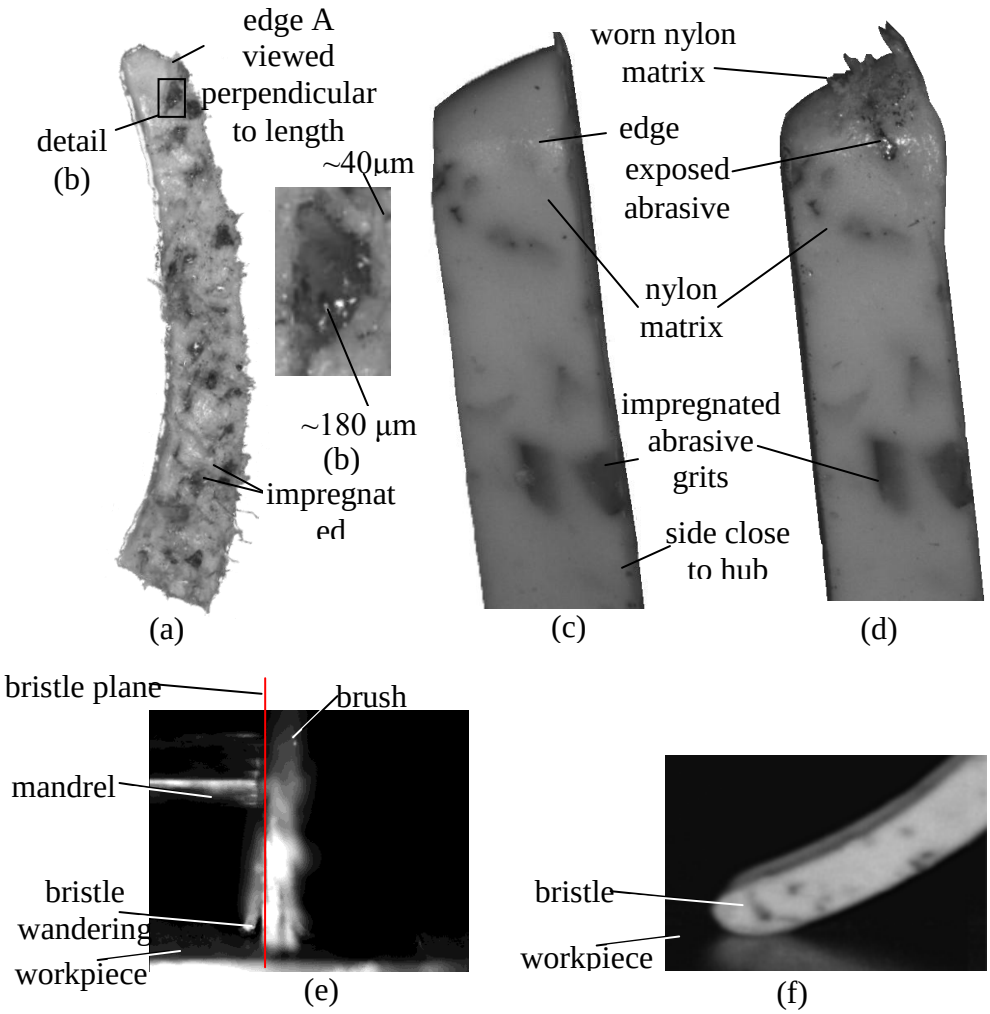

Figure 37: Abrasive impregnated bristles (a) Bristle sectioned along length (b) Impregnated grits (c) Bristle tip before brushing (d) Bristle tip after brushing (e) High speed image of brush (f) High speed image of bristle

Further experiments were conducted on the influence of spindle rotation speed on stiffness to capture any dynamic or centrifugal stiffening effects [104] on the same set up as for the static stiffness except the weighing scale was replaced by a dynamometer (Kistler 9256C2). The single bristle brush was rotated and penetrated according to the conditions in Table 10 with three replications and the measured forces were recorded at 30kHz sampling frequency. The maximum peak-valley forces for all recorded data sets

and their means were calculated. Standard deviations of these mean values were calculated for each set of replications (Figure 38b). The normal force increases from about 0.1 N to 0.14 N when brush penetration increases from 0.5 mm to 1 mm at 5000 rpm. From Figure 38a it can be concluded that the brush normal force due to the static stiffness would increase from 0.09 N to 0.11 N for the same change in brush penetration. Since both these values are close to eachother (especially given the standard deviation in Figure 38b), it may be concluded that at 5000 rpm, the normal force is determined mainly by static bristle stiffness.

The force values at 15000 rpm indicate that the force reduces with increase in speed. Although a probable explanation is that the reduction in force could be due to flaring of the bristles, this was not visible in the high speed video footage. A more likely explanation is that at higher speeds, impact forces dominate and excite the natural frequencies of the dynamometer (~4.6 kHz) leading to erroneous force measurements.

$$F = 0.24 - 0.496\Delta + 0.371\Delta^2 + 0.002\Delta^3 \quad \textbf{(21)}$$

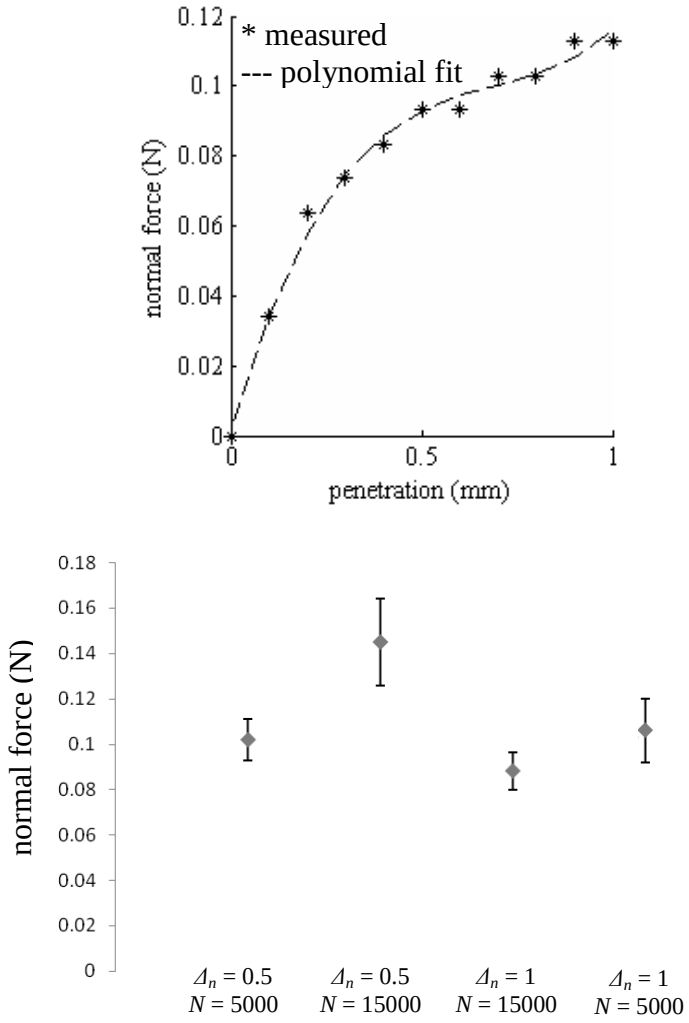

Figure 38: Bristle stiffness (a) Normal force vs. penetration Δ_n (b) Normal force as a function of spindle speed and brush penetration Δ_n

Material Removal in Brushing

A single bristle brush was used to brush a strip of foil that was polished with reducing abrasive size upto 50 nm alumina grits to remove the pickled surface finish which interferes with identifying the brush marks. Brush marks after 20 milliseconds of brushing at 15000 rpm and 1 mm penetration were observed under a SEM and show both ploughing marks and chip formation (Figure 39a and b). Shallow ploughing marks are

seen which may be credited to the smaller grits in the bristle (Figure 37b) or to bristle wandering (Figure 37e) which would lead to a reduction in penetration of even the larger grits. Deeper ploughing marks from the larger grits in the bristle are also seen with ridges. Some brush marks are seen to be angled to the rest of the strokes indicating bristle wandering. Although few chips are seen attached to the brushing marks, it is difficult to conclude as to whether ploughing (with no material removal) or chip formation (material removal) is the dominant mechanism of grit-material interaction. It has been suggested that material removal in chemical mechanical planarization (CMP) can occur at the intersection of two ploughing marks due to shear segmentation when the material that is ploughed up by an abrasive grit reaches the edge of a pervious ploughing mark and gets detached from the workpiece [105]. Another possibility for ridges as seen in Figure 39b is that they are pushed up by an abrasive and removed by the impact of a subsequent abrasive or by the motion of the nylon matrix.

Foil strips were brushed with an unaltered brush (no bristles removed) until they penetrated the entire thickness of the foil. The time taken for complete penetration at any point as well as the location of penetration in the brushed region was noted for all the conditions in Table 10 with three replications. SEM images of a foil brushed at 15000 rpm with 1 mm penetration show that complete penetration of the foil occurs repeatably at the start of the brush mark (Figure 39c). Two points are noticed corresponding to the position of the staggered bristles. The brush marks are much wider at the first point of contact of the bristle and foil that for the rest of the stroke indicating a deeper indentation that is attributed to impact forces. Further weight is added to this conclusion by noting that the first point of full penetration occurs at the middle of the brushed region when the spindle speed is reduced to 5000 rpm.

Multiple impact points are seen for different bristles due to slight variation in their lengths during manufacturing. Material flow away from the impact points can be seen close to the point of complete penetration (Figure 39c). The material flows over the

unimpacted material behind it forming a ledge-like shape which is then broken by subsequent bristles forming debris. Cracks are also seen at the interface of different flow regions. Material could also be removed when these cracks intersect. Towards the middle of the brushed region (Figure 39e), plouging marks with ridges are seen similar to Figure 39b and material deforms and may be removed as discussed in the preceding paragraph. Brush and foil debris are typically flung away from the brushed region due to the centrifugal force of the brush but can be captured using an adhesive layer at the end of the brush stroke (Figure 39f). Most of the debris seen are believed to be nylon fibers due to their glow which is characteristic of nonconductive materials in SEM images. There could however be some foil debris in it however that could also be glowing because they are insulated from the sample holder by the adhesive layer.

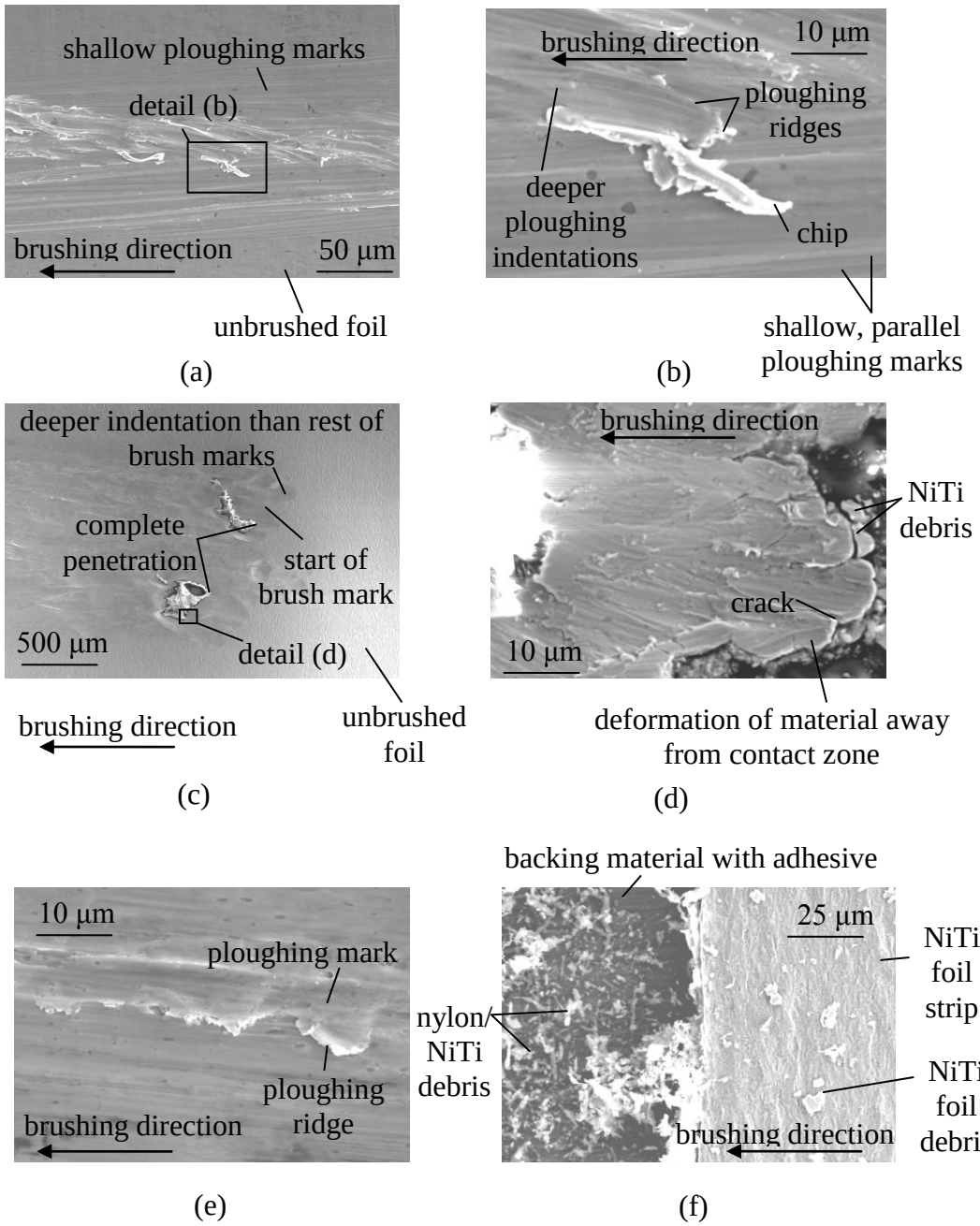

Figure 39: Material removal from foil without grooves (a) Brushing of foil (b) Chip formed during brushing (c) Complete penetration of foil at initial contact zone (d) Material flow close to initial contact zone (e) Ploughed material away from contact region (f) NiTi and nylon debris

Time for complete penetration of the foil thickness reduces with increase in brush rotation speed (Figure 40). This is to be expected since increasing the brush rotation speed increases the tip velocity and therefore, the impact force and indentation depth per bristle. For a constant workpiece reciprocation speed, it also increases the number of bristles interacting with the workpiece which would lead to faster material deformation or removal. Penetration is caused by the normal component of the rate of change in tangential momentum. This normal component increases as the bristle penetration Δ_n increases (Figure 40b). At lower spindle speeds, the effect of brush penetration is not noticeable. The point where the foil is completely penetrated also shifts away from the beginning of the brushed region to the middle of the brushed region indicating that impact forces are no longer dominant. At the middle of the brushed region, deflection of the bristle is maximum (Figure 40b) and hence, at these speeds, bristle stiffness is assumed to be responsible for penetration, a conclusion that is further backed by Figure 38a and b. An increase of brush penetration from 0.5 mm to 1 mm increases the bristle normal force only by 0.04 N (Figure 38b) which may not result in a significant increase of foil indentation and therefore, time for complete penetration of foil thickness.

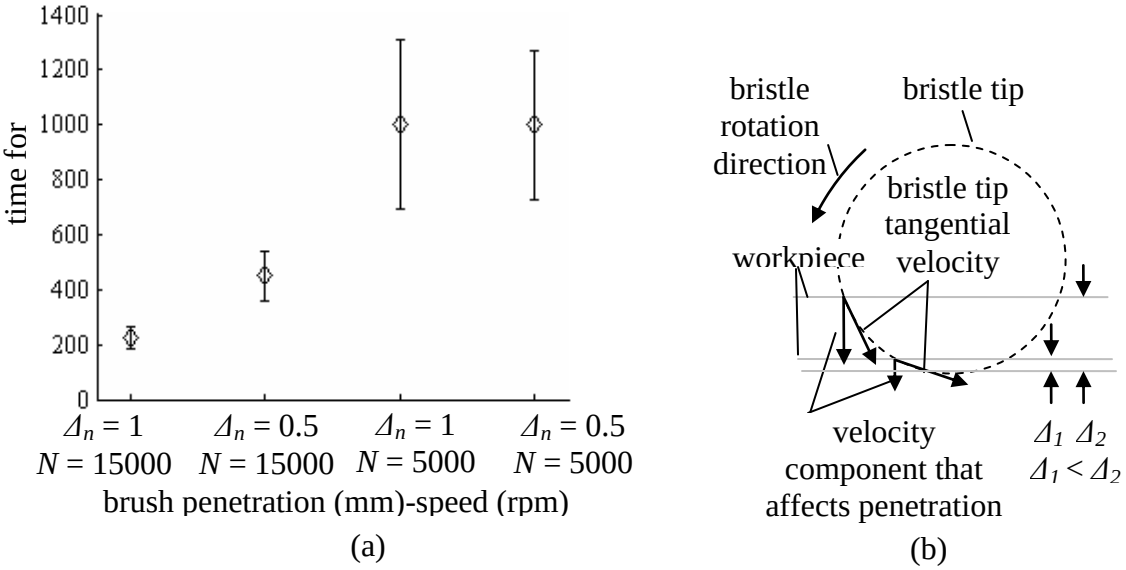

Figure 40: Parameters affecting material removal in brushing. (a) Effect of speed and penetration depth on time for complete penetration of foil (b) Effect of penetration on contact speed.

Qualitative Assessment of Deburred Grooves

Figure 41 shows a groove deburred at 15000 rpm and 1 mm penetration after the first phase. The burrs are typically long and slender, attached to the groove edge at the root. It can be seen that most of the long burrs have been removed on both sides of the grooves within just one reciprocation. This demonstrates the capability of the process to quickly remove large burrs. It also suggests that deburring rate is Some residual burr is seen on the upmilling side. Brushing marks are seen on the surface of the foil except close to the edge where the burrs shield the surface from the bristles. It is interesting that while the burrs initially are larger on the downmilling side, the residual burrs for this groove are on the upmilling side, although this is generally not the trend. Furthermore, the residual burrs are flattened onto the foil surface under the action of the bristles. This suggests that while the long burrs break off from the groove edge (Figure 42), short burrs are stiffer and have a tendency to flatten instead of breaking off.

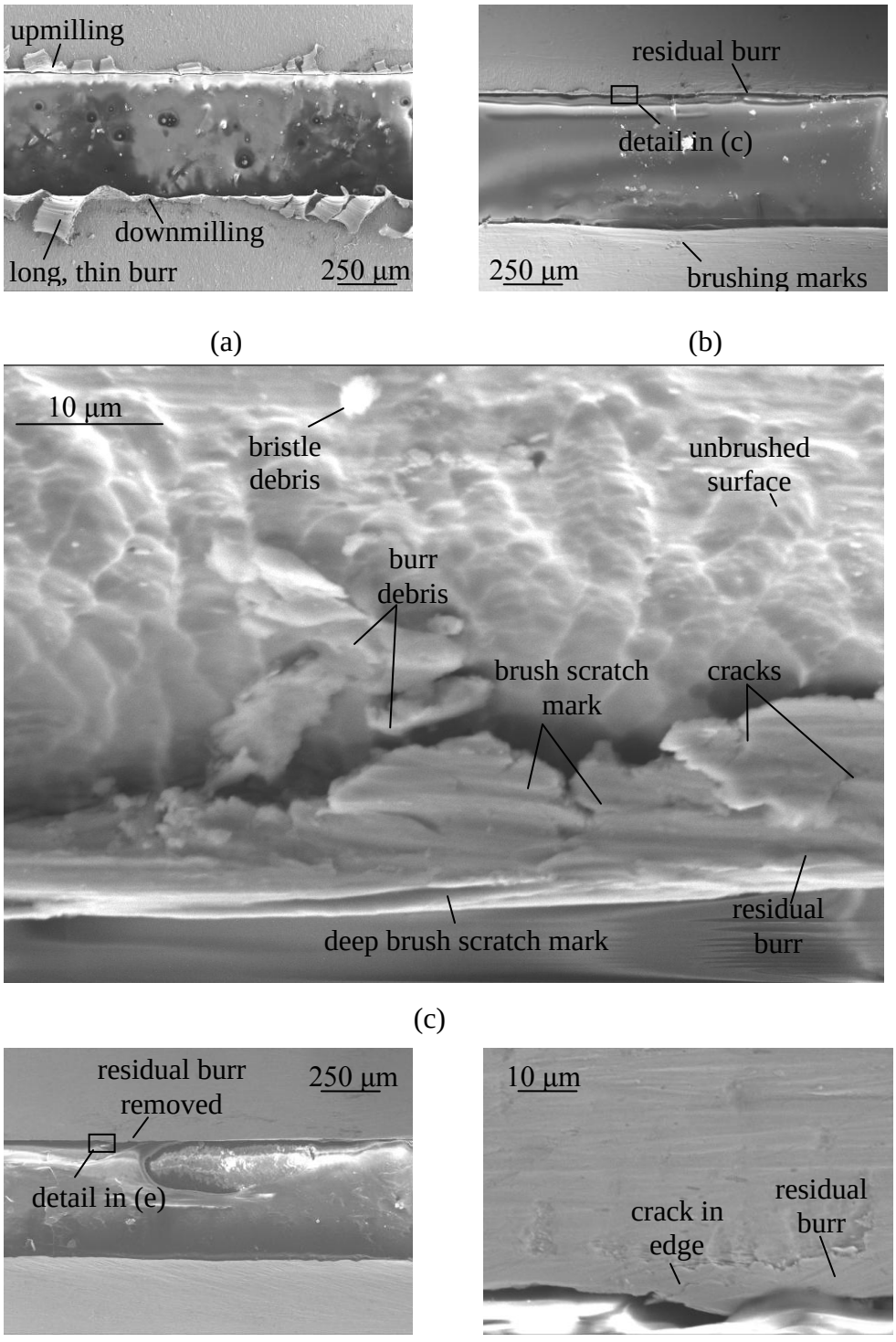

Figure 41: SEM images of grooves before and after deburring (a) Before deburring (b) After two passes (Phase I) (c) Detailed view of edge after two passes (d) After two more passes (Phase II) (e) Detailed view of edge after two more passes

Figure 41c shows a highly magnified image of the residual burr. Debris of the burr and the bristle are noticed and can be differentiated by the glow on the nylon since it is nonconductive to the electrons from the SEM. Cracks originating from the burr edge are also seen along with brushing marks and a particularly deep brushing mark. These observations suggest that for residual burrs, the abrasives cause scratch marks which form cracks at the edge. These cracks propagate under the cyclic loading of the bristles until they intersect with the burr edge or another crack, removing a chunk of the burr seen as burr debris. The process continues until the entire residual burr has been removed (Figure 41d and e). A few microcracks are seen along the length of the groove after Phase II. Residual burrs are seen after Phase II for milder brushing conditions (5000 rpm, 0.5 mm nominal penetration) but are absent for higher speeds and penetration (15000 rpm, 1 mm nominal penetration).

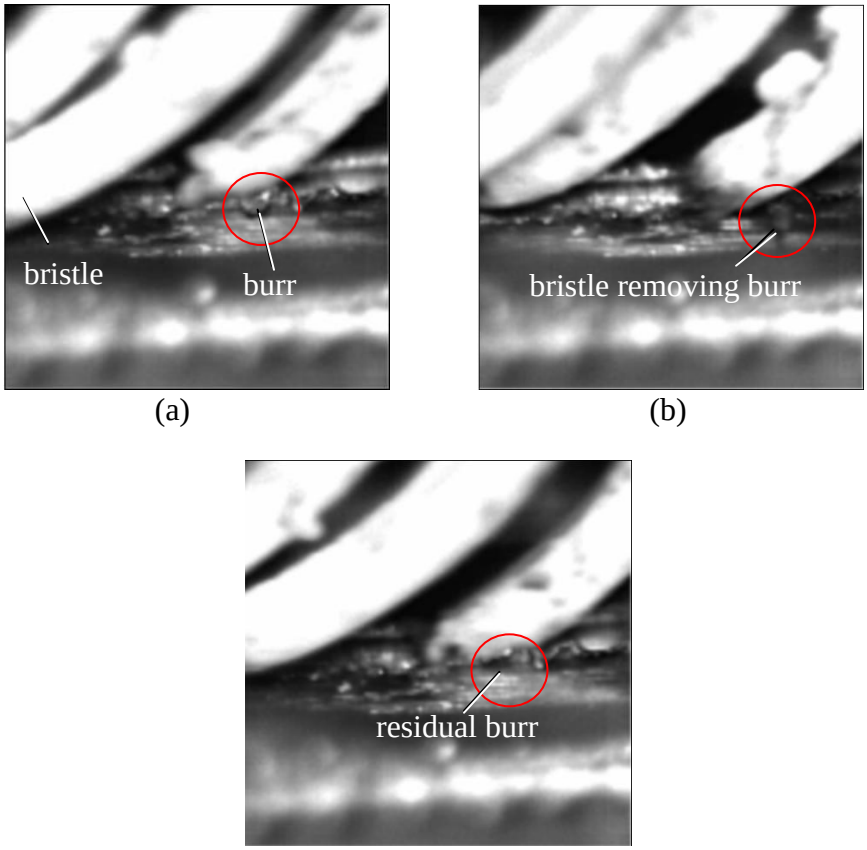

(a) (b) (c)

Figure 42: Mechanism of burr removal (a) Before bristle passes (b) Bristle removing burr (c) Burr removed

Effect of Deburring Parameters on Deburring Rate

Burr height reduction rate y is defined as the change in burr height Δx at any point for a given time that the groove interacts with the brush Δt. In this study, as described on page 7, deburring is carried out in two phases each consisting of one reciprocation of the workpiece at a constant feed of 120 mm/min. Since the grooves are 6 mm long, and the brush traverses twice this length in one reciprocation, the time for each phase is constant at 6 seconds. The change in burr height Δx along the groove at the end of each phase for all the replications of deburring parameters (Table 10) was calculated from burr height

measurements before and after each phase. Deburring rate was then calculated using Eq. **22** for the constant Δt of 6 seconds.

$$y = \frac{\Delta x}{\Delta t} \quad \textbf{(22)}$$

An analysis of variance was conducted using Minitab® for the 200 highest burr measurements after each phase for each condition in Table 10 (a total of 800 runs). Based on the results of a pervious study [103] burr height before deburring at each phase is considered as a covariate while analyzing the effect of deburring parameters. The results show that initial burr height x, penetration ΔN and spindle speed N are significant at $\alpha = 0.05$ for both phases. The speed-penetration interaction term is significant for the first phase but not for the second. Main effects plots cannot be obtained for this data due to its dependence on the initial burr height. The coefficients of the regression equations however suggest that penetration has a higher effect on the burr height reduction rate (Eq. 23 for Phase I and Eq. 24 for Phase II).

$$y = -0.125 + 0.159\,x + 94.6 \times 10^{-6}\,N + 3.93\,\Delta_n - 0.72 \times 10^{-3}\,N\Delta_n \quad \textbf{(23)}$$

$$y = -1.362 + 0.146\,x + 26.7 \times 10^{-6}\,N + 0.895\,\Delta_n \quad \textbf{(24)}$$

For all conditions in this set of experiments, the change of thickness after both phases of deburring was a maximum of 1 μm. Surface roughness of the foil was measured before and after each phase and the change calculated for the different conditions in Table 10 (Figure 43). Surface roughness initially improves during Phase I because the abrasives smoothen the pickled surface of the foil. During Phase II however, the indentation of the abrasives cause a roughening of the surface (Figure 39c) and so the change in surface roughness is negative. Analysis of variance indicates that spindle speed has a significant effect in both phases while penetration does not. This could be explained by noting that the material removal mechanics shows a dominant effect of spindle speed. However, further experiments need to be conducted to understand this trend.

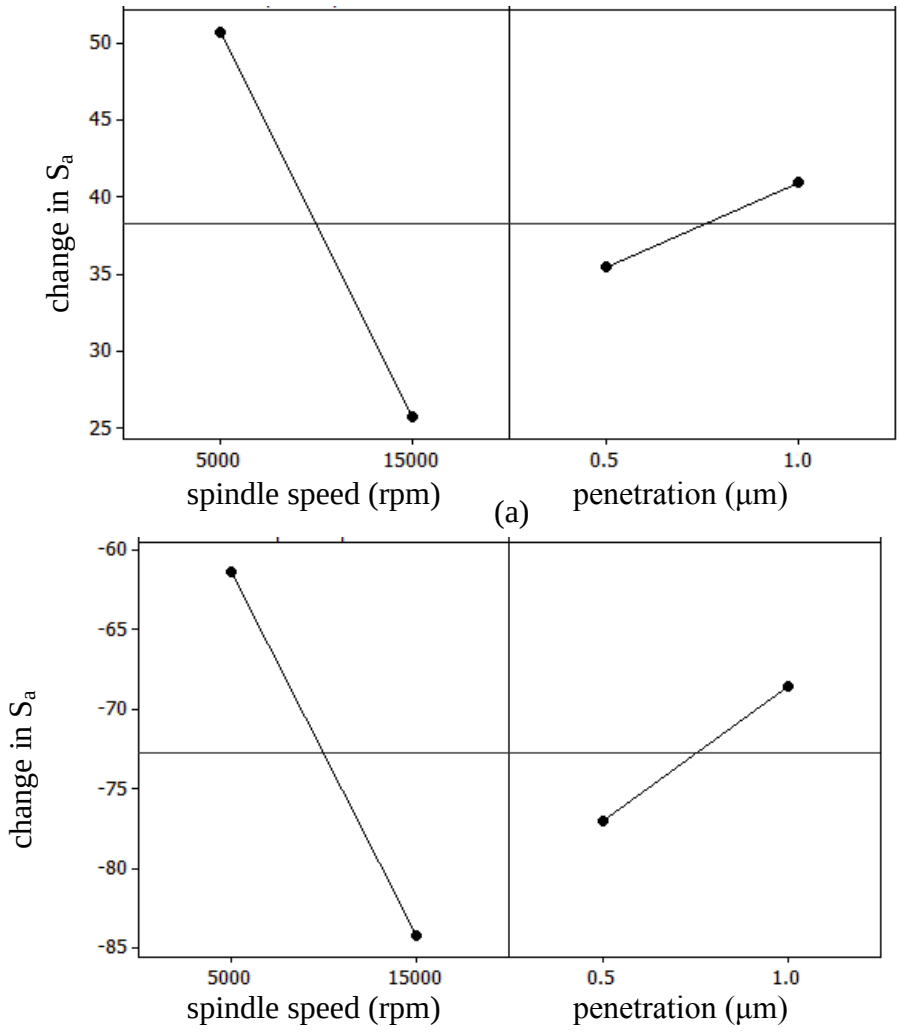

Figure 43: Effect of deburring parameters on change in surface roughness (S_a) of foil (a) Phase I (b) Phase II

Material Removal in Brushing

Hertzian Model for Brush Penetration Rate Though a Foil

Material removal in brushing is modeled based on Hertzian static penetration of a spherical indenter on a flat surface. The assumptions for Hertzian model are discussed in [106] and are summarized as:

1. The loads applied to the grits are static i.e. vibrations during initial contact are neglected.

2. The radius of the contact area is much smaller than the dimensions of the contacting bodies.
3. The contact surfaces are smooth (no friction effects).
4. The material is isotropic, homogeneous and linear elastic.
5. The deformations are small.

Assumption 1 is a reasonable simplification given that no dynamic vibrations were noted in the high speed videos. Since the loads in brushing are small with tangential force being much smaller than the normal force (Figure 44), the depth of indentation would be small and the force due to friction can be assumed to be small satisfying Assumptions 2 and 3. Assumptions 4 and 5 are simplifications given that the material shows superelasticity and the deformations are in the plastic region, however as pointed out in [106], it is common to use the Hertzian model in these applications as a first approximation. The Hertzian model underpredicts the penetration in the plastic zone because of the linear elastic assumption [107]. Strain-rate sensitivity of NiTi results in a further reduction of its strength [44], which would also cause the model to underpredict the penetration.

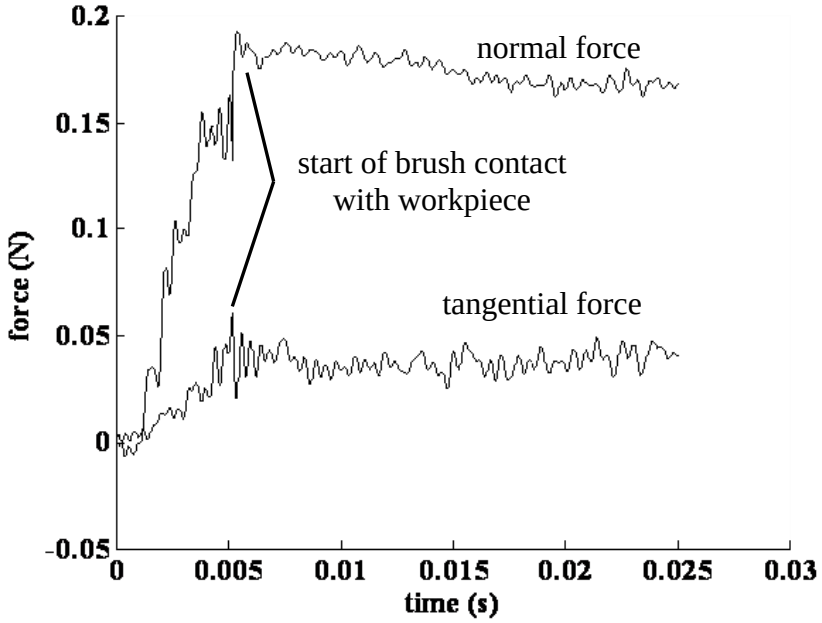

Figure 44: Brushing forces

The methodology used in this model is summarized in Figure 45. Images of the grits show that that they have an irregular but globular shape rather than sharp edges (Figure 37b). The sphere is assumed to have a diameter $2\bar{r}$ equal to the nominal grit diameter of 109 μm. Indentation force comes from the change in momentum of the bristle normal to the foil surface on impact with the foil F_i or from the stiffness of the bristle F_s. Impact force F_i is calculated by dividing the bristle into N_e elements and summing the momentum components normal to the foil surface. It is assumed that the impact has a coefficient of restitution C of 0.7 [108] and that the impact time t_i is the time taken for the bristle to move a distance equal to the tip width b while rotating at a speed ω in rps (Eq. 26).

$$\theta = \sin^{-1}\left[\frac{r - \Delta_n}{r}\right] \quad (25)$$

$$t_i = \frac{b\left(\frac{\pi}{2} - \theta\right)}{r\omega\, cos\theta} \quad (26)$$

$$F_i = \frac{C}{t_i}\sum_{j=1}^{N_e}\frac{m_b}{N_e} r_j \omega \cos\theta \quad (27)$$

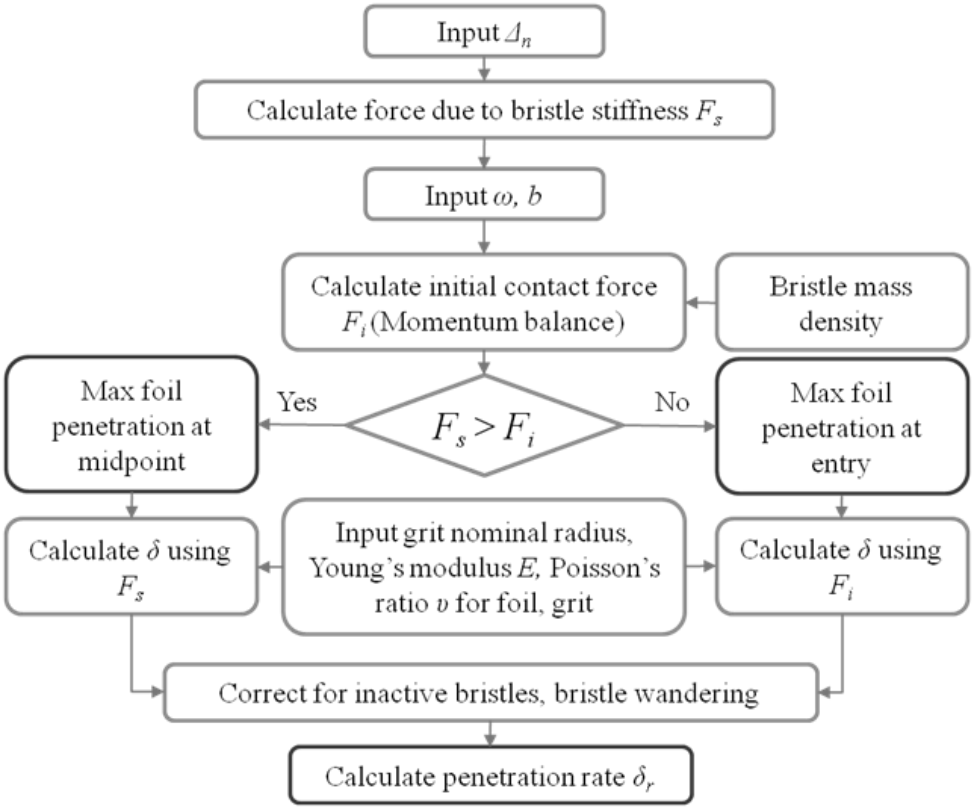

Figure 45: Schematic for calculation of penetration rate and location of penetration

Force caused by the stiffness of the bristle F_s us obtained experimentally (Figure 38a). This force is zero at the start of the contact area where impact force is maximum. On the other hand, impact force F_i is zero after the start of contact and stiffness force F_s reaches a maximum at the middle of the brushed area where it is deflected by the specified penetration Δ_n. In this model, both forces are calculated and the larger of the two is selected as the force F_n used to calculate the material penetration δ for a single bristle interacting with the foil (Eq. 28-30).

$$k_i = \frac{(1-\vartheta_i^2)}{\pi E_i} \quad (28)$$

$$k = \frac{4\sqrt{\bar{r}}}{3\pi(k_1 + k_2)} \quad \textbf{(29)}$$

$$\delta = \left(\frac{F_n}{k}\right)^{\frac{2}{3}} \quad \textbf{(30)}$$

It is observed in Figure 39c that the bristles do not impact the foil at exactly the same location but over an area *A* which can be measured from the SEM images. The probability of the grit indenting the same location is taken as the ratio of the projected area of indentation *a* to the impact area *A* observed in the SEM images. Observation of the bristles under a microscope shows that only half of the tips on the brush have exposed abrasives and would remove material. Penetration rate δ_r is calculated from Eq. 32 where N_a is the number of bristles that have exposed abrasives.

$$a = \pi\left\{2\bar{r}\sin\left[\cos^{-1}\left(\frac{\bar{r} - \delta}{\bar{r}}\right)\right]\right\}^2 \quad \textbf{(31)}$$

$$\delta_r = N_a \delta \frac{a\omega}{2\pi A} \quad \textbf{(32)}$$

Time taken for penetrating the 25 µm thick foil is calculated by dividing the foil thickness by δ_r and the results are compared with the experimentally obtained values in Figure 46b and reasonable agreement is seen. The model also shows that the normal force is determined by bristle stiffness at 5000 rpm while it is determined by impact force at 15000 rpm. Impact forces outgrow the stiffness force at about 11000 rpm for a 1 mm nominal penetration. Deburring rate is much quicker than that penetration rate of a flat surface due to the presence of cracks in the burrs caused during burr formation. It was found that all burrs along an edge were removed in four passes (two workpiece reciprocations, i.e. 12 seconds for a 6 mm groove) at 15000 rpm and 1 mm penetration. Note that the metric of number of passes is independent of changes in groove length.

Table 11: Inputs to brush penetration rate model

Quantity	Symbol	Unit	Value	Source
Brush radius	r	mm	9.52	measured
Bristle tip width	b	μm	457	measured
Coefficient of restitution	C	no unit	0.7	[108]
Mass of bristle	m_b	mg	2.2	measured
Number of bristle elements	Ne		10	
Poisson ratio AlO	ν	no unit	0.23	[109]
Young's modulus AlO	E	GPa	416	[109]
Poisson ratio NiTi	ν	no unit	0.33	[101]
Young's modulus NiTi	E	GPa	32	[77]
Grit radius	$\bar{r}$	μm	54.5	from manufacturer
Bristle spread area (15000 rpm)	A	mm^2	2.6	measured
Bristle spread area (5000 rpm)	A	mm^2	1.69	measured

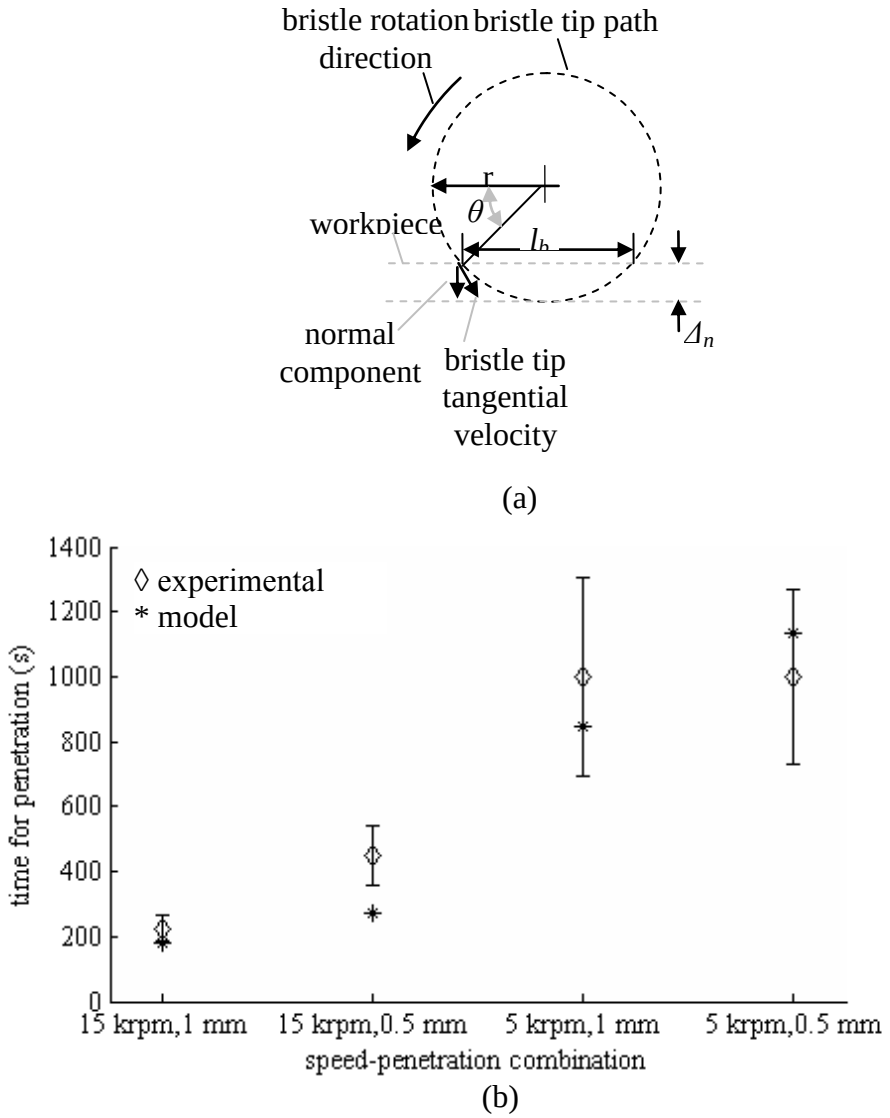

Figure 46: (a) Velocity components in brushing (b) Comparison of model and experimental time for complete penetration of foil

Fracture Mechanics Model for Deburring

Deburring rate during abrasive impregnated brushing of thin foils is obtained by modeling the burr as a thin plate with a crack in it (Figure 47b). The model uses the force calculations from the foil penetration model in the previous section and hence, the appropriate assumptions apply. The crack propagates under the action of cyclic loading

from the bristles. For thin foils, fracture of the long, slender burrs (Phase I) happens within one oscillation. However, it has been found that burr roots are much more difficult to remove [95, 110, 111] and Phase II determines deburring time. Figure 41c shows that the burr at the beginning of Phase II has been flattened onto the foil surface and is cracked along the edges. Action of the bristles results in a cyclic normal load F_n which induces a shear stress on the burr of thickness d_f and length b_f that is given in Eq. 33. Tangential forces are again assumed to be negligible (Figure 44).

$$\sigma_s = \frac{F_n}{b_f d_f} \tag{33}$$

Crack propagation in one pass of the brush over the burr is calculated by dividing the brush contact length l_k into segments Δl_k long (Figure 48). As the brush passes over the burr, the actual penetration Δ_i and therefore, the normal force due to bristle stiffness increases from zero until the burr is at the axis of the brush and then reduces again. For each segment at a distance f_i from the point where the brush just reaches the burr, the actual penetration Δ_i is calculated from Eqs. 34 and 35 and the normal force from Eq. 31.

$$\xi_i = sin^{-1}\left(\frac{l_k - f_i}{r}\right) \tag{34}$$

$$\Delta_i = r\cos\xi_i - (r - \Delta_n) \tag{35}$$

$$N_{int} = \frac{\Delta l_k}{f}\omega N_b \tag{36}$$

Propagation rate per cycle *db/dN* is computed from the Paris Law (Eq. 38) in facture mechanics and ΔK is calculated from the appropriate stress concentration factor K_{III} which is obtained from a handbook with K_{min} as zero [112].

$$\Delta K = K_{III} = \frac{2}{\pi}\sigma_s\sqrt{2\pi b} \tag{37}$$

$$\frac{db}{dN} = C(\Delta K)^m \tag{38}$$

Crack propagation per segment is calculated by multiplying the propagation rate in Eq. 38 by the number of bristles interacting with the burr N_{int} from Eq. 36 and process

is continued until $f_i = l_k$. Crack propagation due to impact force F_i is also added to obtain the total crack propagation in the first pass. If the crack propagation is less than the distance b_f between two cracks in the burr or the burr width, then the process is repeated. The total number of passes N_{pass} required for the crack to propagate the distance b_f is taken as the number of passes required to deburr the groove edge (Figure 48). Table 12 compares the predicted values for N_{pass} using values in Table 13 for the speeds and penetrations used in this study with those obtained in experiments and shows good agreement.

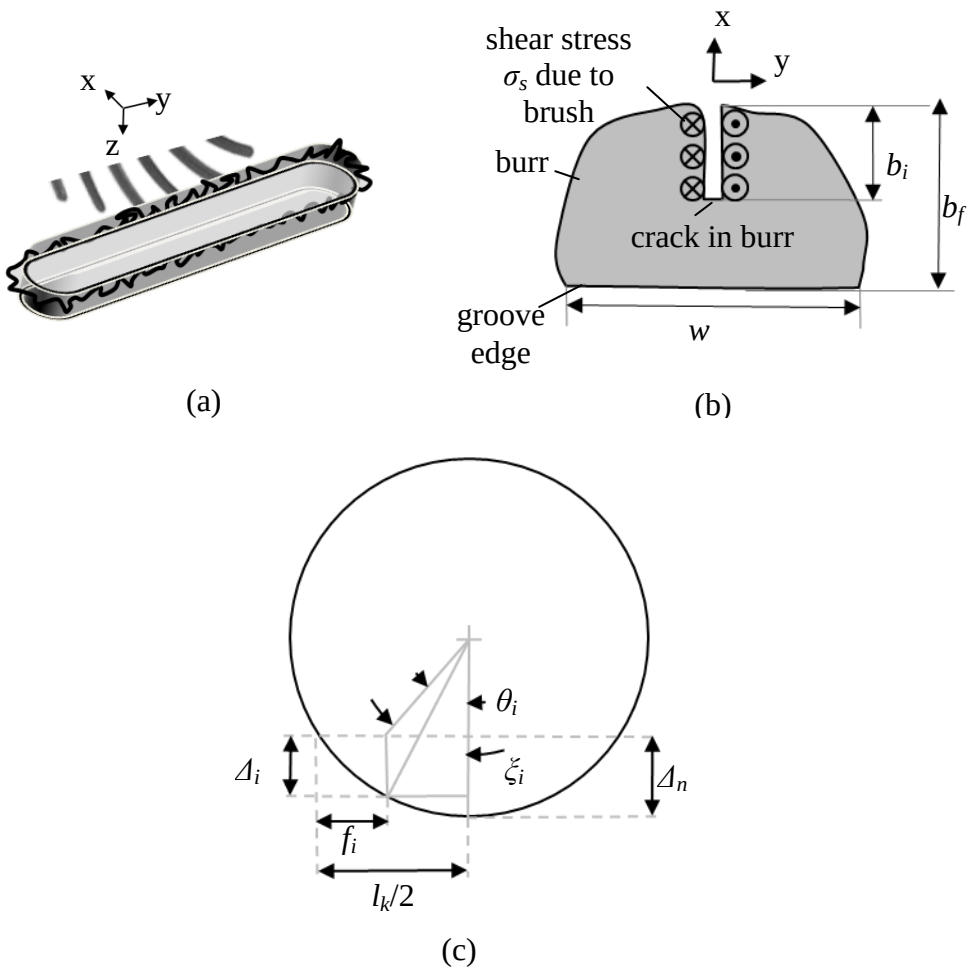

Figure 47: Deburring model parameters (a) Orientation of burr (b) Idealization of burr geometry (c) Calculation of instantaneous penetration as brush passes burr

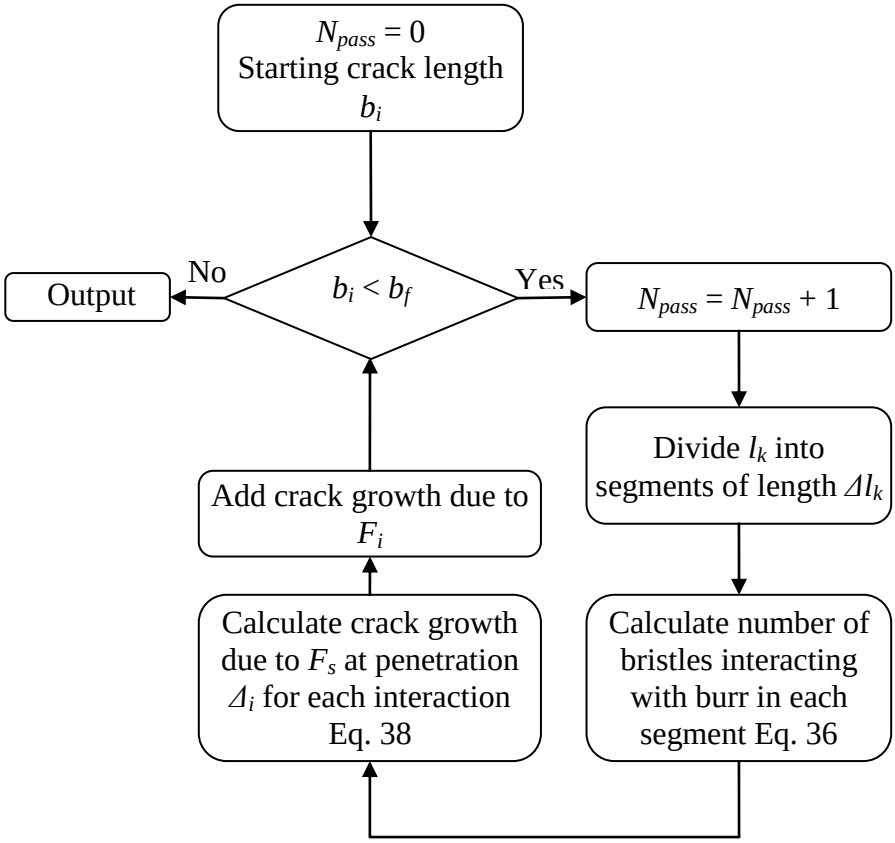

Figure 48: Deburring model process flowchart

Table 12: Comparison between predicted and actual number of passes for complete deburring

Spindle Speed (rpm)		**15000**		**5000**	
Penetration (mm)		**1**	**0.5**	**1**	**0.5**
Number of passes	**Model**	2	4	4	12
	Expt.	2	4	6	10

Table 13: Parameters used for predicting N_{pass}

Quantity	Symbol	Unit	Value	Source
Scaling constant	C	m/cycle/(MPa $m^{0.5}$)^m	1.88 x 10^{-11}	[113]
Scaling exponent	m		4.21	[113]
Initial crack length	b_i	μm	5	measured
Final crack length	b_f	μm	20	measured
Brush feed	f	mm/min	100	

Sensitivity analysis of the model with brush penetration set to 1 mm and brush rotation speed 15,000 rpm indicates that a larger initial crack size b_i results in a reduction in deburring time as would be expected. Reviewing the SEM images it is observed that most of the burrs have a width of less than 25 μm while the initial cracks in the root are at least 4 μm long. Hence, it is reasonable that cracks of about 8 μm would result in the burrs being removed in one pass. Based on these observations, it is very unlikely that there would be a burr with cracks of initial length less than 4 μm making the almost linear inverse proportionality of the prediction with reduction in b_i less of a concern. It is also to be noted that brushing the foil for an additional two passes would not severely affect the thickness of the foil and hence, is not a major concern. A similar logic applied to the final crack length b_f, shows that it is improbable for the current material to have burr roots larger than 25 μm. Over this range, the number of passes changes only by 1, which would not be detrimental to the feature size. C and m at 15,000 rpm and 1 mm penetration shows that the predictions change only slightly for most parameters (Figure 49). The range for each parameter is obtained from SEM images and the references indicated in

Table 13. The drawback with overestimating N_{pass} is the reduction in foil thickness, which in the present experiments is negligible. Equation 33 indicates that, as expected, the number of passes would increase with increase in foil thickness.

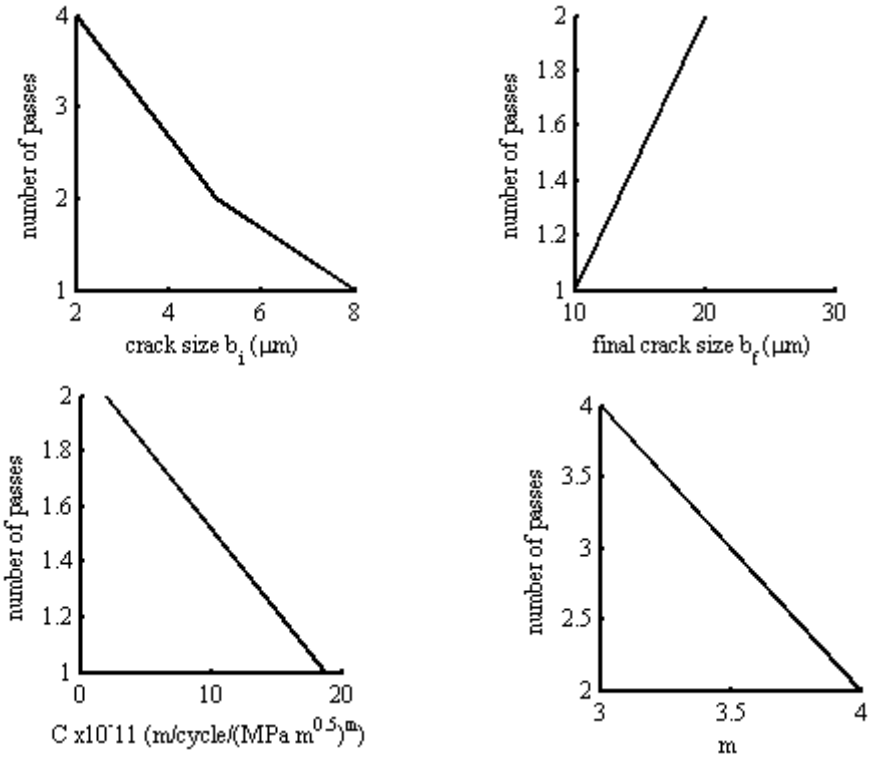

Figure 49: Sensitivity analysis. (a) Crack size, (b) Final crack size, (c) Material fracture constant *C*, (d) Material fracture constant *m*.

CONCLUSIONS

This study sought to shed light on material removal in abrasive impregnated brushing of metallic foils. The following conclusions are arrived at in this study:

- For brushing of a flat surface, some material is removed as chips by the grits. Material is also deformed by the grits and pushed up to form ledge like structures or microburrs which then break off due to the impact or stiffness forces of subsequent bristles.
- The maximum normal force and maximum indentation shifts from the middle of the brushed region at 5000 rpm to the entry region at 15000 rpm

due to a shift from a bristle stiffness dominated force to an impact dominated force.

- A Hertzian static indentation model used to predict indentation rate during brushing of foils shows good agreement with experiments.
- Burr removal occurs in two phases. Phase I involves fatigue fracture of the long slender burrs at the root. Phase II involves material being removed in flakes as the cracks formed during fracture in Phase I and new cracks formed during brushing propagate through the burr.
- A fracture mechanics model based on Paris equation can predict the number of passes required to deburr an edge and further supports the hypothesis that material removal in brushing is better described by fracture mechanics.
- Burrs can be removed within 12 minutes for a 6 mm long groove with no more than a micron change in foil thickness.
- Surface finish initially improves for the pickled foils used in this study during Phase I but subsequently degrades in Phase II due to impact of the bristles.

In the next chapter the knowledge of burr formation and deburring is applied to the micromilling of a device manufactured from a thin foil.

CHAPTER 6

DESIGN OF SURGICAL SUPPORT STRUCTURE

In this chapter, tissue manipulation devices currently used are described. The Pahl and Beitz systematic methodology of design is then used to address the needs of a tissue translocation device for surgical correction of AMD [114]. The four steps used for design are Task Clarification, Conceptual Design, Embodiment Design and Detail Design. Physical effects and working principles are presented in a morphological chart. They are compared with the requirements list to identify the principle solution. This solution is then fleshed out and auxiliary devices for use with the design are identified and developed. Detail Design, involves creating detailed drawings of the design and is not presented. However, the selected solution is manufactured and tested in-vivo and ex-vivo in a pig model.

Ocular Tissue Translocation Devices

This section discusses currently used tissue translocation devices in ophthalmic surgery. These devices are compared with the requirements for the new device.

Forceps

The most basic tissue manipulation device used in ophthalmic surgery is a pair of forceps. Lens insertion forceps have a clearance at the tip to grasp the tissue over a small area so that there is minimal damage to the graft. Miniature vertically acting forceps may be used to insert and manipulate the structures in the eye. They are easily introduced through one of the instrument ports made in the eye.

Lens Inserters

During cataract surgery, a foldable artificial lens is inserted into the eye to replace the cataract. One type of lens inserter is the Tan EndoGlide (Angiotech Pharmaceuticals) [115]. These are used to fold and insert the artificial lens into the eye through a small incision. The lens is placed on a compliant platform, then pushed in to the cannula causing it to roll up. The cannula is then inserted through a clear corneal incision and the platform is advanced into the eye to release the artificial lens.

Electro-Adhesive Forceps

Electro-adhesive forceps work on the principle of thermal adhesion of a tissue to a surface [79]. The forceps consist of an insulated probe exposed at the tip, which acts as one electrode in the circuit. The second electrode is usually larger and can be placed anywhere in the operating field such that the electrical circuit can be completed. The probe is touched to the tissue and an electrical pulse is applied between the two probes. This causes thermal adhesion of the tissue to the probe via a hydrogen bonding mechanism. The tissue can then be translocated to the target location. A higher voltage is applied to cause ablation and detachment of the tissue from the probe. Adhesive forces on the order of $0.3x10^{-3}$ N were achieved with a 50 μm probe and chorioallantoic membrane of leghorn chicken embryos. A similar device based on electrically induced adhesion was developed to support an ocular tissue patch [14]. This device consists of two nitinol rings. One ring is placed below the tissue graft and the other is placed above the graft concentric with the first ring. The rings are then electrically heated to cause adhesion of the tissue to the rings.

Task Clarification

Following the Pahl and Beitz methodology, Table 14 summarizes the requirements for the tissue translocation device. The following sections discuss these requirements in detail.

Table 14 : Requirement list for tissue translocation device. D = Demands, W = Wishes.

D/W	Requirement
	Geometry
D	Insertable through 2 mm incision
D	Should not have protruding parts
D	Flat apposition surface
D	Hold a patch of tissue 3 and 5 mm in diameter
D	Structure should be less than 250 μm thick inclusive of 150 μm thick tissue graft
	Forces
D	Should be able to withstand manipulation forces during surgery
D	Should be able to prevent folding of tissue
D	Mechanical manipulation should be possible using small gage instruments
	Kinematics
D	Prevent rubbing of clamp against tissue
D	Motion should be smooth (not jerky or sudden)
D	Prevent tissue wrinkling or folding
	Material
D	Biocompatible, sterilizable
D	Should be capable of being implanted in the eye for many years
	Energy
D	Energy levels should not damage tissue graft
	Production
D	Should be suitable for batch or mass production
	Quality Control
D	Should pass FDA approval
D	Should perform successfully in ex-vivo and in-vivo pig models

Geometry

The device can be inserted into the eye through one of the 2 mm long incisions made for the 3-port pars plana vitrectomy procedure. The device may also be inserted

through a clear corneal incision. This approach has the advantage that the incision is self-sealing and is commonly used for inserting foldable intraocular lenses. The incision is made with the tip of a keratome and is typically slightly less than 3 mm in length. Larger incisions make it difficult to control the pressure inside the eye thus making it more difficult to control bleeding in the eye. Ideally, the device should have dimensions compatible with insertion through a small incision (2-3 mm). However, the size of the patch that needs to be translocated is about 3 mm for the pig model and 5 mm for procedures on humans. Hence, the dimensions of the device should be such that it can accommodate the graft without allowing it to fold. The presence of sharp edges and protrusions can significantly increase chances of inflammatory reactions and should be avoided. The translocation device will be left implanted under the retina after surgery and should be thin enough to be accommodated in the sub-retinal space.

Forces and Kinematics

During the production of the device and its use, it will be subjected to several forces. This includes manipulation forces during surgery, handling forces during sterilization, forces exerted by the tissue graft on the device and forces involved in the manufacture of the device. The device should be able to withstand these forces without damage. Instruments used in surgery are typically either 20, 23, or 25 gage and apply limited mechanical forces. Hence, if the device needs to be manipulated, forces should be within the mechanical limitations of small gage instruments. Surgery in the eye involves manipulation in a constrained space with a restricted view. Therefore, any motion of the device should be very smooth in order to avoid jerky manipulations within the eye. The cells of the RPE layer are extremely delicate and are highly prone to detach from the underlying Bruchs membrane, especially in elderly patients. Therefore, the device should not touch the RPE tissue designated for the fovea, or cause it to fold since this would damage the delicate RPE layer.

Energy

Any energy release associated with the working of the device should not adversely affect the tissue. The area of damaged tissue, if any, should be minimal, at most on the order of about 10% of the graft area. Energy levels depend on the energy density as well as the duration of exposure of the tissue to the energy source. As a reference, typical energy densities used for a pulsed excimer laser ablation of eye tissues are between 100 and 200 mJ/cm^2 [116].

Materials and Cost

An estimated 1.6 million Americans over the age of 50 suffer from AMD [17]. Hence, the device should lend itself to mass production or at least large-scale batch production while being relatively inexpensive. The material used for construction of the device should be biocompatible and be capable of either gas or steam sterilization. Typical steam sterilization cycles involve heating the instruments in a steam autoclave to about 140°C using steam at about 15 psi. Gas sterilization involves exposing the device to ethylene oxide gas at temperatures between 30°C and 60°C and is preferred for devices sensitive to high temperatures or UV radiation.

Comparison of Current Devices with Requirements List

A comparison of the currently used tissue translocation devices described in Section 0 with the requirements of the device to be designed reveals some deficiencies in the current designs. Miniature forceps are readily available and can be designed to avoid significant tissue damage due to their small contact area. However, they contact the tissue only at one point and cannot support an entire patch of tissue. Even if two forceps are used, they can only stretch the tissue patch between two opposite points and not along the entire periphery of the patch. Hence, after translocation, the graft tissue may fold over during the healing process. Electrified forceps suffer from some of the same drawbacks

as standard forceps resulting from the point contact. The nitinol ring design on the other hand contacts the tissue all along its periphery. However, in the process of aligning the two rings so that they are concentric, they can rub against the tissue and damage it. Also, aligning the two rings is difficult.

Similar to forceps, lens inserters cannot be implanted in the eye. Furthermore, they are designed for thicker tissues to prevent damage of one side of the tissue by causing it to fold without overlapping. On the other hand, the device to be designed is meant for tissues on the order of a few 100 microns, which need to be prevented from folding. They also contact the tissue over the entire area of the patch on one side of the tissue. This can also lead to significant damage of the RPE-Bruchs membrane graft and compromise functionality of the graft.

Design Problem Statement

The above discussion proves the need for a new device that meets the requirements listed in Table 14. In particular these devices are incapable of supporting an entire patch of thin tissue and prevent it from folding on itself. They also cannot be implanted in the eye permanently. An analysis of the requirements list suggests the following abstracted problem statement:

To design a long term ocular implant to support a patch of tissue while it is translocated.

This problem statement is represented as a function diagram in Figure 50. It is to be noted however, that moving the patch can be easily achieved using forceps if the tissue patch is secured properly. Hence, the design process mainly focuses on supporting the tissue.

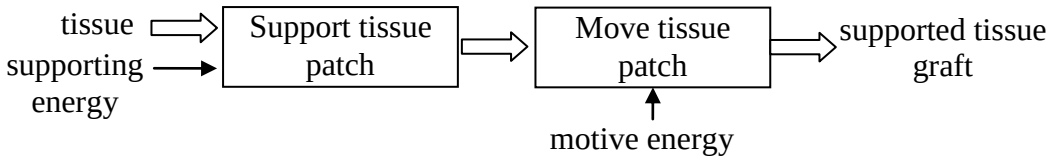

Figure 50: Function diagram for tissue translocation device

Conceptual Design

In this section, the solution to the foregoing problem statement is identified starting with the most abstract terms possible to avoid bias. This is done by starting with working principles in Section 00. These working principles are then compared with the requirements list to identify the principal solution in Section 00.

Working Principles

In-plane forces must be applied along the entire periphery of the tissue patch to support it. These forces must oppose any forces that might try to wrinkle the tissue. Folding or shrinkage forces can result from the elastic forces within the tissue, forces applied by the surgical instruments or the flow of liquid through the eye. Figure 51 shows a morphological chart for the different approaches to support the tissue patch. The following sections discuss these approaches in detail.

Friction

As illustrated in Section 0, most of the devices in ophthalmic surgery use forces arising from friction and mechanical interlocking to support tissue. Friction may be in the form of resistance offered by the surface of a pair of forceps. This approach has been modified for the tissue support structure shown in Figure 51a, b and c. All the designs are based on the idea of sandwiching the tissue between two stiff structures that support the tissue. The tissue is retained between the rings using friction between the rings and the tissue and hence, needs a normal force to be applied at the interface of the tissue and the structure. This normal force is supplied by compressing the tissue between the rings and

locking them in place using clasps or wedges (Figure 51a and b). The force can also come from the reaction forces due to elastic deformation of the structure (Figure 51c), similar to a paperclip. It is to be noted that the structure may be monolithic (Figure 51a and c) or consist of multiple parts (Figure 51b) that can be assembled inside or outside the eye. Figure 51c can also be modified by using a superelastic or shape memory material.

Mechanical Interlocking

Mechanical interlocking may also be used to support the tissue. This concept has been translated in practice as forceps where sharp ridges present on the tips bite into the tissue (Figure 51d). Figure 51e presents another possible solution shaped like Figure 51c that works similar to the electro-adhesive forceps discussed in Section 0. However, rather than depending on hydrogen bonds to generate the required force, this solution uses mechanical interlocking of the tissue with a textured surface of the support structure. The texture causes the tissue to enter the crevices in the gripping surface. When heat is applied to the surface, the tissue is dehydrated and shrinks onto the surface to form a mechanical interlock. It is to be noted that in this case there is no necessity for a normal force to be applied between the tissue and the structure.

Electrostatic Forces

The third approach to supporting the tissue is to use electrostatic forces to grip the edge of the tissue. Some have hypothesized that devices like the electro-adhesive forceps support the tissue by electrostatic forces such as hydrogen bonds [79] (Figure 51f). Commercially, electrostatic forces have been applied to achieve adhesive forces on the order of 0.5 to 1.5 N/cm^2 [117]. The lens folding devices utilize surface tension and viscoelastic fluids to resist relative motion between the lens and the folding device.

Bioadhesives based on electrostatic forces and van der Waals forces have also been used in drug delivery applications [118] (Figure 51g).

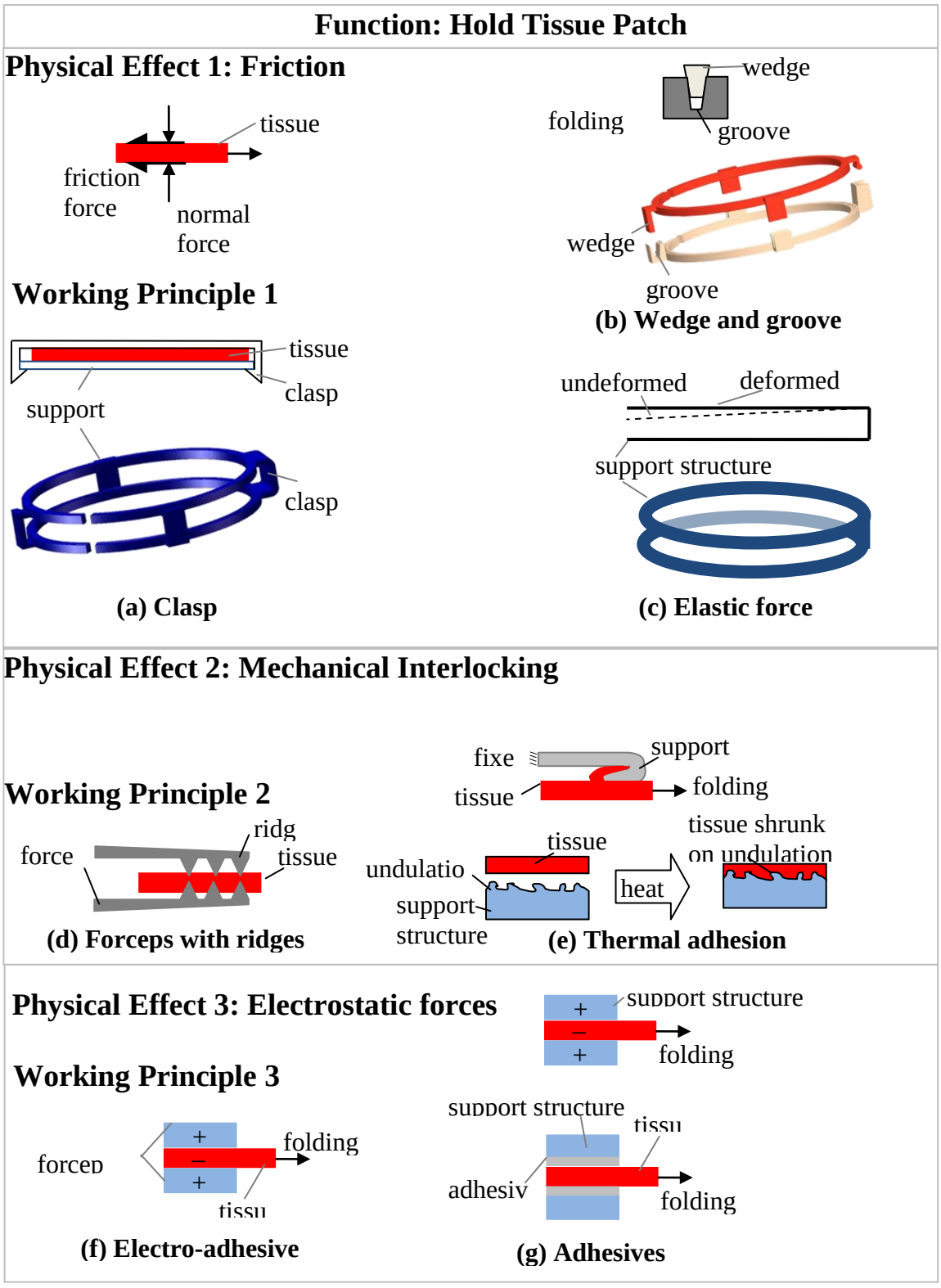

Figure 51: Morph chart for function 'Hold tissue patch'

Selection of Principal Solution

The possible solutions shown in Figure 51 are now evaluated with respect to the requirements list in Table 14 to identify the principal solution. All the solutions fulfill the requirements of geometry except the ridged forceps (Figure 51d). However, not all of them satisfy the other requirements as discussed in the following sections.

Electrostatic Forces

Electrostatic forces based on charge induction (Figure 51f) would be difficult to use for a permanent bond between the tissue and translocation device since this would require a permanent supply of electric charge to the device. Moreover, the device would discharge through the body or the saline solution used in the eye. Bioadhesives (Figure 51g) quickly clump together in the eye and do not allow sufficient time for application to the tissue being translocated. This suggests that it would be best to pursue a solution based on mechanical interlocking or clamping.

Friction

Microscopic polymer structures have been created using micromolding [119] and micro-SLA [120]. Photopolymers for contact lenses, such as polyvinyl alcohols, can be fabricated using micro-stereolithography. Micromolding could definitely be used to manufacture the devices shown in Figure 51a and b. However, polymers are too weak or compliant for the dimensions under consideration.

There is however, a trade-off in flexibility that is involved in the design of the device. The material would need to be sufficiently stiff for the clasps to remain closed. If the material is too flexible, it will tend to bend and slip out of the clasps. However, if it is too stiff, it cannot be rolled up to insert it through the 2mm incision. The approach in Figure 51c also suffers from low elastic forces generated by the small dimensions

required for this device even if it were fabricated out of metal. In short, although all the designs satisfy the geometric requirements, designs in Figure 51a, b and c do not satisfy the force requirements. Furthermore, manufacture of micromolds calls for a significantly high initial investment and is not feasible for small batch production.

These devices would require four surgical incisions to be made in the graft structure for the claps and wedges to pass through. The surgeon would also have to precisely align these features with the incisions inside the eye, whichfurther complicates the surgical procedure. The design in Figure 51b would need forceps that can generate sufficient force to push the wedge into the groove. It would be challenging to generate this force with the delicate tips of 23 gage forceps used in this procedure.

Mechanical Interlocking

The design in Figure 51e offers an alternate approach to securing the tissue graft without the requirement of high normal forces. In this design, the force comes from the tissue adhering to the rough surface of the structure. Hence, the device can be thin and compliant and still perform satisfactorily even if it does not apply a normal force on the graft tissue. Insertion of such a device can be achieved by deforming it so that it fits into the cannula. Unlike these lenses however the proposed device would be subjected to higher strains when inserting through a 2 mm cannula and therefore may not regain its original shape. Hence, the device would have to be made of a material that can regain its shape after severe deformation. This is one of the unique properties of shape memory alloys. Furthermore, nickel titanium alloy (nitinol) is a shape memory alloy that is approved for use in the manufacture of implants such as coronary stents. Shape memory structures can be taught to remember a particular shape. They can then be subjected to 6-8% strain but will regain the trained shape if heated above the austenite transformation temperature A_s. If the design in Figure 51d is made out of nitinol, it would fulfill all the

requirements stated earlier. This design is chosen as the principal solution for the tissue translocation device.

Embodiment

In this section the selected principal solution in Section 0.0.0 is developed in detail. Two embodiments of this device are presented. Various auxiliary devices to be used with this device are also presented.

Embodiment 1: Helical Coil

In this structure, the selected principal solution is very similar to the nitinol ring design [14] except that the two rings have been connected together to ensure that they are always concentric with each other. The helical configuration eliminates the need to align them inside the eye and avoids damage that would occur to the delicate RPE membrane during the surgical process. Hence, one embodiment of the principal solution consists of the two rings joined together by a tab as illustrated in Figure 52. This embodiment consists of a shape memory wire of circular or rectangular cross-section. The geometric constraints limit the diameter of the wire to about 100μm. The wire is trained to memorize a shape in its final position as shown in Figure 52. It is then straightened for insertion into the eye through the cannula. Part of the wire is heated above the austenite transformation temperature to form the bottom ring, which is inserted under the tissue graft. The remainder of the wire is heated to form the tab and top ring. The rings are then heated electrically to cause them to stick to the tissue. The tissue graft can then be cut and translocated.

The foregoing device was fabricated using 100 μm nitinol wire (Flexinol, Dynalloy Inc.) and tested ex-vivo on cadaver pig eyes in air as illustrated in Figure 53. It can be seen that the device successfully grasps and supports the tissue in spite of the small gage wire used. It effectively demonstrates the proof of concept. However, Figure

53b indicates that the tissue is not fully attached to the device along the periphery. This is primarily because of the small surface area of the wire that produces a low bond force, which could severely limit the success of the procedure. Further testing indicated that the forces involved in cutting the graft from the surrounding tissue was sufficient to break the bond between the tissue and the ring. Furthermore, this design suffers from the deficiency that the ends of the wire have a tendency to pierce the surrounding tissue and can lead to tissue damage.

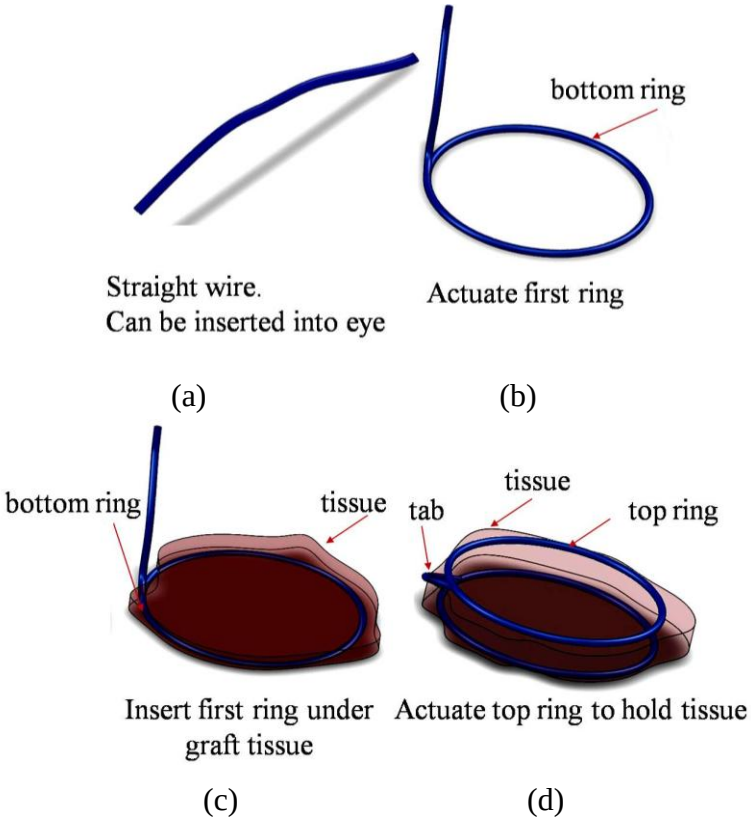

Figure 52: Embodiment 1: Shape memory alloy wire based design. (a) Uncoiled form for insertion (b) Bottom ring activated (c) Insertion under tissue (d) Top ring activated

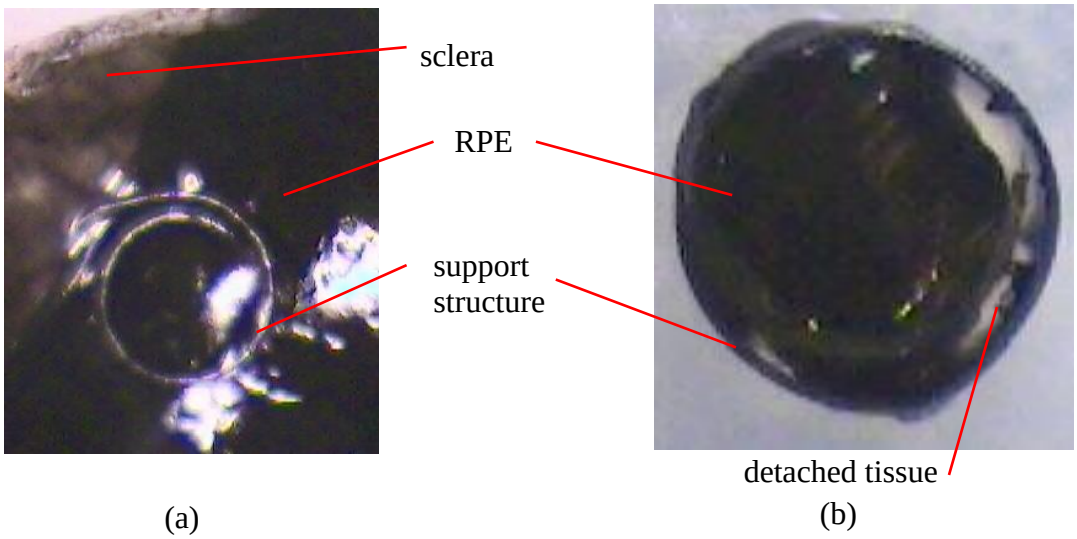

Figure 53: Ex-vivo tests of ring design in pig model (a) before extraction of graft (b) after extraction of graft

Embodiment 2: Foil Based Structure

The second embodiment of the principal solution is shown in Figure 54. This design improves on the ring design in that it has a much larger surface area since it is made from foil. Moreover, the annular surface can be textured to provide the tissue with features to shrink onto and create a stronger bond. The most basic form of texturing in the form of annular holes is illustrated in Figure 54. However, more complex surface features such as microscopic hooks or teeth may also be used.

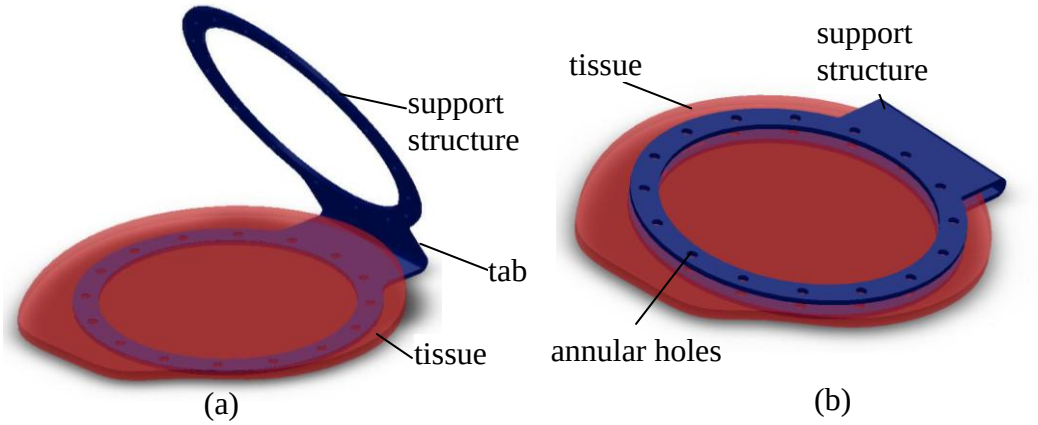

Figure 54: Embodiment 2: Shape memory foil based structure (a) open configuration (b) closed configuration

The structure is designed with a tab to increase the ease of device manipulation. If no gap is left between the rings, the tissue tends to wedge the structure open and prevents proper grasping as illustrated in Figure 55a. Hence, a gap of about 150 µm is intentionally created between the two rings to accommodate the tissue (Figure 55b).

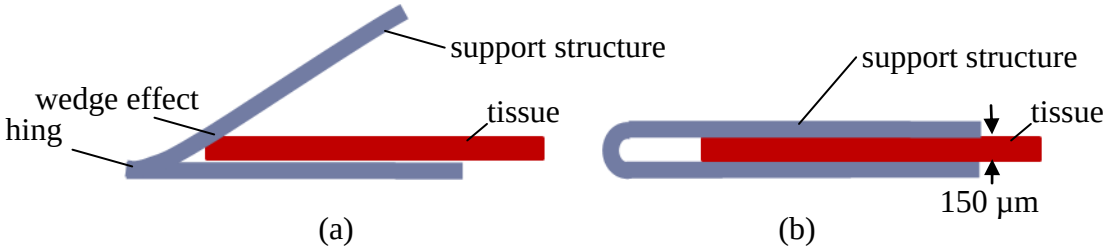

Figure 55: Foil hinge (a) Tab bent with zero radius (b) Tab bent with 150 µm bend diameter

Insertion of the foil through the cannula is achieved by rolling it in to a scroll of about 1.6 mm in diameter and then inserting it into the cannula or through a 2 mm incision in the eye. This process induces plastic strain in the material, which is recovered by the shape memory effect. Commercially available foils typically have A_s between 10°C and 90°C. Shape memory coronary stents typically have A_s at or slightly below body temperature to cause them to retain their trained shape once inserted into the body.

The tissue translocation device needs to remain open inside the eye during insertion under the tissue graft to be harvested (Figure 54a). The device is made with a transition temperature of 50 °C, which is above body temperature. This implies that the device would need some form of heat input to cause it to regain its trained shape.

Auxiliary Device: Heat source

Commonly used heat sources in ophthalmic surgery are surgical lasers (eg. Iridex Diolite) and bi-polar electric cauteries (eg. Synergetics Bi-polar Cautery Probes). The advantage of these two devices is that they require only a single port for insertion into the eye. The challenge with using lasers in the eye is that the beam has a comparatively large size, which makes it difficult to localize the application of heat. This problem is complicated further by beam divergence. Furthermore, the laser power required for proper heating of the foil structure was found to be almost 1W, a power level that is damaging to the eye.

Electrical resistance heating is another alternative to supply heat inside the eye. Bipolar cautery pencils are commonly used to control bleeding inside the eye (Figure 56a). Typically, a voltage of 30 to 50 V (sinusoidal, peak to peak) at about 360 kHz is applied between the two electrodes at the tip of the cautery to cause localized heating. However, as illustrated in Figure 56a, the area that is heated is extremely small. Also, the length of the electrical path is short leading to a very small resistance and hence, a small amount of heat is generated. Furthermore, both electrodes need to touch the foil structure to cause resistive heating. This requires the tip to be angled as shown in Figure 56a, which is cumbersome.

Limitations of bipolar cauteries suggest the need for two separate electrodes to increase the length of the electrical path and hence higher heat generation. This was achieved by modifying two 23 gage forceps (Alcon/Grieshaber) that are energized electrically (Figure 56b). A notable feature of this design is that it allows the disposable

tip to be easily replaced even after the modification. The forceps are supplied with 3 V DC and the typical current used in surgery to activate the support structure is about 2 A corresponding to 6 W.

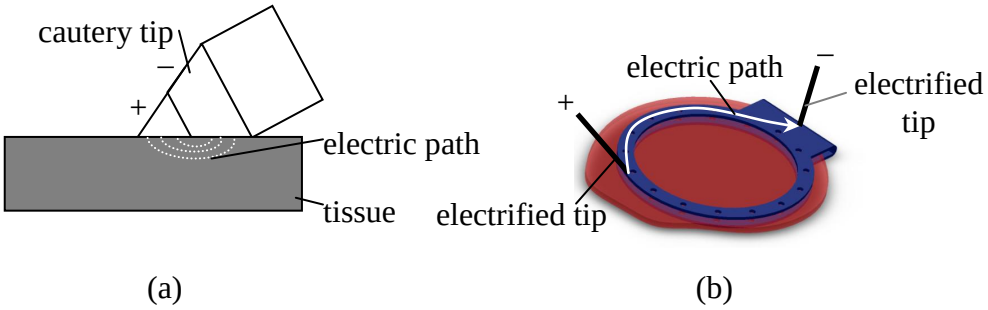

Figure 56: Electrical heat sources in ophthalmic surgery (a) bipolar pencil cautery (b) Monopolar electrified probes

Saline solution is used for infusion during the surgical procedure. This provides the current an alternate, low resistance path and causes the current to bypass the translocation device. Perflourooctane, which is an infusion liquid with a higher specific gravity than saline, and may be injected into the eye to create an insulating layer around the end of the tip in contact with the foil (Figure 57). Furthermore, the tips of the forceps are insulated, except at the two ends. The end of the tip that is connected with the electrical leads to the power supply remains outside the eye and out of the saline. Thus, current flow is focused through the foil to heat it instead of flowing through the saline solution. Based on the preceding discussion, the design shown in Figure 54 is the selected embodiment of the tissue translocation device.

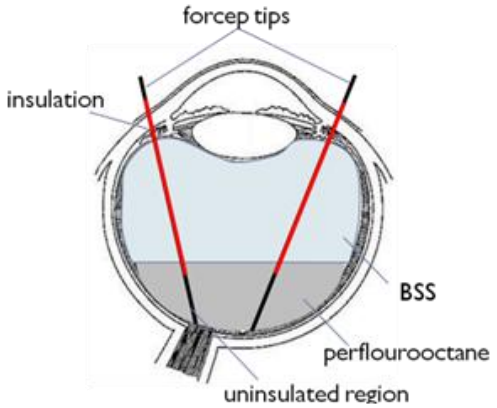

Figure 57: Modifications to prevent flow of current through saline

Application of Burr Formation and Deburring Knowledge to Device

The tissue support structure was manufactured by micromilling as shown in Figure 58. Nitinol foil (Johnson Matthey Medical Components), 25 µm in thickness was glued to a PMMA backing and micromilled on a laboratory-built micromilling machine (Figure 58). The profile was cut using a 500 µm diameter end mill (PMT TR-2-0200-S) rotated at 60,000 rpm and fed at 100 mm/minute. The holes in the annulus were milled using a 200 µm diameter (PMT TR-2-0080-S) end mill at the same spindle speed but with a 10 mm/minute axial feed rate. The glue was then dissolved to release the part from the backing. It was then deburred and polished using emery paper. The flat foil structure was then folded in half while heating it to about 480°C to avoid failure during bending due to work hardening. It was then trained for 5 minutes at the same temperature in the closed configuration to obtain the final part shown in Figure 59. The foil in its rolled configuration is also shown. The roll has a diameter of about 1.6 mm which would easily fit through a 2 mm incision.

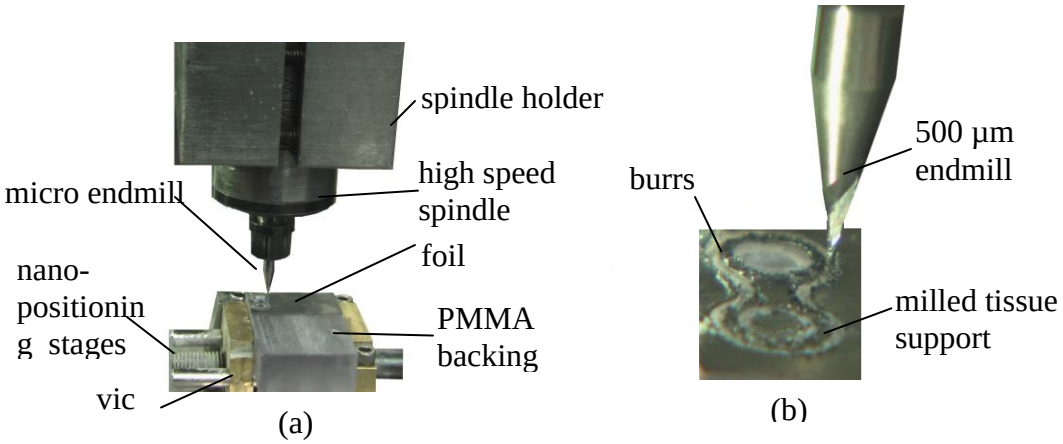

Figure 58: Micromilling of tissue support structure

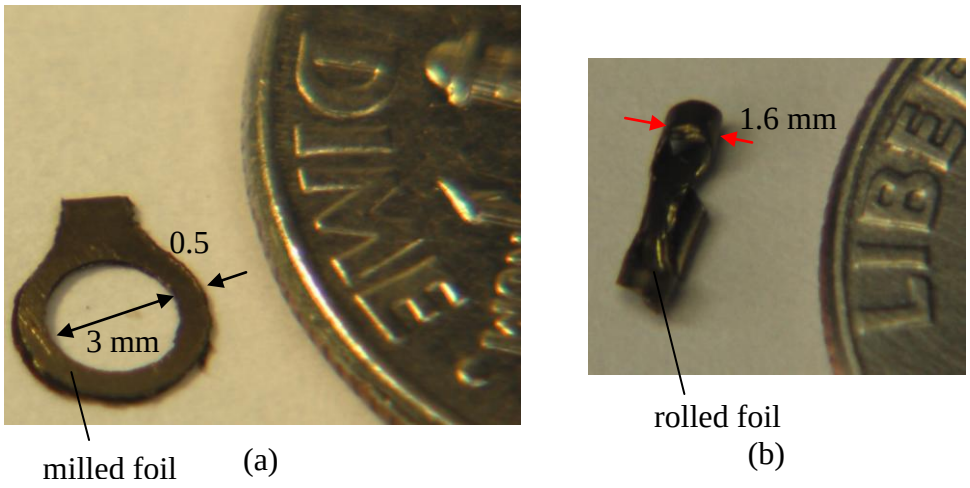

Figure 59: Micromilled foil support structures without annular holes (a)unrolled and closed (b) rolled

A notable feature of the micromilling process is the production of burrs as shown in Figure 61a. These burrs serve as microscopic hooks to grasp the tissue graft and are retained on the graft side of the foil. However, the presence of burrs on the side that contacts the surrounding tissue could lead to damage of the graft and surrounding tissue. Hence, it is important to limit the size of the burrs on the device. Knowledge generated in Chapter 4 is applied to obtain two distinct burr size ranges (Figure 60). The devices are milled on a PMMA backing with cyanoacrylate adhesive. Large burrs are produced by

selecting the tool path such that the device edges are downmilled with a feed of 1 μm/tooth. Significantly smaller burrs are produced by upmilling with a feed of 10 μm/tooth. Mean burr widths measured on these devices are compared with those predicted by the model and found to be in good agreement (Table 15). Variation in size of the larger burrs is much higher than that of the smaller burrs. The smaller burrs are stiffer due to their shorter length and have a higher tendency to stay normal to the foil surface unlike the larger but slender burrs. This would make the smaller burrs more capable of penetrating the tissue and anchoring it. Furthermore, the larger burrs cover the annular holes and would obstruct vascularization.

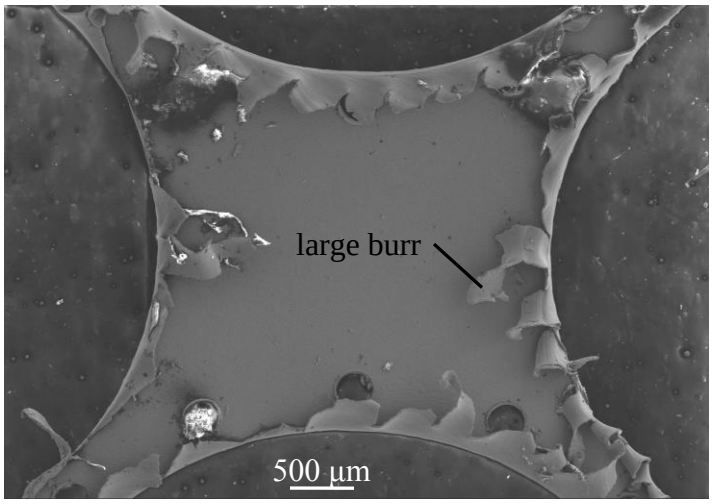

(a)

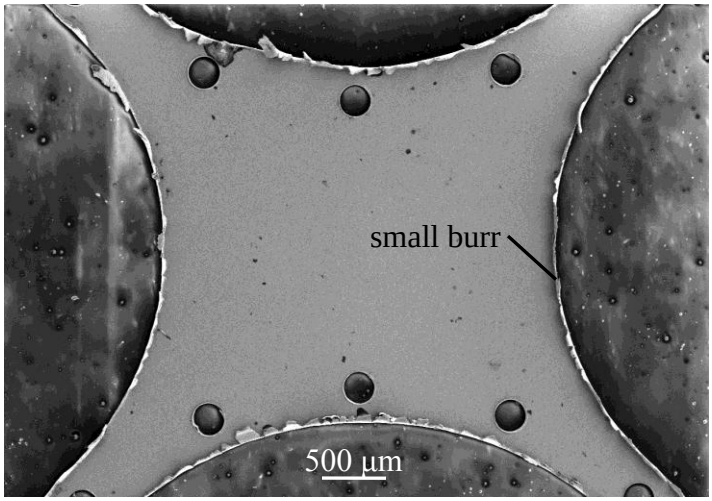

(b)

Figure 60: Different size burrs produced on device by selecting appropriate feed and milling side (a) Large burrs produced using 1 µm/tooth and downmilling (b) Small burrs produced using 7.5 µm/tooth and upmilling

Table 15: Comparison between predicted burr widths and measured burr widths on device

Feed (µm/tooth)			1	7.5
Burr width (µm)	**Model**		32	223
	Experimental	**Mean**	41	204
		Std. dev.	10	86

The devices in Figure 60 were deburred based on the predictions from Chapter 5 with two passes after Phase I at 15000 rpm with 1 mm nominal brush penetration and complete deburring was achieved. The annular holes also remain undamaged.

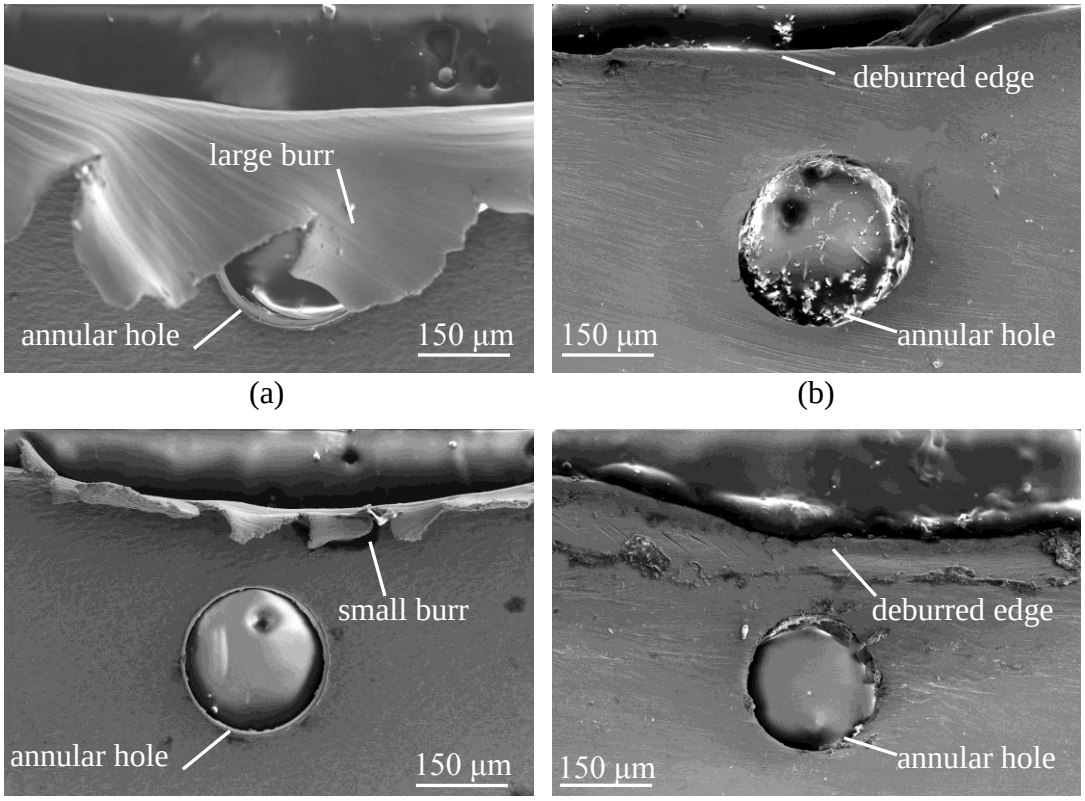

Figure 61: SEM images of tissue translocation device (a) Device with large burrs (b) Device with large burrs after deburring (c) Device with small burrs (d) Device with small burrs after deburring

Animal Studies

The support structures were tested along with the electrical actuation system ex-vivo with cadaver pig eyes and in-vivo with live pigs. Results of an ex-vivo test are shown in Figure 62. It can be seen that the structure can be used to translocate tissue. No significant damage due to electrical heating can be visually observed in the tissue patch.

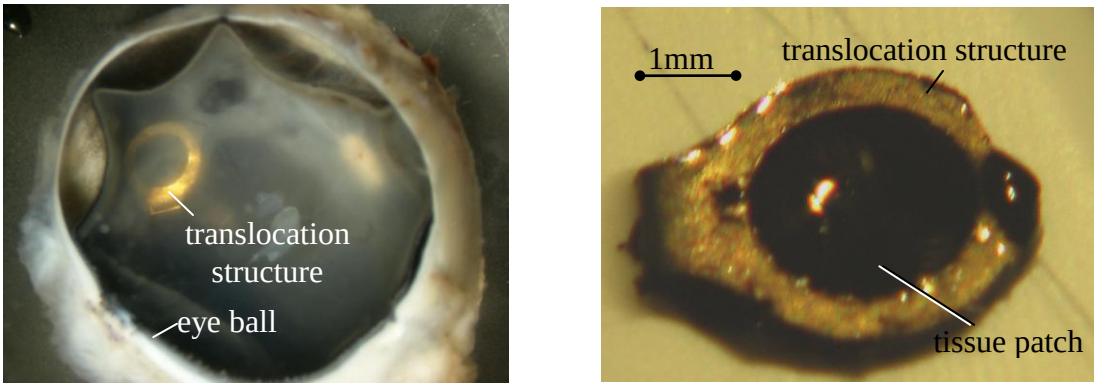

(a) (b)

Figure 62: Ex-vivo tests of foil based structure (a) Device implanted in pig eyeball (b) Device with harvested tissue graft

The in-vivo tests are summarized in Table 16. The wire-based device was actuated with laser heating in six pigs. Although the tissue adhered to the wire, the forces involved in translocating the graft are high enough to break the adhesive bond. The 50 µm foil based devices were difficult to manipulate using the delicate 23 gage forceps used for retinal surgery. Therefore, 25 µm foil based devices were tested in 15 pigs. In five pigs, the device was actuated with the laser (Iridex Diolite). Laser power of about 0.8 W was needed for shape recovery of the foil and adhesion with tissue. However, the tissue graft was severely damaged due to the high power used. The patches were inserted under the retina in four animals and survived for one to seven weeks. The 25 µm foil devices were then tested in ten pigs with electrical actuation. Perflourooctane was used to insulate the tips from the Balanced Salt Solution (BSS) infusion fluid. Successful translocation was achieved in three pigs. Among the devices used, some had burrs on the order of 200 µm, some about 40 µm and some were completely deburred. However, the tissue, whose thickness is estimated to be about 150 µm would be pierced and damaged if the burrs are larger than about 75 µm. Furthermore, burrs larger than this size would obstruct the annular holes as well as cause the tissue to contact the device only at the high points of the burrs, reducing the area for the tissues to thermally adhere to the device. The

effect of the presence of these burrs on tissue healing requires detailed in-vivo surgeries and is left to future work. However, it may be noted that barbed sutures are routinely used in surgery to close up wounds [121].

Bleeding during surgery poses a severe limitation. The presence of multiple instruments in the eye and the large incision used to insert the rolled foil leads to a drop in the pressure inside the eye due to leakage of infusion. This makes it difficult to tamponad the bleeding once it starts. This limitation of the procedure can be overcome by using a clear corneal incision since these incisions are self-sealing.

In some cases because of the bleeding, the entry of the foil under the tissue patch to be harvested was obstructed by a clot. This caused the foil to fold over itself. A long pick would need to be used to remove any obstructions and can also be used to ensure a large enough pocket under the RPE for the structure to be inserted without the burrs snagging on the tissue. Another challenge with this procedure is that the perfluorooctane becomes cloudy as the electric current heats the foil causing a reduction in visibility. This could be partly due to localized arcing between the tips of the forceps and the foil leading to localized degradation of the perfluorooctane. Consequently, the perfluorooctane has to be removed after activation of the foil.

Table 16: Summary of in-vivo tests of device with primary results

Device	No. of pigs	Survival	Results
100 µm wire	6	0	Insufficient adhesion to tissue
50 µm foil	2	1	Too thick to be manipulated with 23 gage forceps
25 µm foil, laser actuation	5	4	High Laser power required for actuation damages tissue
25 µm foil, electric actuation	10	3	Successful translocation if bleeding is controled

Conclusions

This chapter presented the systematic design of a device to translocate tissue inside the eye for surgical correction of AMD. The following conclusions are drawn:

- Currently used tissue translocation techniques were analyzed and found to have significant limitations to perform translocation in the eye.
- A novel device was designed and manufactured out of thin nitinol foil. The device could be inserted through a 2 mm incision in the eye by rolling it. The rolled coil could be successfully unrolled in the eye using shape memory effect caused by electric heating.
- The adhesion of the tissue to the device is achieved by electrically heating it beyond the shape transformation temperature of the structure.
- The adhesion of the tissue to the foil structure is further improved by the presence of burrs along the edge of the device. These burrs are produced during the micromilling process and act as microscopic hooks to anchor the tissue to the foil structure.
- The predictions for burr size from Chapter 4 and deburring passes from Chapter 5 can be successfully applied to the device to produce either large (~200 μm) burrs or small (~ 40 μm) burrs as well as to fully deburr them.
- The device was shown to successfully grasp and translocate a patch of tissue in both ex-vivo and in-vivo tests carried out on pig eyes.

The next chapter presents an analysis of the structural and thermal characteristics of this device.

CHAPTER 7

ANALYSIS OF TISSUE SUPPORT DEVICE

In this chapter a bilinear kinematic material model can be used to simulate the clamping force generated by the device on the tissue due to shape memory effect. This approach proved adequate because of the noncyclic loading conditions for the device. This presents an advantage over the other models in that it does not require the use of special algorithms. The model was also used to explore the limits on the deformation of the device imposed by loss of shape memory. Prior thermal models involving ocular tissue have focused on simple geometries such as electrodes and do not provide insight in to the temperature profiles of a planar structure with varying cross sections. Hence, an electro-thermal analysis was performed to simulate the thermal gradients in the device as well as the thermally affected region of the tissue. These finite element analyses were also verified using closed form reduced order models.

Clamping Force Analysis

Motivation

Shape memory effect is used in the tissue translocation device to close on to the tissue patch that needs to be moved as illustrated in the Figure 54. The objective of this analysis was to simulate the amount of clamping force the structure would exert on the tissue. The developed model was also used to evaluate the effect of changing the thickness of the structure on the force exerted by the structure on the tissue.

Geometry

The geometry used to model the structure is shown in Figure 63. It consists of a thin planar structure folded over similar to a paperclip. At the open end, the gap between

the foil is assumed to be 2 µm. This ensures that the edges are close to each other without being merged completely by the finite element software. Symmetry is used in modeling the structure.

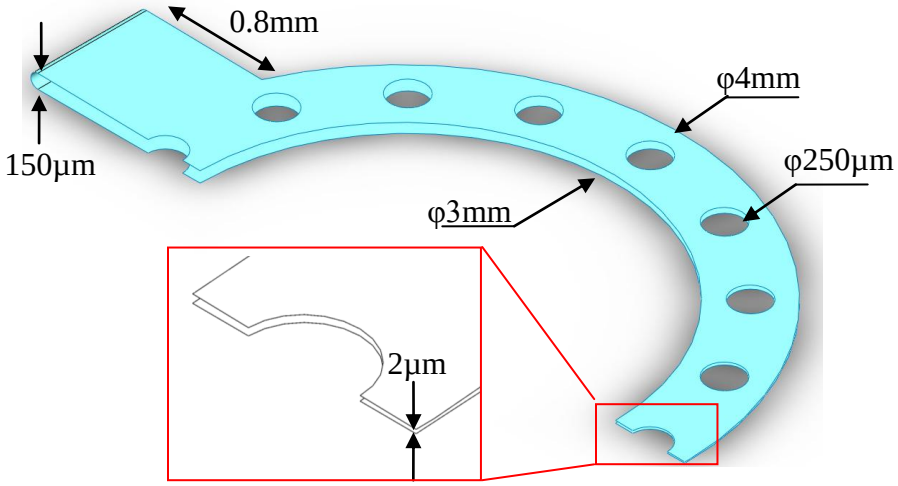

Figure 63: Geometry used for structural analysis

Material Models

The material model used in this model is based on the work done by Terriault et al. [77]. The aim of this study is to model the pressure applied by the foil on the tissue when its temperature is raised beyond A_f. At this high temperature, in the stress free state, the material is fully austenite. During operation of the device, the structure is initially deformed to open it at a temperature below A_f. Hence, it is consists entirely of the low temperature phase, martensite and will follow the purely elastic-plastic behavior of martensite. If the induced strains are below 8%, all the mechanism of strain is exclusively twinning. Consider the case that it is constrained to remain open in this state and the temperature is increased to above A_f by resistance heating. The material attempts to transform to the high temperature phase namely, austenite and in the process attempts to recover the strain. However, since it is constrained, it cannot achieve this transformation and the material remains in the stress-induced martensite phase. If the structure is

released from the constraint, it follows the martensite elastic and subsequently the inverse transformation curve in Figure 4. This process of recovery continues until it touches the tissue at which point it is restricted from further recovery. If the strain in this case is above ε_{af} (Figure 4), then the material is partly austenite and partly martensite. If the strain is below ε_{af}, the material is completely austenitic. In this study, our intention is to model the force applied by the foil structure at high temperature on the tissue as it regains its trained shape. Hence, the direct transformation curve can be neglected and the structure can be modeled as a bilinear kinematic hardening material. Material properties are shown in Figure 64 and are obtained from [77] at 50°C.

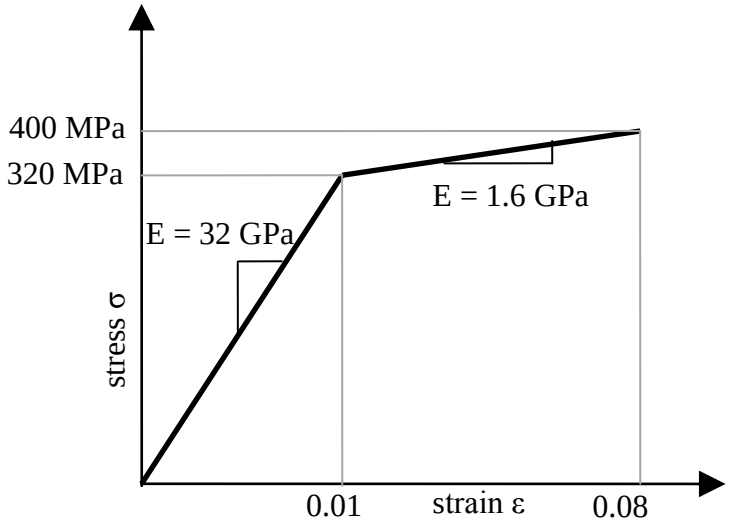

Figure 64: Stress-strain curve used in FE model

Boundary Conditions

As discussed in the previous section, the complete closure of the foil is prevented by the presence of tissue between the two foils. This results in some residual strain in the foil, which in turn induces a corresponding stress in the foil based on the stress-strain curve in Figure 64. This internally generated residual stress due to the shape memory effect or elasticity causes the foil to apply a corresponding pressure on the tissue. The tissue in turn applies a reaction pressure on the foil. Hence, the pressure on the tissue has

a one-to-one correspondence to a given displacement of the foil. This correspondence is governed by the inverse transformation stress-strain curve of nitinol. Hence, the device is deformed from the trained shape (closed) by a pressure on the foil to open it, the material model traces the stress-strain curve (Figure 64) from the strain free, trained state. The deformed shape of the structure when it contacts the tissue is known. If the pressure is now varied, a point is reached when this known deformation (strain) is induced in the foil. The pressure corresponding to this known strain is also the pressure applied by the foil on the tissue in equilibrium and is the quantity of interest in this analysis. Hence, as shown in Figure 65, the actual process follows the curve from a point of higher strain to the known strain while the finite element model starts from a strain free state and follows the curve to the known strain.

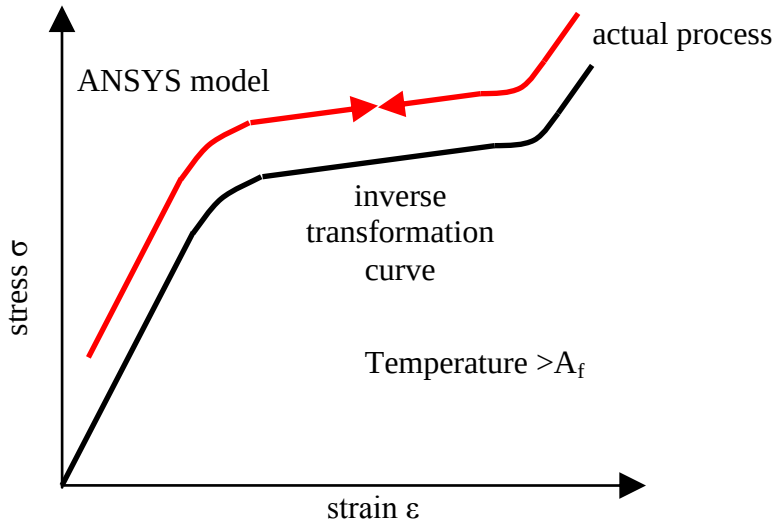

Figure 65: Actual process of deformation verses the ANSYS model

Based on this approach, the model is subjected to the loads shown in Figure 66. The bottom part of the foil is held fixed. Symmetry is used in the model and so displacement along the z-axis for the edges shown is constrained. Pressure *P* is applied to the top face of the foil along the positive y-axis. In the actual foil, there will be a gradient in the pressure with a higher pressure towards the hinge and a lower pressure towards the open end because of higher strain near the fixed end of the foil, similar to the strain

distribution in a cantilever beam. However, this gradient is assumed to have a negligible effect on the analysis since the difference in strain is fairly small. Furthermore, the quantity of interest is the average pressure on the tissue and not the variation.

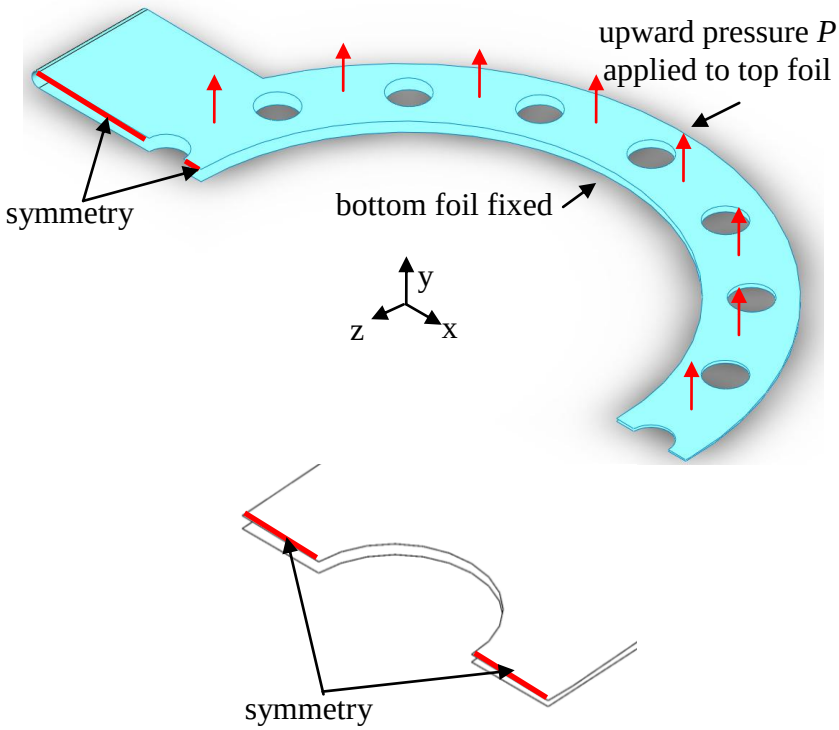

Figure 66: Boundary conditions for clamping pressure simulation

The analysis was carried out using ANSYS® Multiphysics V13. The model is a thin structure with out-of-plane loading and displacements. Hence, it was meshed with linear shell elements (SHELL181). Convergence to within 6% for maximum von-Mises stress was obtained as shown in Figure 67.

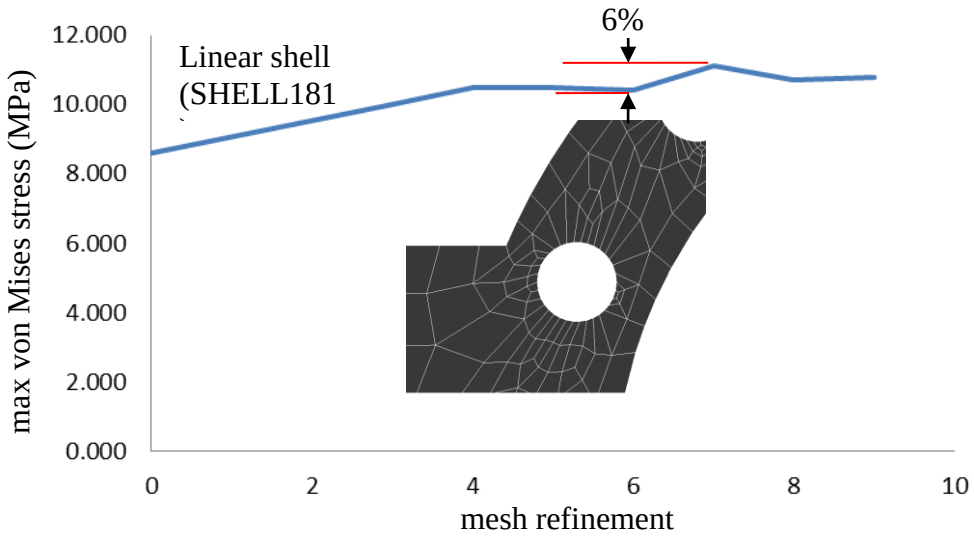

Figure 67: Convergence with linear shell elements

Results and Discussion

Simulations were run by varying pressure *P* so that the displacement of the open end reached the known displacement of 150 µm. It was found that this displacement was reached at a pressure of 77.12 Pa as shown in Figure 68. This corresponds to a net force of 220 µN on the tissue. This force is extremely small and insufficient for clamping tissue.

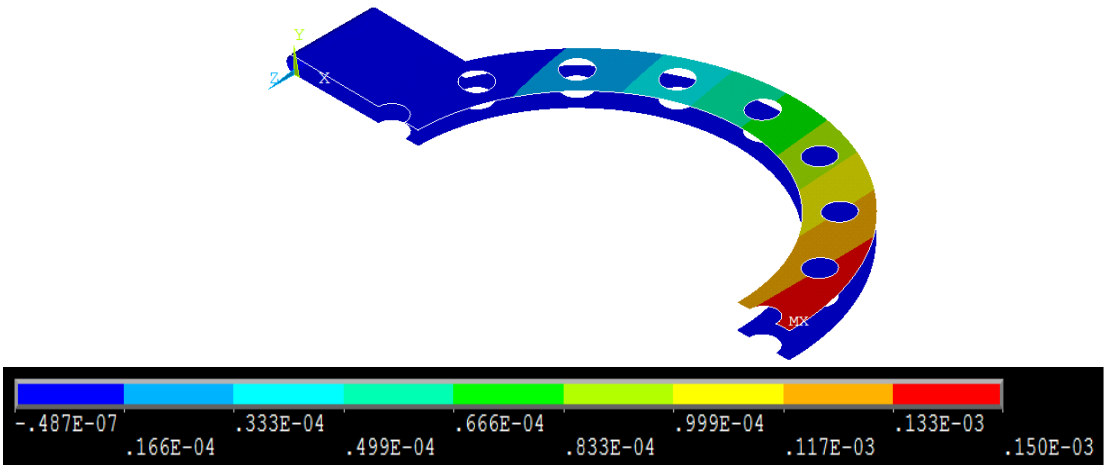

Figure 68: Displacement of foil on application of a pressure of 77.12 Pa

The model was used to evaluate the effect of increasing the foil thickness on the clamping force. As can be seen from Figure 69, clamping force even as low as 200 mN (20 g) can be generated only if the foil thickness is greater than 300 µm. This however, is much larger than is allowed by the space between the tissues and could increase chances of autoimmune rejection. Hence, it can be concluded that shape memory effect cannot provide the necessary clamping force to hold the tissue. This limitation can be overcome by employing thermal adhesion to hold the tissue.

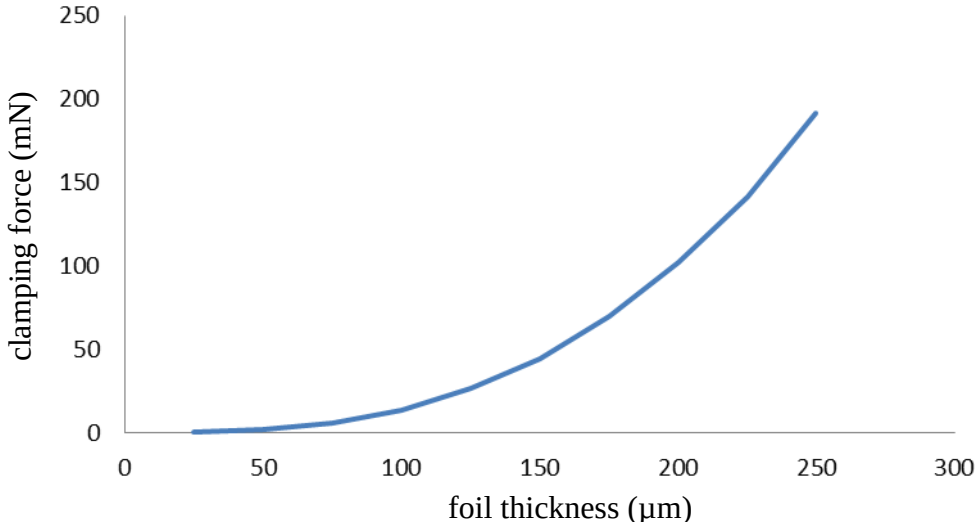

Figure 69: Variation of net clamping force with foil thickness

Closed Form Analysis and Verification

Structurally the foil is similar to spring made of half a turn of a rectangular cross section wire (n = 0.5). Hence, the results of the FEA model were verified by analytical equations for the axial stiffness λ_x of such a spring using Eqs. 39 to 41 [122]. The symbols used for the dimensions of the spring are illustrated in Figure 70. Shear modulus G can be calculated using Eq. 40 as a function of elastic modulus E and Poisson's ratio v. Based on this stiffness, the force required for a 150 µm deflection is calculated and compared with the values obtained from the FE analysis. It can be seen that the values

agree to within 30%. It is noted that the analytical equations do not capture the effect of the annular holes and hence overestimates the required force.

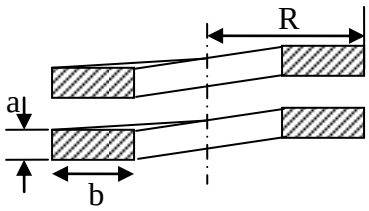

Figure 70: Rectangular section helical spring

$$\lambda_x = \frac{GC}{2\pi R^3 n} \quad (39)$$

$$G = \frac{E}{2 \cdot (1+\nu)} \quad (40)$$

$$C = a^3 \left[\frac{b}{3} - 0.209a\left(tanh\left(\frac{\pi a}{2b}\right) + 0.004\right)\right] \quad (41)$$

Table 17: Comparison of predicted force for 150 µm deflection from FEA and analytical model

Load (µN)	
spring model	**FEA**
285	220

Bending Analysis

Motivation

During the surgery the support structure is rolled up into a spiral and inserted through an incision. During this process the foil undergoes large bending strains. The shape memory effect is completely reversible to a strain of 8 %. However, the bending strains can reach higher values and cause permanent plastic deformation of the structure. It is the role of this investigation to analyze the stresses and strains induced in the device when it is rolled in a spiral. The model is then used to study the effect of changing the foil thickness and hole diameter on these strains.

Boundary Conditions

The boundary conditions applied to the foil as shown in Figure 71. The top edge is first given a ramped rotation of 3.15 radians (180 degrees) so that the foil is folded over in half (Load Step 1). The edge is then moved vertically downwards so that the bend diameter *d* becomes smaller (Load Step 2). The base is clamped and symmetry is applied to the edges shown.

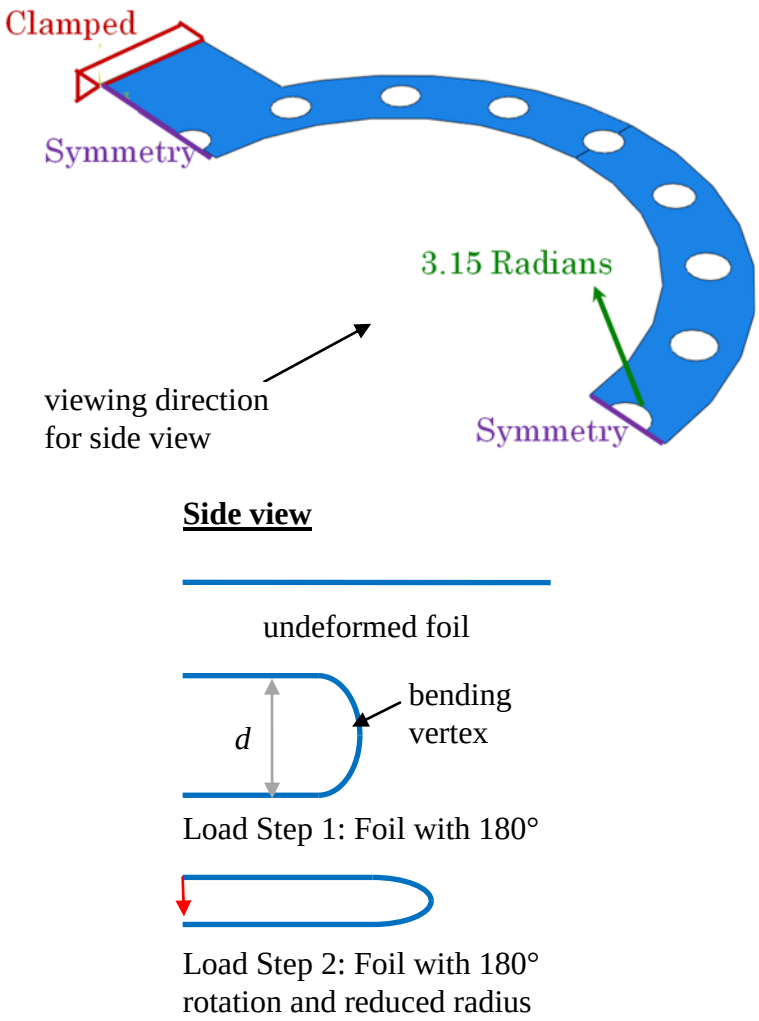

Figure 71: Boundary conditions for bending analysis

Meshing

The bending analysis was carried out in ABAQUS. A 4-node general-purpose shell element with reduced integration, hourglass control and finite membrane strains was used to discretize the geometry. Convergence with maximum stress is achieved to within 2% at the element size of 0.05 µm (Figure 72). The mesh that was finally used is shown in Figure 72.

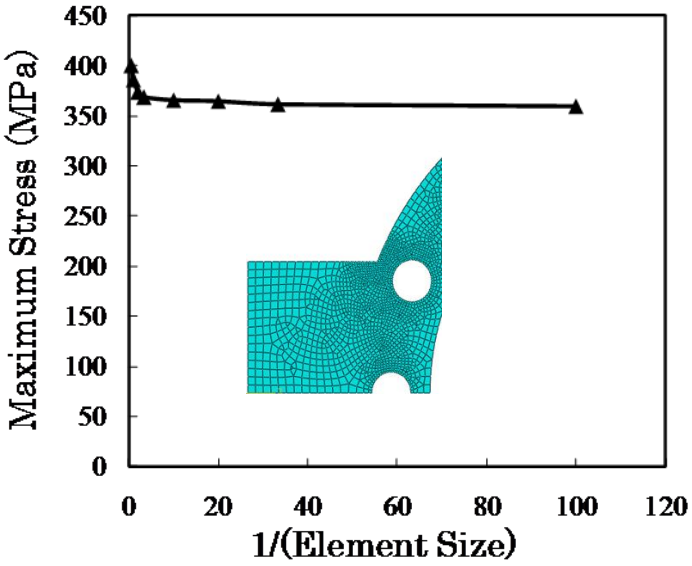

Figure 72: Mesh convergence for bending

Results and Discussion

When the foil is subjected to bending, stress concentrations develop around the holes that are close to the bending vertex. Strains beyond 8% cannot be recovered by shape memory effect. Hence, the bend diameter *d* which induces a maximum strain of 8% is considered to be the minimum radius of the spiral the device can be rolled in to. Figure 73 shows this strain for a foil of 25 µm thickness and hole diameter of 250 µm is reached at a bend diameter is 1.55 mm. The diameter of the incision through which the foil needs

to be inserted in to the eye is about 1.6 mm. Hence, these results imply that the foil can be inserted in to the eye without inducing plastic strains.

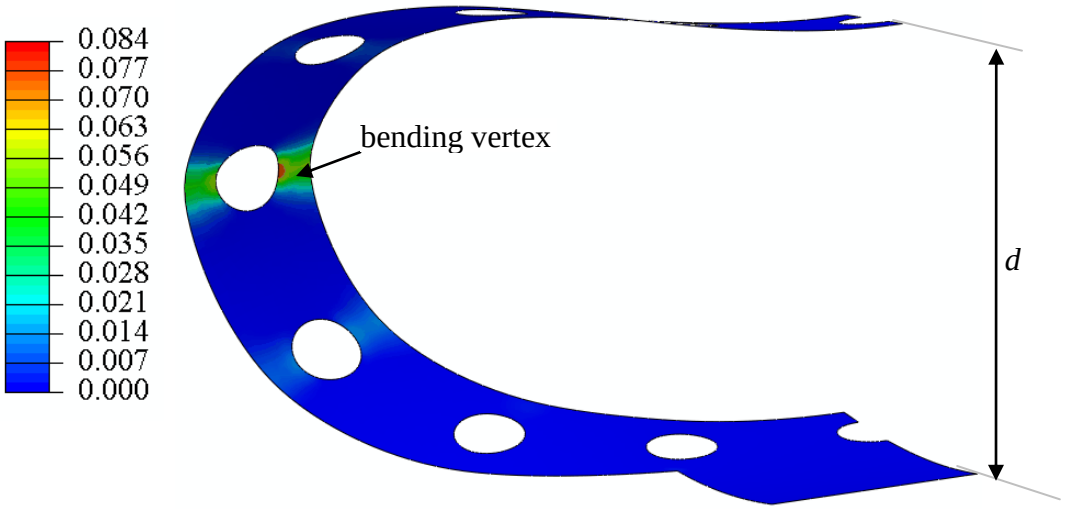

Figure 73: Equivalent strain contour plots for foil

As mentioned in Section 4 e, the clamping force can be increased by increasing the foil thickness. Hence, the effect of increasing foil thickness on the maximum possible bend angle. Figure 74 shows the strain and corresponding rotation for structures with increasing thickness from 25 µm and 200 µm. It can be seen that devices made of foils thicker than 25 µm cannot be folded over completely (180° rotation).

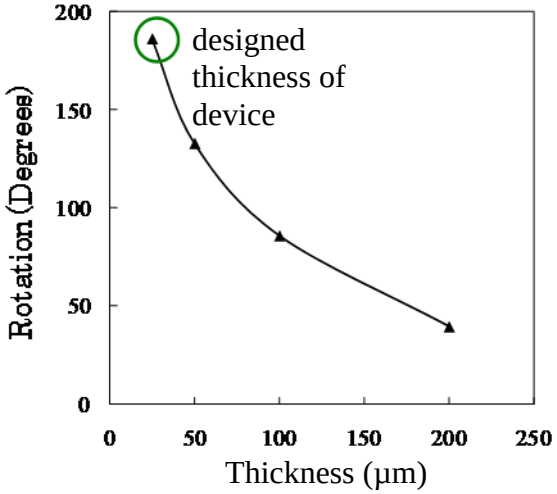

Figure 74: Rotation to failure as a function of thickness

Holes are milled in the annulus to provide texturing to the surface and improve adhesion with the tissue. However, they also weaken the structure. Hence, the effect of the hole diameter on the bend diameter *d* was analyzed for hole diameters from 200 µm to 350 µm. Figure 75 shows that the minimum bend diameter increases almost linearly with increase in hole diameter.

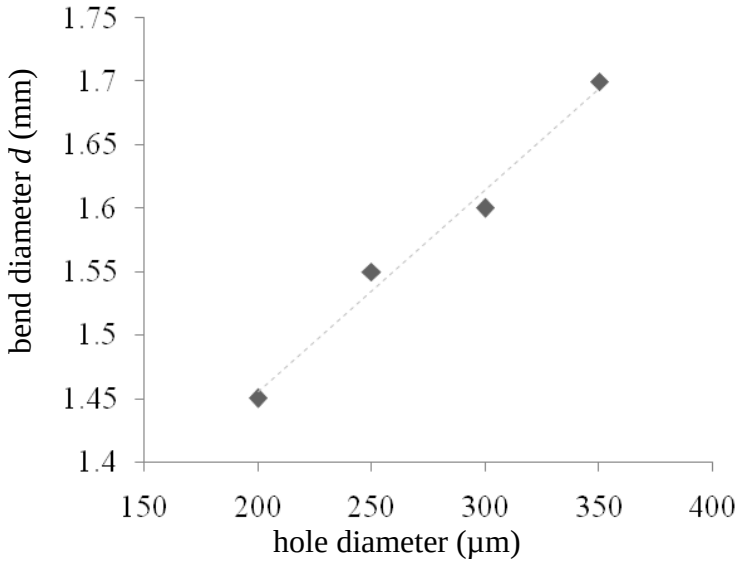

Figure 75: Variation of bend diameter as a function of hole diameter for a 25 µm thick foil

Closed Form Analysis and Verification

Results from the FEA analysis were verified using analytical equations for sheet bending. The theoretical strain in the outer and inner fibers of the foil e_i for a 180° bend is given by Eq. 42 where *r* is the bend radius and *T* is the thickness of the foil [123]. The strain value for a 25 µm foil with 250 µm diameter holes obtained from FEA is compared with the estimate from Eq. 42 in

Table 18 and found to be in good agreement.

$$e_i = \frac{1}{\frac{2r}{T} + 1} \quad \textbf{(42)}$$

Table 18: Verification of FEA results for bending

average strain (%)	
FEA	**analytical**
1.18	1.2

Electro-Thermal Analysis

Motivation

From the discussion in Sections 3 and 4, it can be concluded that the amount of force generated by shape memory effect is too small to clamp the tissue. However, the tissue can be held stretched if it is thermally adhered to the foil [84]. It has been shown that tissue will stick to an electrode if the temperature of the tissue reaches 70°C [124]. However, if temperatures reach about 100°C, dehydration causes the tissue to disintegrate and it would get detached from the foil. Hence, the voltage has to be controlled so that the overheating of the tissue is avoided. Furthermore, some heat is conducted in to the choroid. If the temperature in the choroid exceeds 70°C, it will stick to the foil and hinder the extraction of the tissue patch. The electrodes, foil and tissue are surrounded by a fluid environment (perflorooctane). Hence, some heat is lost to convection. The objective of the following analysis is to study the relationship between voltage applied to the foil and tissue temperature in a fluid environment.

Geometry

The geometry used for the model is shown in Figure 76. It consists of a patch of RPE sandwiched between the foil structure. The foil thickness is 25 µm, while the RPE tissue is 150 µm thick. Below this composite structure is the choroid which is 350 µm thick. The radius of the foil hinge is neglected in this analysis. As illustrated in Figure 56, the foil is actuated by touching it with two forceps, one at the hinge and the other diametrically opposite. The area of contact between the forcep and the foil was measured under a tool makers microscope and found to be approximately rectangular with dimensions 250 µm x 210 µm. Since symmetry is used in the model, the contact area is modeled as a patch with dimensions 250 µm x 105 µm.

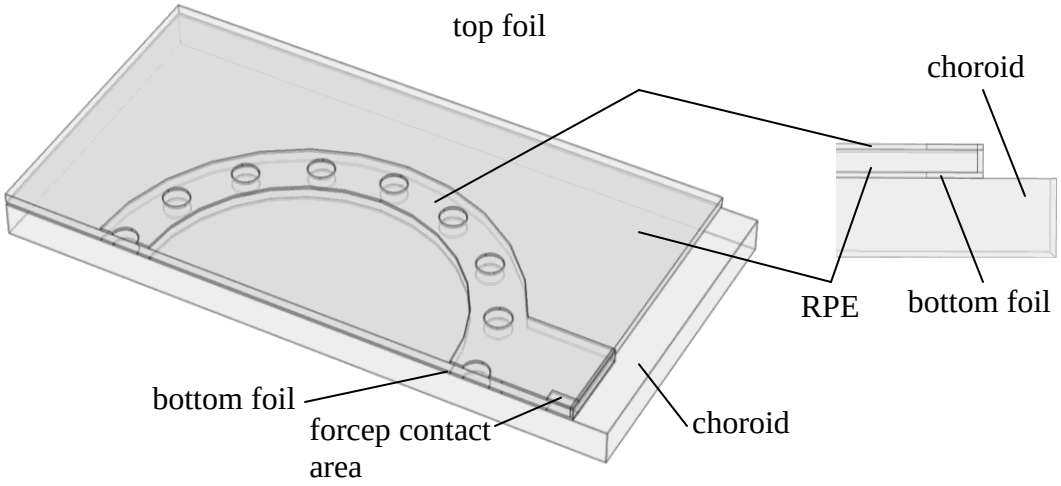

Figure 76: Geometry used for electro-thermal analysis

Materials

Electrical and thermal properties of the tissue and foil are summarized in Table 19. Most body tissues have about 80% water content. Consequently, thermal and electrical properties of various tissues in the body are similar to that of water. Hence, both the RPE and the choroid are assigned the same material properties. All properties are assumed to be constant with respect to temperature. Convection coefficient of fluid around the foil h_{pfo} is assumed to be 250 W/m^{2}K based on an estimate from [125].

Table 19: Thermal and electrical material properties for support structure and tissue

			Nitinol		**Retina**	
Property	Unit	Name	Value	Reference	Value	Reference
Electrical conductivity	S/m	k	10^6	[126]	0.1	[127]
Thermal conductivity	W/(mK)	K	18		0.454	[128]
Density	kg/m^3	ρ	6450		1062	[86]
Heat capacity at constant pressure	J/(kgK)	C_p	840		3680	[129]

Boundary Conditions

COMSOL® has a built-in bio-heat transfer analysis module. The governing equation is shown in Eq. 43, where ρ_b is the density of blood, C_b is the specific heat of blood, ω_b is the flow rate of blood [124]. The term $\rho_b C_b \omega_b (T_b - T)$ corresponds to heat extracted by blood flow (perfusion) through the tissue. Heat generated in the tissue due to metabolism (body heat) is captured by the term Q_{met}. External heat generation Q_{ext} in this study comes from electric resistance heating of the foil and tissue. On the left hand side of the equation, δ_{ts} is the heating time, ρ is the density of the tissue, C is the specific heat of the tissue, k is the conductivity of the tissue, T is the temperature of the tissue and t is time. Hence, heat is added to the tissue by resistance heating and metabolism while heat is extracted due to conduction to surrounding tissue and heat transfer to blood flow. The rate of temperature rise in the tissue is proportional to the net heat transfer through the tissue. Values used for perfusion constants are shown in Table 20.

$$\delta_{ts}\rho C\frac{\partial T}{\partial t} + \nabla \cdot (-k\nabla T) = \rho_b C_b \omega_b (T_b - T) + Q_{met} + Q_{ext} \quad \textbf{(43)}$$

Table 20: Values for perfusion

Quantity	Value	Units	Reference
$\boldsymbol{\rho_b}$	1000	kg/m^3	[6]
$\boldsymbol{C_b}$	4180	J/(kgK)	[6]
$\boldsymbol{\omega_b}$	0.2	s^{-1}	[11]

The boundary conditions for the electrical analysis are shown in Figure 77. The coupled electro-thermal analysis consists of a steady state electrical analysis followed by a transient thermal analysis. Voltage is applied to the area where the forceps touch the foil (Figure 77). The other end of the foil is set to ground voltage. All other surfaces are electrically insulated.

Boundary conditions for thermal analysis are shown in Figure 78. Heat generation by resistance heating calculated from the electrical analysis is applied to all the parts in the model. Heat extraction due to blood perfusion is specified in the RPE and choroid

tissue volumes. The bottom surface of the choroid is fixed to body temperature. Convection is specified on all top surfaces of the foil and RPE that are exposed to perflourooctane. Heat generated due to metabolism is assumed to be negligible in this analysis in comparison to the heat generated by resistance heating. The model is meshed using linear tetrahedral elements. Convergence on heat flux magnitude to within 5% was obtained with moderate mesh sizes as shown in Figure 79.

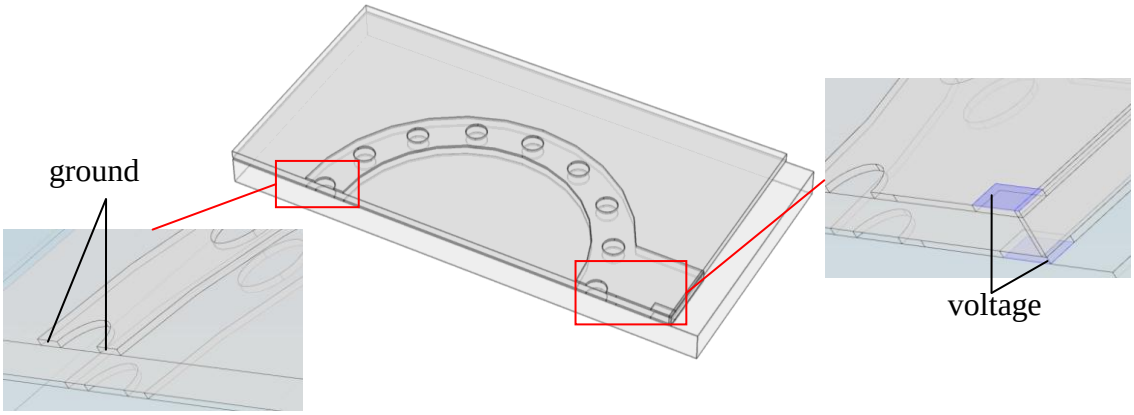

Figure 77: Boundary conditions for electrical analysis

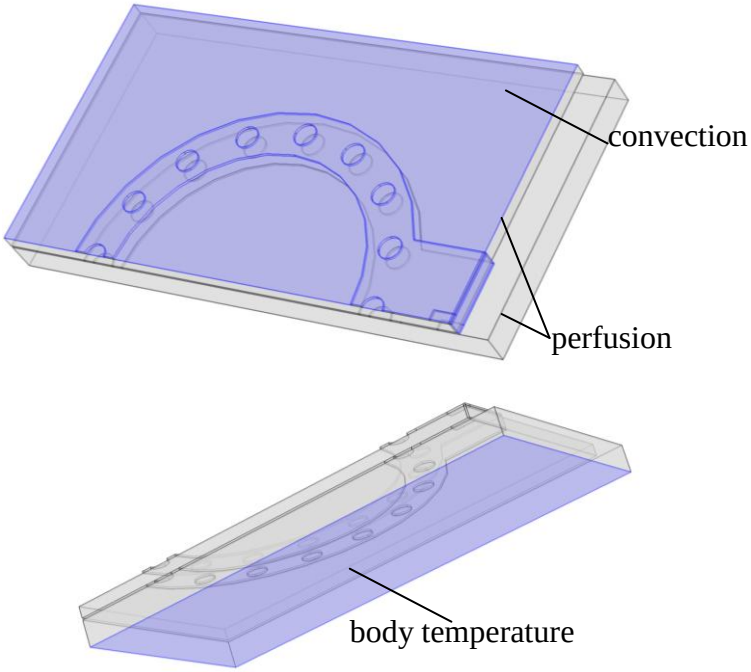

Figure 78: Boundary conditions for thermal analysis

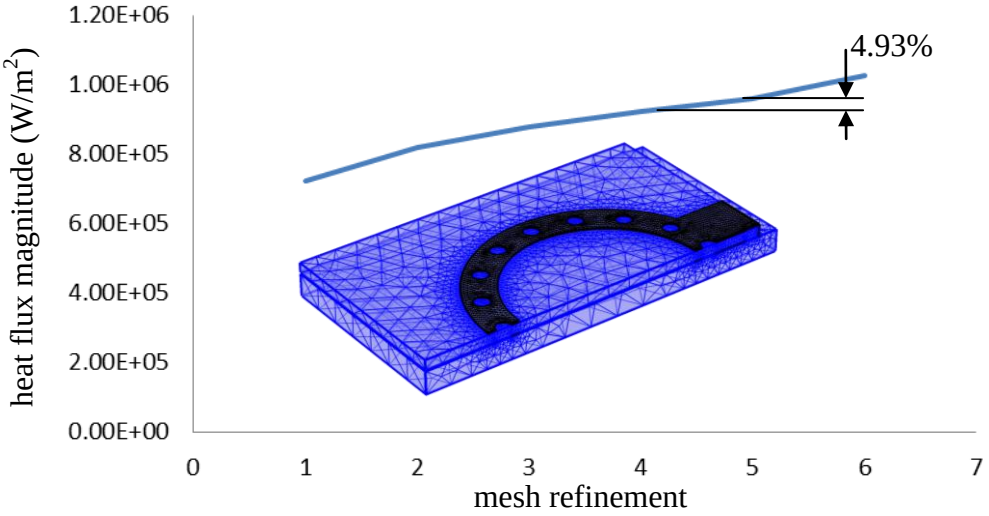

Figure 79: Convergence of electro-thermal analysis

Results and Validation

The voltage at which the average temperature in the foil reaches 70°C is found to be about 0.35 V. In practice, however, the required voltage is about 3 V. This discrepancy is mostly due to the resistance of the leads and electrified forceps R_e that have not been included in the FE model. The resistance R_e and the resistance of the top half of the foil R_f were measured using a digital multimeter and the results are tabulated in Table 21. In addition to the comparatively high resistance of the forcep and leads, additional power is required to overcome the contact resistance between the foil and the forceps and the resistance of moving parts in the forceps.

Table 21: Resistance of forceps and foil

Resistance Ω	
R_e	**R_f**
2.8	0.38

Maximum temperature in the model is in the foil close to the open side as seen in Figure 80. This is because current density is less at the tab and hence it heats to a lower extent. Furthermore, the tab has a larger area for heat convection and is also closer to the bottom foil which acts as a heat sink. Hence, heat loss from the foil is higher in this area.

As a result, temperature close to the tab is lower. Furthermore, current density is highest around the diameter of the holes in the annulus. Hence, maximum temperature is seen at the open end.

Variation of maximum temperature in the entire model with respect to voltage is shown in Figure 81. It can be noted that the variation is almost quadratic in nature. This is to be expected since for a constant voltage, resistance heating varies with the square of voltage as shown in Eq.44.

$$Q = \frac{V^2}{R} \tag{44}$$

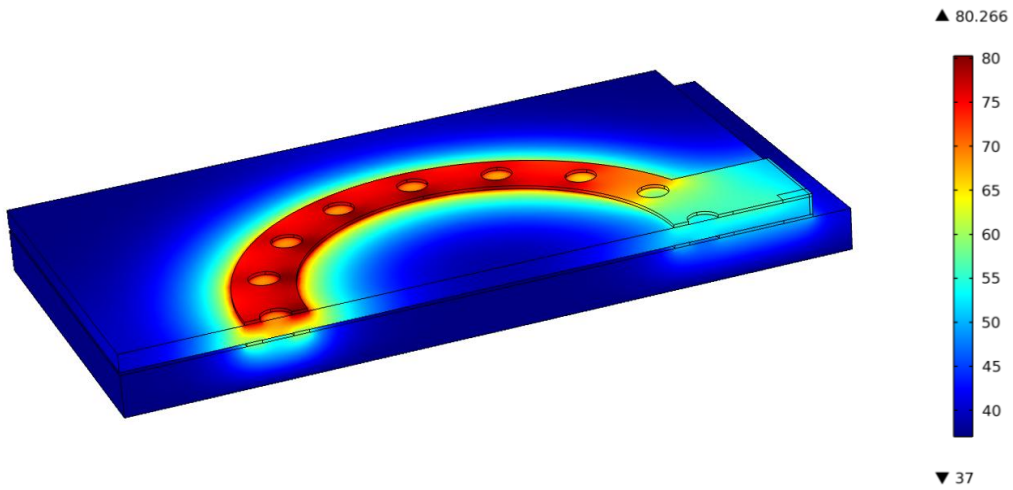

Figure 80: Temperature rise in model at 2s with 0.35 V applied voltage

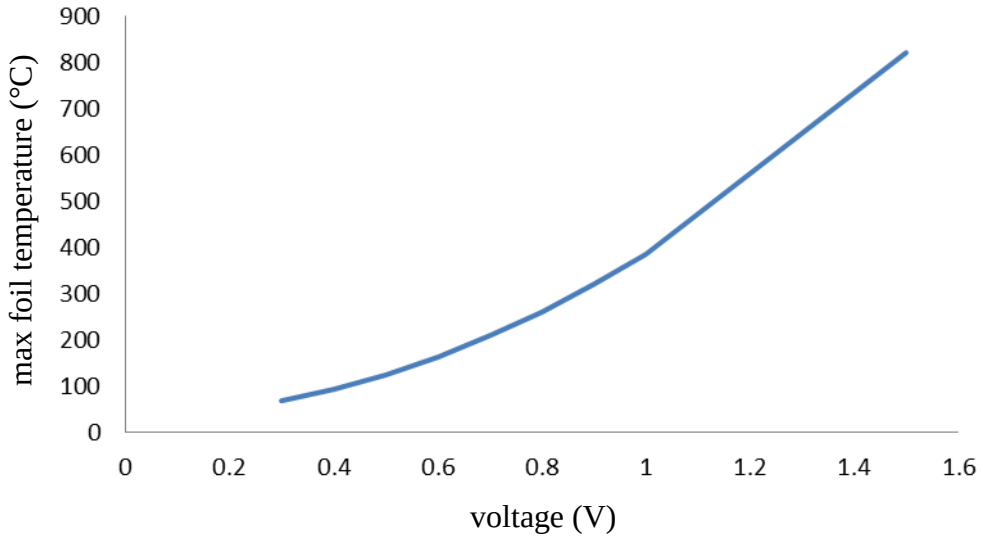

Figure 81: Maximum foil temperature as a function of applied voltage

Equation 45 can be used to verify the results of the finite element model by performing a heat balance. The tissue volume used in this analytical approximation is the volume under the foil since the FEA results show that most the temperature of the tissue away from the foil remains fairly unchanged. Heat loss by convection is calculated using Eq.7 where A is the annular area of the foil, and h_{pfo} is the convection coefficient of the fluid surrounding the foil. Heat loss by conduction is calculated by a lumped thermal resistance model using Eq. 8 to 10 as shown in Figure 82. Equations 45to 49 50 can be simplified to obtain Eq. 50 which gives the average temperature rise in the lumped mass model.

Table 22 compares the average temperature rise predicted by the finite element model with the average temperature rise predicted by the lumped thermal mass model. The lumped mass model predicts a much smaller temperature rise. This is because in the lumped mass model, the heat generation due to joule heating is assumed to be equally distributed throughout the volume. However, in the heat generation is concentrated mostly in the top foil which is also the material with the smaller specific heat. Hence, there is significantly higher temperature rise in the foil than in the rest of the model. This

localized heating is not captured by the lumped mass model and hence, it predicts a much lower temperature rise. However, it is still of the same order of magnitude and sufficiently validates the FEA results.

$$\Delta T_{avg} = \frac{\left(\frac{V^2}{R} - q_{cond} - q_{conv}\right)\delta t}{[(m_{foil} \cdot C_{p\,foil}) + (m_{tissue} \cdot C_{p\,tissue})]} \quad \textbf{(45)}$$

$$q_{conv} = h_{pfo} \cdot A \cdot \Delta T_{avg} \quad \textbf{(46)}$$

$$q_{cond} = \frac{\Delta T_{avg}}{R_{tot}} \quad \textbf{(47)}$$

$$R_{tot} = R_{th\,choroid} + R_{th\,bottom\,foil} + R_{th\,RPE} \quad \textbf{(48)}$$

$$R_{th} = \frac{L}{K \cdot A} \quad \textbf{(49)}$$

$$\Delta T_{avg} = \frac{\frac{V^2}{R}\delta t}{\left[(m_{foil} \cdot C_{p\,foil}) + (m_{tissue} \cdot C_{p\,tissue}) + \frac{\delta t}{R_{tot}} + h_{pfo} \cdot A \cdot \delta t\right]} \quad \textbf{(50)}$$

Table 22: Comparison between FEA model and lumped mass model

ΔT_{avg} (°C)	
FEA	**Lumped mass**
23	15

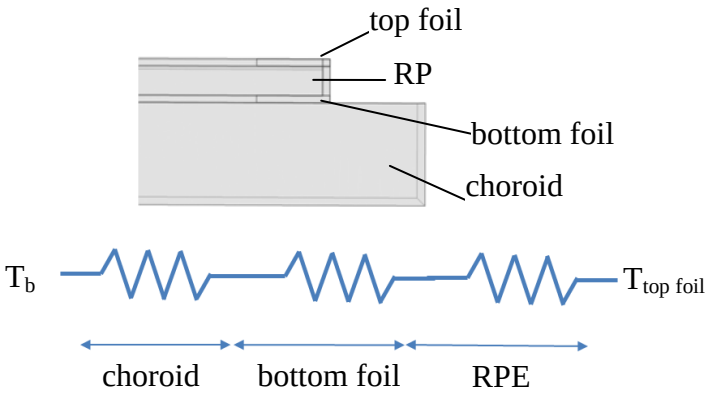

Figure 82: Lumped mass model for prediction of temperature rise

The FEA model can also be used to predict the ablation depth of the tissue when the foil is heated. The tissue sticks to the foil if its temperature reaches 70°C while it disintegrates if the temperature reaches 100°C. A voltage of 0.35 V causes the tissue to reach a maximum temperature of 80°C. As shown in Figure 83 the maximum depth at which temperature reaches 70°C gives the maximum adhesion depth, which in this case is 59 μm. This implies that the top foil will stick to the tissue while the bottom foil will not. There is also no adhesion near the tab since the temperature rise at the tab is much lower. Furthermore, the bottom foil will not stick to the choroid in this case. If the bottom foil sticks to the choroid, it would make extraction of the structure difficult. The results also suggest that the structure may need to be turned over and the bottom foil heated to cause it to stick to the tissue. Also, local heating of the tab may be required to raise the temperature locally to cause adhesion of the tissue. It is also noted that while adhesion occurs at the foil, the surrounding tissue is not damaged. In fact the tissue within the holes in the annulus remains fairly unaffected which is advantageous for vascularization of the tissue.

Equations 8 to 10 can be used to find the temperature gradient in the lumped model when the average foil temperature is 75°C. This in turn can be used to find the depth in the tissue at which the temperature reaches 70°C. Table 23 compares the depth predicted by the FEA model with that predicted by the lumped mass model. The lumped mass model predicts a higher depth since it assumes that the entire top foil is at a constant temperature. The FEA model captures the variation of temperature along the foil area and hence predicts a lower ablation depth. However, the lumped mass model validates the ablation depth predicted by the FEA model.

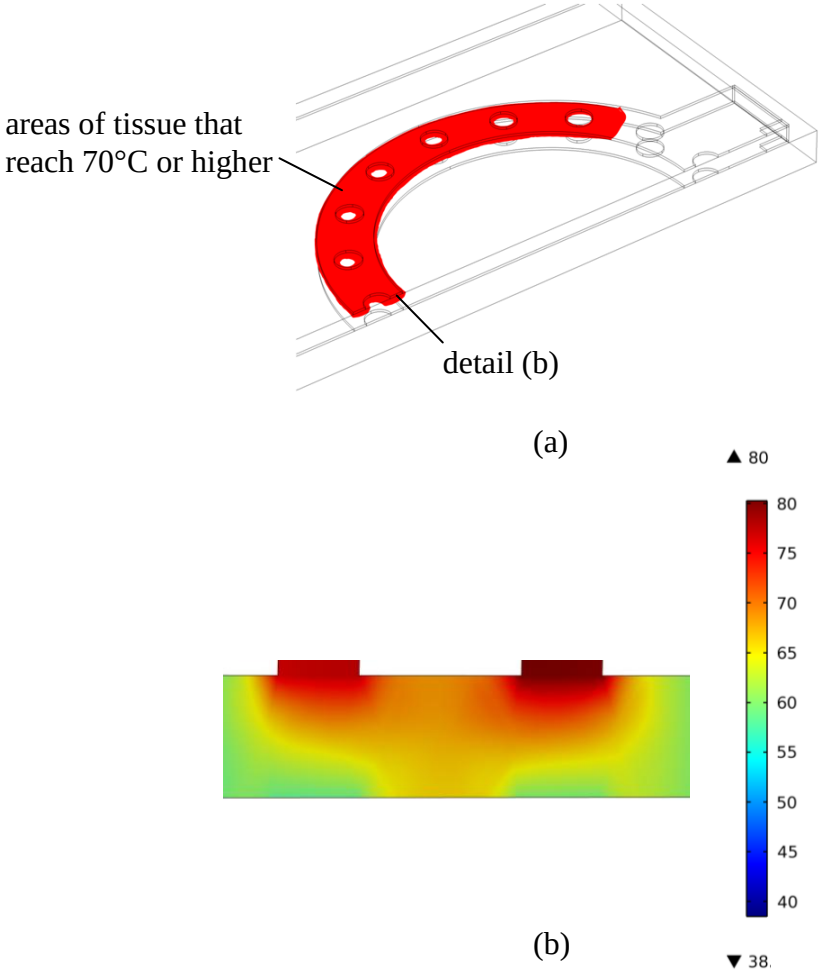

Figure 83: Temperature profile during thermal adhesion (a) Area of adhesion and ablation depth in tissue with 0.35V applied voltage (b) Cross sectional thermal profile at section with maximum temperature

Table 23: Comparison between adhesion depth predicted by FEA model and analytical model

Ablation depth (μm)	
FEA	**Analytical**
59	65.8

The model can also be used to check the effect of cauterizing the tissue patch around the structure before adhering the tissue to the structure. If the tissue is cauterized before adhesion, there will be no flow of blood through the RPE tissue. There would be no heat carried away by the blood and the perfusion term in Eq. 4 can be neglected for the RPE. Perfusion would still be present in the choroid. The simulation was run for 0.3V applied voltage with and without perfusion in the RPE. The results are summarized in Table 24 and indicate that the effect of cauterization on temperature in the tissue is not significant.

Table 24: Maximum temperature in tissue with and without cauterization with 0.3V

	not cauterized	**cauterized**
max temp (°C)	69.96	70.2

Convective heat transfer coefficient for perflourooctane was not found to be reported in literature and hence estimate of this value was used based on [125]. A sensitivity analysis was carried out to analyze the effect of this estimate on the results are shown in Figure 84. Typical values for oils are between 50 and 3000 W/m^2K, for which the maximum temperature reduces by about 30°C. This in turn would require a higher voltage to be applied to the foil. However, as shown in Figure 81, the increase in applied voltage would not be very significant. Other results such as the depth of thermally affected tissue are not affected by the variation in h_{pfo} since they depend mainly on the foil temperature.

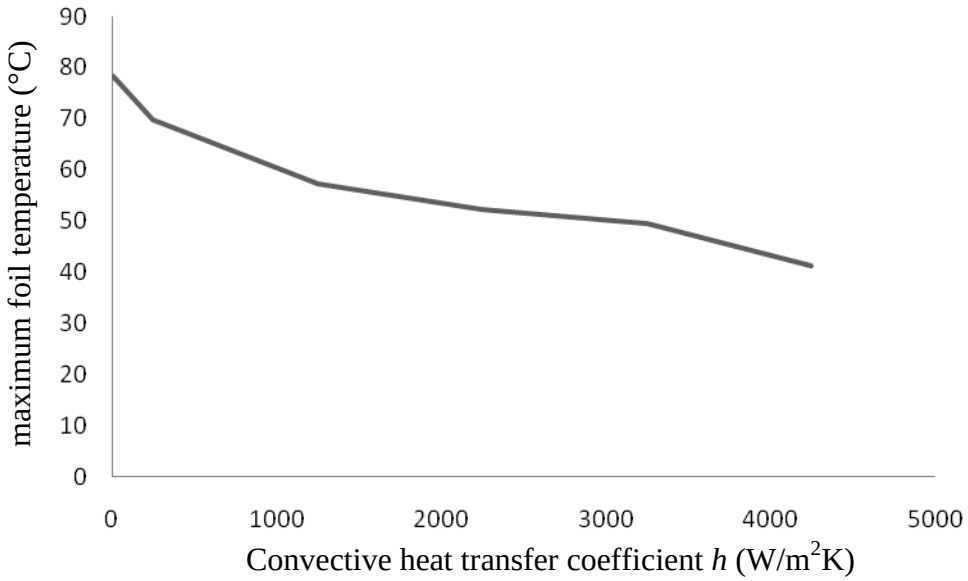

Figure 84: Variation of maximum foil temperature with change in convective heat transfer coefficient of fluid medium in the eye

Force measurement

The primary purpose of the device is to resist inplane forces that would cause the tissue to fold and wrinkle. Hence, the force required to pull the tissue out of the clamp was measured experimentally. A patch of the tissue graft was adhered to the translocation device ex-vivo with pig eyeballs. The graft was excised with excess tissue around the periphery to allow for the tissue to be gripped in a fixed clamp at one end. Weights were hung from the translocation device until it detached from the tissue. The maximum weight that the translocation device could withstand before it got detached from the tissue was noted. Multiple measurements were taken for devices with annular holes, with and without burrs. The mean of the measured values is shown in Figure 86 and suggests that the force is higher for the device with burrs. However, there is high variation in the measured values stemming from the variation in tissue properties within an eyeball and between eyeballs. The burrs on the devices used for these tests had a width of about 200 μm.

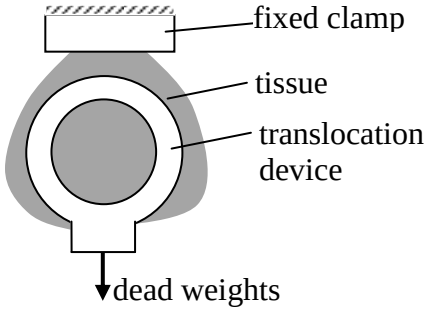

Figure 85: Pulling force measurement apparatus

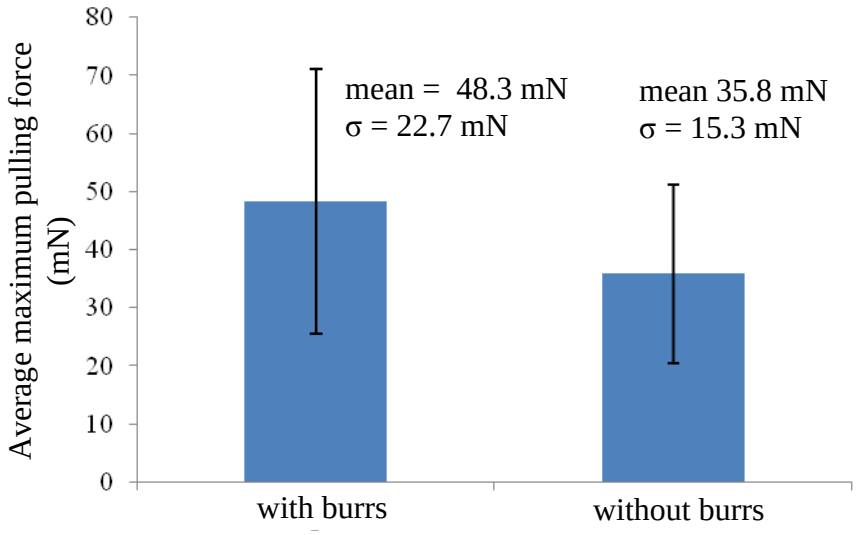

Figure 86: Pulling force for devices with and without burrs

Figure 87 shows images of the translocation device with and without burrs after a pull test. It can be seen that the burrs on the support surface provides toeholds and crevices for the tissue to anchor on to. The shape edges may also snag the tissue as it slides relative to the structure and mechanically restrain (hook) the tissue. They also increase the surface area for thermally induced adhesion. These burrs, however, are produced unintentionally during the milling process and hence, are an uncontrolled aspect of the design which is undesirable. If the size of these burrs is negligible, they will not provide adequate mechanical interlocking with the tissue. On the other hand if they are too large, they could potentially prevent full closure of the support structure, obstruct the tissue from contacting the rest of the foil and block the annular holes created to aid

vasularization (Figure 87). Furthermore, they could snag on the tissue as the support is inserted under the graft and hinder insertion. This suggests a need for a better control on the burr size and a deeper understanding of the factors that affect burr size and will be the subject of future research.

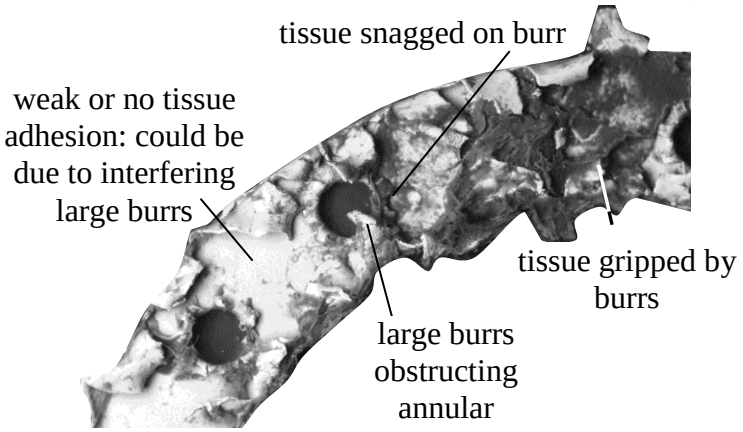

(a)

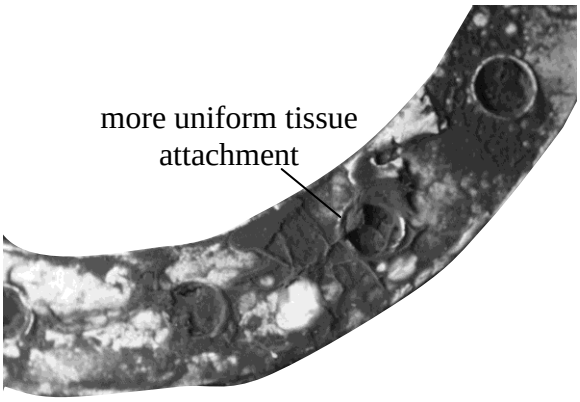

(b)

Figure 87: Support structure after the tissue was adhered to it and then pulled out of it. (a) device with burrs (b) deburred device

Conclusions

This chapter summarizes the analysis of a tissue support structure for translocation of a patch of tissue inside the eye. Based on the analysis, the following conclusions can be drawn:

- Clamping forces generated in the foil due to shape memory effect are negligible for the 25μm foil used. Significant clamping forces can be generated only if foil thickness is beyond 300 μm.
- The 25 μm foil can be rolled with a smallest diameter of 1.55 mm which is within the design criterion of 1.6 mm. Thicker foils cannot be bent in to a roll for insertion. Increasing the annulus hole size increases the minimum bend diameter.
- Device temperature is a function of current density and hence, the tab has the lowest temperature while the areas around the holes have a relatively higher temperature. Depth of thermally affected tissue when the foil is at 80°C is about 59μm. Most of the tissue graft is not damaged thermally. Blood flow in thin tissues such as the RPE does not significantly affect thermal gradients within the tissue due to an external heat source.
- The presence of burrs on the surface of the device grips the tissue and leads to better mechanical interlocking with it.

In the next chapter the conclusions of this dissertation are summarized and the objectives put forth in Chapter 1 are evaluated in light of these findings.

CHAPTER 8

CONCLUSIONS AND FUTURE WORK

In this chapter the conclusions from each chapter are juxtaposed with the research objectives proposed in Chapter 1 which were as follows:

- Evaluate abrasive slurry assisted brush deburring as a means to deburr microfeatures.
- Understand the mechanics of burr formation in thin foils as well as the effect of process parameters on the process.
- Understand the mechanics of material removal in brushing and abrasive impregnated brush deburring.
- Apply and verify the generated knowledge to the manufacture of a tissue translocation device.

Abrasive Slurry Assisted Deburring

This chapter focused on experimentally evaluating the applicability of abrasive assisted brush deburring to micromilled grooves and quantifying the effects of material hardness, spindle speed, grit size and type on the rate of burr height reduction. From this study, the following conclusions are drawn:

- A linear regression model can be used to predict the time required for completely deburring a micromilled groove based on the maximum initial burr height present, brush rotation speed and grit type. In these experiments, the model slightly underestimates the deburring time for the harder material (tool steel) and slightly overestimates the time for the softer material (copper).

- The deburring rate is proportional to the initial burr height with an almost constant proportionality for the conditions chosen in this study. An inference drawn from this is that the burrs either bend or break at about half the initial burr height. Deburring rate increases with spindle speed and is higher for diamond than SiC. No clear trend is evident for the influence of grit size.
- Groove depth change is small (for all conditions examined in this study) and is maximum for the largest diamond grit at the highest speed. The edge of the groove on the upmilling side exhibits a small radius due to the action of the abrasives.
- Large burrs shield some of the area next to them from the action of bristles resulting in a slope in the surface and a depression in the unshielded region.

The study showed that brush deburring can effectively remove large burrs in a few minutes with improvements in surface finish but the precision of the process is adversely affected by the large brush-workpiece interaction area and lack of control of the number of grits interacting with the workpiece. This addresses the first objective and it may be stated that 'Abrasive slurry assisted brush deburring effectively deburrs microgrooves but is difficult to control.' Brush deburring has been suggested as the first method of choice for deburring microfeatures but has not been systematically evaluated. This study makes significant contribution by filling this gap in knowledge.

Burr Formation in Thin Foils

This chapter focused on presenting a fundamental understanding of the mechanics of burr formation in micromilling of a thin nitinol foil adhered to a backing material. The following conclusions are drawn:

- Burrs are formed via ploughing as the tool initially penetrates the foil, mainly due to delamination and insufficient chip thickness. If initial penetration is sufficient to cause the foil to fail in tension, the foil tears with the crack starting closer to the upmilling side and thereby resulting in larger downmilling burrs. If penetration is insufficient, the foil plastically deforms until it tears typically in the middle of the tooth path.
- The kinematic model developed captures the effects of feed per tooth, tool tip radius and adhesive peel strength to predict the burr width and is shown to be within the experimental variation.
- At higher feeds, with a new tool and a strong adhesive bond, chips of the material are formed leading to very small burrs on either side of the groove.
- Three types of burrs were identified: rollover, feathery and wall type. Feathery burrs are produced only on the downmilling side when cutting with sufficient chip thickness, moderate bond strength and a new tool. Wall burrs are formed with worn tools at higher feeds due to moderate delamination on the downmilling side. Rollover burrs are formed in all other cases.
- The effect of downmilling on burr height is most pronounced except when there is significant delamination on the upmilling side.
- Wear of the tool results in larger burrs. Increasing the feed from insufficient chip thickness (< 5 μm in this work) to sufficient chip thickness (5 to 10 μm in this work) reduces the burr height if the tool is new, whereas it increases the burr height if the tool is worn.
- Spindle speed (strain rate effect) does not have a significant effect on the burr height for a new tool. For a worn tool, a lower spindle speed (more time for delamination) results in larger burrs.

- PMMA is a softer backing material and yields larger burrs and has a higher tendency for forming a built-up edge, which in turn produces larger burrs.
- A weak adhesive bond with the backing material also leads to larger burrs.
- Variation in burr height is smallest for a feed of 7.5 μm/tooth, high bond strength and cutting with a new tool.

In short, it has been shown that process parameters such as the feed per tooth and milling side (up vs. down), workpiece conditions such as adhesive-backing material combination (which affects adhesive strength) and the tool properties such as tool edge radius and wear noticeably affect burr size. The variation of burr width with feed per tooth has been captured by a kinematic model whose predictions are within the experimental variation. The smallest experimental variation for the predicted value was about 75 μm at a feed of 7.5 μm/tooth. This addresses the second objective and it may be stated that 'Process parameters, especially feed per tooth, in micromilling of thin foils affect burr size and burr width can be predicted within a range.' Burr formation in machining of microscale features in thin metal foils is influenced by the edge radius and foil delamination, which make it a distinct process from macromachining or micromachining of bulk materials. This thesis has for the first time shed light on the mechanics of burr formation in this process as well as the effect of process parameters on burr width. An experimentally verified model has also been presented allowing to these results to be generalized.

Deburring of Thin Foils

This chapter sought to shed light on material removal in abrasive impregnated brushing of thin (25 μm) metallic foils. The following conclusions are arrived at in this study:

- For brushing of a flat surface, some material is removed as chips by the impregnated abrasives. Material is also deformed by the grits and pushed up to form ledge like structures or microburrs which then break off due to impact or stiffness forces improved by subsequent bristles.
- The maximum normal force and maximum indentation shifts from the middle of the brushed region at 5,000 rpm to the entry region at 15,000 rpm due to a shift from a bristle stiffness dominated force to an impact dominated force.
- A Hertzian static indentation model used to predict indentation rate during brushing of foils shows good agreement with experiments.
- Burr removal occurs in two phases. Phase I involves fatigue fracture of the long slender burrs at the root. Phase II involves material being removed as flakes as the cracks formed during fracture in Phase I and new cracks formed during brushing propagate through the burr.
- A fracture mechanics model based on the Paris equation can predict the number of passes required to deburr an edge and further supports the hypothesis that material removal in brushing of Nitinol is better described by fracture mechanics.
- Burrs can be removed within 12 minutes for a 6 mm long groove with no more than a micron change in foil thickness.
- Surface finish initially improves for the pickled foils during Phase I but subsequently degrades in Phase II due to impact of the bristles.

In summary, abrasive grits impregnated in the brush bristles indent the workpiece material either due to the stiffness of the bristles or due to initial contact forces with the latter dominating at higher brush rotation speeds. During abrasive impregnated brush deburring, burrs are removed via crack propagation due to action of the bristles in two phases. Hertzian static indentation and the Paris equation for fracture mechanics are able

to describe workpiece indentation during brushing and brush deburring respectively. This addresses the third objective and it may be stated that 'Material indentation in abrasive impregnated brush deburring is dominated by bristle stiffness at low speeds and impact at high speeds and brush deburring occurs due to fracture of burrs.' This study significantly deepens the understanding of material removal in brushing, which has been long identified as an important and unaddressed gap in the knowledge of brushing and brush deburring. It has shown that deburring occurs by fracture rather than bending failure. The experimentally verified models help explain the shift in the position of maximum material penetration with increase in speed while also allowing the material penetration rate and number of deburring passes to be predicted.

Design of Surgical Support Structure

This chapter presented the systematic design of a device to translocate tissue inside the eye for surgical correction of AMD. The following conclusions are drawn:

- Currently used tissue translocation techniques have significant limitations to perform translocation in the eye.
- A novel device was designed and manufactured out of thin Nitinol foil can be inserted through a 2 mm incision in the eye by rolling it. The rolled coil can be successfully unrolled in the eye using shape memory effect caused by electrical heating.
- The adhesion of the tissue to the device is achieved by electrically heating it beyond the shape transformation temperature of the structure.
- The adhesion of the tissue to the foil structure is further improved by the presence of burrs along the edge of the device. These burrs are produced during the micromilling process and act as microscopic hooks to anchor the tissue to the foil structure.

- The predictions for burr size from Chapter 4 and deburring passes from Chapter 5 can be successfully applied to the device to produce either large (~200 μm) burrs or small (~ 40 μm) burrs as well as to fully deburr them.
- The device can successfully grasp and translocate a patch of tissue in both ex-vivo and in-vivo tests carried out on pig eyes.

Analysis of Tissue Support Device

This chapter summarizes the analysis of a tissue support structure for translocation of a patch of tissue inside the eye. Based on the analysis, the following conclusions can be drawn:

- Clamping forces generated in the foil due to shape memory effect are negligible for the 25μm foil used. Significant clamping forces can be generated only if the foil thickness is greater than 300 μm.
- The 25 μm foil can be rolled with a smallest diameter of 1.55 mm which is within the design criterion of 1.6 mm. Thicker foils cannot be bent into a roll for insertion. Increasing the annulus hole size increases the minimum bend diameter.
- Device temperature is a function of current density and hence, the tab has the lowest temperature while the areas around the holes have a relatively higher temperature. Depth of thermally affected tissue when the foil is at 80°C is about 59μm. Most of the tissue graft is not damaged thermally. Blood flow in thin tissues such as the RPE does not significantly affect thermal gradients within the tissue due to an external heat source.
- The presence of burrs on the surface of the device leads to better mechanical interlocking with it.

Knowledge of micromilling of thin metal foils has been applied to a systematically designed medical device for translocation of a tissue graft inside the eye.

The models in Chapter 4 and 5 can be successfully applied to predict the burr size on the device within a range as well as the number of passes required to deburr the device. Finite element analysis of the device shows that the forces generated due to shape memory effect are insufficient by themselves to hold the tissue graft. On the other hand, experiments show that heating the device sufficiently causes the tissue to stick to the annular surface allowing the tissue to be successfully harvested and translocated. SEM images of the device after the tissue has been removed from the device show that the burrs enhance retention of the tissue by acting as microhooks. This addresses the fourth objective and it may be stated that 'Burrs on a surgical micromilled device snag tissue and assist tissue retention.' This device aids in the surgical correction of one of the leading causes of blindness in the world.

Future Work

Burr Formation

Following are some areas where the current research in the area of burr formation during micromilling of thin foils may be extended:

- Verification of the extent of delamination between the foil and backing material experimentally to validate the predictions of this study.
- Understanding the process by which cracks are generated during burr formation rather than assuming the cracks to occur at the middle of the delaminated area.
- As the tool follows a curved path, the actual uncut chip thickness would vary from the feed per tooth and would affect the predicted transition feed from ploughing to cutting. Hence, the model developed in this study could be connected to some of the tool path planning algorithms that have been

reported in literature to study burr formation for features that are not straight grooves.

- Evaluation of the effect of pretensioning the foil or sandwiching it between stiffer materials (such as adhesive tape with card paper) on burr size. It is expected that both these strategies would reduce the tendency of the foil to delaminate from the backing material and reduce burr formation.

Abrasive Impregnated Brush Deburring

- Developing an understanding of the impact dynamics of the bristles as they contact the workpiece.
- Develop a statistical model of abrasive grit sizes, shapes, distribution and radii to predict the indentation process more accurately.
- Develop methods to improve surface roughness during Phase II of the deburring process.

Tissue Translocation Device

- Understand the biomechanics of tissue-burr interaction.
- Create deterministic features on the foil surface to enhance burr retention.
- Carry out in-vivo surgical tests to evaluate the viability as a long term implant in the eye.

REFERENCES

[1] Ali, M., Omar, M., Othman, K., and Hung, W., 2009, "Prediction of Burr Formation in Fabricating Mems Components by Micro End Milling," Advanced Materials Research, 74, pp. 247-250.

[2] Thomas, G., and Crol, H., 2000, "New Options for Micromachining Medical Devices," Medical Device and Diagnostic Industry Magazine, http://www.mddionline.com, Accessed November 12, 2012.

[3] Lee, K., and Dornfeld, D., 2005, "Micro-Burr Formation and Minimization through Process Control," Precision Engineering, 29(2), pp. 246-252.

[4] Felix, C., 2007, Ban the Burr- a Look at ECD, September 08, 2012, http://www.productionmachining.com

[5] Sockman, J., 2006, Selecting Brushes for Burrs, www.productionmachining.com, Accessed Septemer 08, 2012.

[6] Gillespie, L. K., 2010, "Deburring, Deflashing and Edge Finishing Micro Parts," SME Micro Manufacturing Conference, Dearborn, MI, pp.12-14.

[7] Microlution, Case Studies, http://microlution-inc.com/solutions/casestudies.php, Accessed November 12, 2012

[8] Kathuria, Y. P., 2005, "Laser Microprocessing of Metallic Stent for Medical Therapy," Journal of Materials Processing Technology, 170, pp. 545-550.

[9] Takahata, K., and Gianchandani, Y., 2004, "A Planar Approach for Manufacturing Cardiac Stents: Design, Fabrication, and Mechanical Evaluation," Journal of Microelectromechanical Systems, 13(6), pp. 933-939.

[10] Cassidy, V., 2008, "Ultrafast Track: The buzz about ultrafast-pulse lasers gets louder," MICROmanufaturing, 1, pp 1-3.

[11] Richter, A., 2008," Building for Micromachining," Cutting Tool Engineering, 60, pp 1-8.

[12] Schaffer, C. B., Brodeur, A., and Mazur, E., 2001, "Laser-Induced Breakdown and Damage in Bulk Transparent Materials Induced by Tightly Focused Femtosecond Laser Pulses," Measurement Science and Technology, 12(11), pp. 1784-1794.

[13] Zheng, L., Wang, C., Yang, L., Song, Y., and Fu, L., 2012, "Charachteristics of Chip Formation in the Mirco-Drilling of Multi-Material Sheets," International Journal of Machine Tools and Manufacture, 52, pp. 40-49.

[14] Olsen, T. W., Lotfness, P. E., and Erdman, A. G., 2007, "Surgical Support Structure", US Patent # 20070179512.

[15] Klein, R., Klein, B. E., and Linton, K. L., 1992, "Prevalence of Age-Related Maculopathy. The Beaver Dam Eye Study," Ophthalmology, 99(6), pp. 933-43.

[16] Brown, G. C., Brown, M. M., Sharma, S., Stein, J. D., Roth, Z., Campanella, J., and Beauchamp, G. R., 2005, "The Burden of Age-Related Macular Degeneration: A Value-Based Medicine Analysis," Trans Am Ophthalmol Soc, 103, pp. 173-84; discussion 184-6.

[17] NEI, 2010, Facts About Age-Related Macular Degeneration, http://www.nei.nih.gov/health/maculardegen/armd_facts.asp, Accessed November 12, 2012.

[18] Vanmeurs, J. C., and Biesen, P. R. V. D., 2003, "Autologous Retinal Pigment Epithelium and Choroid Translocation in Patients with Exudative Age-Related Macular Degeneration: Short-Term Follow-Up," American Journal of Ophthalmology, 136(4), pp. 688-695.

[19] Maaijwee, K., Heimann, H., and Missotten, T., 2007, "Retinal Pigment Epithelium and Choroid Translocation in Patients with Exudative Age-Related Macular Degeneration: Long-Term Results," Archive for Clinical and Experimental Ophtalmology, 245, pp. 1681-1689.

[20] Gillespie, L. K., 1999, Deburring and Edge Finishing Handbook, SME Press, p. 36.

[21] Gillespie, L. K., Neal, B. J., and Albright, R. K., 1976, "Burrs Produced by End Milling," Technical Report No. Bendix Corp., Kansas.

[22] Nakayama, K., and Arai, M., 1987, "Burr Formation in Metal Cutting," Annals of the CIRP, 36, pp. 33-36.

[23] Ko, S., and Dornfeld, D., 1991, "A Study of Burr Formation Mechanism," Journal of Engineering Materials and Technology, 113, pp. 75-87.

[24] Hashimura, M., Ueda, K., Dornfeld, D., and Manabe, K., 1995, "Analysis of Three-Dimensional Burr Formation in Oblique Cutting," Annals of the CIRP, 44, pp. 27-30.

[25] Ko, S., and Dornfeld, D., 1996, "Burr Formation and Fracture in Oblique Cutting," Journal of Materials Processing Technology, 62, pp. 24-36.

[26] Rubenstein, C., 1983, "The Mechanics of Continuous Chip Formation in Oblique Cutting in the Absence of Chip Distortion. Part 1—Theory," International Journal of Machine Tool Design and Research, 23, pp. 11-20.

[27] Hashimura, M., Chang, Y. P., and Dornfeld, D., 1999, "Analysis of Burr Formation Mechanism in Orthogonal Cutting," Journal of Manufacturing Science and Engineering, 121, pp. 1-7.

[28] Park, I. W., and Dornfeld, D., 2000, "A Study of Burr Formation Processes Using the Finite Element Method: Part I," Journal of Engineering Materials and Technology, 122, pp. 221-228.

[29] Park, I. W., and Dornfeld, D., 2000, "A Study of Burr Formation Processes Using the Finite Element Method: Part Ii - the Influences of Exit Angle, Rake Angle, and Backup Material on Burr Formation Processes," Journal of Engineering Materials and Technology, 122(pp. 229-237.

[30] Min, S., Dornfeld, D., Kim, J., and Shyu, B., 2001, "Finite Element Modeling of Burr Formation in Metal Cutting," eds., Delft, Netherlands, pp. 97-104.

[31] Leopold, J., and Wohlgemuth, R., 2009, " Modeling and Simulation of Burr Formation: State-of-the-Art and Future Trends ," Proceedings of the CIRP International Conference on Burrs, Kaiserslautern, Germany, pp. 79-86.

[32] Aurich, J. C., and Sudermann, H., 2005, "Characterisation of Burr Formation in Grinding and Prospects for Modelling," CIRP Annals - Manufacturing Technology, 54, pp. 313-316.

[33] Guo, Y. B., and Dornfeld, D., 1998, "Finite Element Analysis of Drilling Burr Minimization with a Backup Material," NAMRC, Atlanta, GA, 207-212.

[34] Hellstern, C., 2009, "Investigation of Interlayer Burr Formation in the Drilling of Stacked Aluminum Sheets," Ph.D. Thesis, Georgia Institute of Technology, Atlanta.

[35] Liles, H., and Mayor, R., 2012, "Initial Study on the High-Speed, High-Precision Micromilling of Laminated Electric Steels," Proceedings of the International Conference of Micromanufacturing, Evanston, IL, Paper 105.

[36] Performance Microtool, 2012, Microtool Catalog, pmtnow.com, Accessed December 7, 2012.

[37] Sugawara, A., and Inagaki, K., 1982, "Effect of Workpiece Structure on Burr Formation in Micro-Drilling," Precision Engineering, 4, pp. 9-14.

[38] Stein, J. M., and Dornfeld, D. A., 1997, "Burr Formation in Drilling Miniature Holes," CIRP Annals - Manufacturing Technology, 46(1), pp. 63-66.

[39] Lee, K., and Dornfeld, D., 2002, "An Experimental Study on Burr Formation in Micro Milling Aluminum and Copper," Transactions of NAMRI/SME, 30, pp. 255-262.

[40] Chern, G., Wu, Y., Cheng, J., and Yao, J., 2007, "Study on Burr Formation in Micro-Machining Using Micro-Tools Fabricated by Micro-Edm," Precision Engineering, 31(2), pp. 122-129.

[41] Liu, X., Devor, R. E., and Kapoor, S. G., 2004, "The Mechanics of Machining at the Microscale: Assessment of the Current State of the Science," Journal of Manufacturing Science and Engineering, 126(4), pp. 666-678.

[42] Mcmaster-Carr, 2012, www.mcmastercarr.com, Accessed November 12, 2012.

[43] Cambron, S., Keynton, R., and Franco, J., 2003, "Design and Fabrication of Microtacks for Retinal Implant Applications," Washington, DC, USA, pp. 247-249.

[44] Huang, H., 2004, "A Study of High-Speed Milling Characteristics of Nitinol," Materials and Manufacturing Processes, 19, pp. 159-175.

[45] Weinert, K., and Petzoldt, V., 2004, "Machining of Niti Based Shape Memory Alloys," Materials Science and Engineering: A, 378, pp. 180-184.

[46] Weinert, K., and Petzoldt, V., 2008, "Machining Niti Micro-Parts by Micro-Milling," Materials Science and Engineering: A, 481-482, pp. 672-675.

[47] Biermann, D., Kahleyss, F., Krebs, E., and Upmeier, T., 2011, "A Study on Micro-Machining Technology for the Machining of Niti: Five Axis Micro-Milling and Micro Deep-Hole Drilling," Journal of Materials Engineering and Performance, 20, pp. 745-751.

[48] Stango, R. J., Heinrich, S. M., and Shia, C. Y., 1989, "Analysis of Constrained Filament Deformation and Stiffness Properties of Brushes," Journal of Engineering for Industry, 111, pp. 238-243.

[49] Stango, R. J., Cariapa, V., Prasad, A., and Liang, S.-K., 1991, "Measurement and Analysis of Brushing Tool Performance Charachteristics, Part I: Stiffness Response," Journal of Engineering for Industry, 113, pp. 283-289.

[50] Shia, C. Y., 1988, "Analysis of Constrained Deformation of a Circular Brush System," Ph.D. Thesis, Marquette University, Milwaukee, WI.

[51] Shia, C. Y., Stango, R. J., and Heinrich, S. M., 1989, "Theoretical Analysis of Frictional Effect on Circular Brush Stiffness Properties," SME Deburring and Surface Conditioning Conference, San Diego, CA, pp.1-18.

[52] Cariapa, V., Stango, R. J., Liang, S.-K., and Prasad, A., 1991, "Measurement and Analysis of Brushing Tool Performance Charachteristics, Part Ii: Contact Zone Geometry," Journal of Engineering for Industry, 113, pp. 290-296.

[53] Cariapa, V., Stango, R. J., Chen, L., and Hermann, R., 1992, "Aspects of Process Model for Automatic Control of Edge-Deburring with Filamentary Brush," Journal of Manufacturing Science and Engineering, 114, pp. 294-300.

[54] Shia, C. Y., and Stango, R. J., 1997, "Analysis of a Compliant Honing Tool for Brushing Cylindrical Surfaces," Journal of Manufacturing Science and Engineering, 119, pp. 441-444.

[55] Stango, R. J., and Shia, C. Y., 1997, "Analysis of Filament Deformation for a Freely Rotating Cup Brush," Journal of Manufacturing Science and Engineering, 119, pp. 298-306.

[56] Shia, C. Y., Stango, R. J., and Heinrich, S. M., 1998, "Analysis of Contact Mechanics for a Circular Filamentary Brush/Workpart System," Journal of Manufacturing Science and Engineering, 120, pp. 715-721.

[57] Stango, R. J., Chen, L., and Cariapa, V., 1999, "Automated Deburring with a Filamentary Brush: Prescribed Burr Geometry," Journal of Manufacturing Science and Engineering, 121, pp. 385-392.

[58] Stango, R. J., Cariapa, V., and Zuzanski, M., 2005, "Contact Zone Force Profile and Machining Performance of Filamentary Brush," Journal of Manufacturing Science and Engineering, 127, pp. 217-226.

[59] Sedriks, A. J., and Mulhearn, T. O., 1963, "Mechanics of Cutting and Rubbing in Simulated Abrasive Processes," Wear, 6, pp. 457-466.

[60] Aghan, R. L., and Samuels, L. E., 1970, "Mechanisms of Abrasive Polishing," Wear, 16, pp. 293-301.

[61] Bowden, F. P., and Tabor, D., 1966, "Friction, Lubrication and Wear: A Survey of Work During the Last Decade," British Journal of Applied Physics, 17, pp. 1521-1544.

[62] Evans, C., Paul, E., Dornfeld, D., Lucca, D., Byrne, G., Tricard, M., Klocke, F., Dambon, O., and Mullany, B., 2003, "Material Removal Mechanisms in Lapping and Polishing," CIRP Annals - Manufacturing Technology, 52(2), pp. 611-633.

[63] Fitzpatrick, P. R., and Paul, F. W., 1987, Robotic Finishing Using Brushes- Material Removal Mechanics, Creative Manufacturing Engineering Program- Mr87-156, SME, Dearborn, MI.

[64] CPOB, 2009, Comparison of Age-Related Macular Degeneration Treatments Trials (CATT), http://www.med.upenn.edu/cpob/studies/CATT.shtml, Accessed November 12, 2012.

[65] Yehoshua, Z., Rosenfeld, P. J., and Albini, T. A., 2011, "Current Clinical Trials in Dry Amd and the Definition of Appropriate Clinical Outcome Measures," Seminars in Ophthalmology 26(3), pp. 167-180.

[66] Eandi, C. M., Giansanti, F., and Virgili, G., 2008, "Macular Translocation for Neovascular Age-Related Macular Degeneration," Graefes Archive for Clinical and Experimental Ophthalmology, 4, pp. 1-27.

[67] Chen, F. K., Uppal, G. S., Maclaren, R. E., Coffey, P. J., Rubin, G. S., Tufail, A., Aylward, G. W., and Da Cruz, L., 2009, "Long-Term Visual and Microperimetry Outcomes Following Autologous Retinal Pigment Epithelium Choroid Graft for Neovascular Age-Related Macular Degeneration," Clinical & Experimental Ophthalmology, 37(3), pp. 275-285.

[68] Binder, S., Stanzel, B. V., Krebsa, I., and Glittenberg, C., 2007, "Transplantation of the Rpe in Amd," Progress in Retinal and Eye Research, 26, pp. 516-554.

[69] Olsen, T. W., and Pribila, J. T., 2010, "Pars Plana Vitrectomy with Endoscope-Guided Sutured Posterior Chamber Intraocular Lens Implantation in Children and Adults," American Journal of Ophthalmology, 151(2), pp. 287-296.

[70] Olsen, T. W., Mathai, G. K., Loftness, P. E., Melkote, S. N., Rosen, D. W., and Erdman, A. G., 2012, "A Novel Surgical Technique for Submacular TissueTranslocation Using the in vivo Porcine Model," Annual Macula Society Meeting, Jerusalem, Israel.

[71] Falk, F., 1983, "One-Dimensional Model of Shape Memory Alloys," Archives of Mechanics 35(1), pp. 63-84.

[72] Tanaka, K., 1986, "A Thermomechanical Sketch of Shape Memory Effect: One-Dimensional Tensile Behavior," Res Mechanica, 18(3), pp. 251-263.

[73] Brinson, L. C., and Lammering, R., 1993, "Finite Element Analysis of the Behavior of Shape Memory Alloys and Their Applications," International Journal of Solids and Structures, 30(23), pp. 3261-3280.

[74] Pelton, A. R., Rebelo, N., Duerig, T. W., and Wick, A., 1994, "Experimental and FEM Analysis of the Bending Behavior of Superelastic Tubing," Shape Memory and Superelastic Technologies, Pacific Grove, CA, pp. 353-358.

[75] Auricchio, F., and Taylor, R. L., 1997, "Shape-Memory Alloys: Modelling and Numerical Simulations of the Finite-Strain Superelastic Behavior," Computer Methods in Applied Mechanics and Engineering, 143(1-2), pp. 175-194.

[76] Gong, X.-Y., Pelton, A. R., Duerig, T. W., Rebelo, N., and Perry, K., 2003, "Finite Element Analysis and Experimental Evaluation of Superelastic Nitinol Stent," Pacific Grove, California, USA, pp. 453-462.

[77] Terriault, P., Viens, F., and Brailovski, V., 2006, "Non-Isothermal Finite Element Modeling of a Shape Memory Alloy Actuator Using Ansys," Computational Materials Science, 36(4), pp. 397-410.

[78] Müller, I., and Xu, H., 1991, "On the Pseudo-Elastic Hysteresis," Acta Metallurgica et Materialia, 39(3), pp. 263-271.

[79] Vankov, A., Huie, P., Blumenkranz, M., and Palanker, D., 2004, "Electro-Adhesive Forceps for Tissue Manipulation," San Jose, CA 5, pp. 270– 274.

[80] Knulst, A. J., Maaijwee, K., Van Meurs, J. C., Wieringa, P. A., Breedveld, P., and Schutte, S., 2009, "Micro-Scale Thermal Tissue Gripper," Minimally Invasive Therapy & Allied Technologies, 18(1), pp. 8-14.

[81] Matsudaira K., Nakagawa H., Wittkampf F. H., Yamanashi W. S., Imai S., Pitha J. V., Lazzara R., and M., J. W., 2003, "High Incidence of Thrombus Formation without Impedance Rise During Radiofrequency Ablation Using Electrode Temperature Control.," Pacing and Clinical Electrophysiology, 26(5), pp. 1227-1237.

[82] Wittkampf F. H., and H., N., 2006, "R F Catheter Ablation:Lessons on Lesions," Pacing and Clinical Electrophysiology, 29(11), pp. 1285-1297.

[83] Stringer H., and Parr J., 1964, "Shrinkage Temperature of Eye Collagen," Nature, 204, pp. 1307.

[84] Shimko, N., Savard, P., and Shah, K., 2000, "Radio Frequency Perforation of Cardiac Tissue: Modelling and Experimental Results," Medical and Biological Engineering and Computing, 38, pp. 575-582.

[85] Scott, J. A., 1988, "A Finite Element Model of Heat Transport in the Human Eye," Physics in Medicine and Biology, 33(2), pp. 227-241.

[86] Cvetkovic, M., Poljak, D., and Peratta, A., 2008, "Thermal Modelling of the Human Eye Exposed to Laser Radiation," Proceedings of International Conference on Software, Telecommunications and Computer Networks, Split-Dubrovnik, Croatia, pp. 16-20.

[87] Berjano, E. J., 2006, "Theoretical Modeling for Radiofrequency Ablation: State-of-the-Art and Challenges for the Future," BioMedical Engineering OnLine, 5(1), pp. 24.

[88] Berjano E. J., Saiz J., Alió J. L., and M., F. J., 2003, "Ring Electrode for Radio-Frequency Heating of the Cornea: Modelling and in Vitro Experiments.," Medical and Biological Engineering and Computing, 41(6), pp. 630-639.

[89] Mathai, G. K., and Melkote, S. N., 2010, "Deburring of Microgrooves by Abrasive Brushing," Madison, WI, pp. 1-7.

[90] Vander Voort, G. F., 1999, Metallography: Principles and Practice, ASM International, Materials Park, Ohio, p. 145.

[91] Franke, V., Leitz, L., and Aurich, J. C., 2010, "Burr Measurement: A Round Robin Test Comparing Different Methods," Burrs- Analysis, Control and Removal, 5(pp. 167-178.

[92] Fujita, H., Shinmura, T., and Yamaguchi, H., 2007, "Magnetic-Field-Assisted Finishing with Axial Vibration -Deburring on Internal Holes and Internal Finishing of Pipes with Rectangular Cross-Sections," Key Engineering Materials, 329(pp. 261-266.

[93] Dornfeld, D. A., and Min, S., 2009," A Review of Burr Formation in Machining," Proceedings of the CIRP International Conference on Burrs, Kaiserslautern, Germany, pp. 3-11.

[94] Madarkar, R., and Jain, V. K., 2007, "Investigation into Magnetic Abrasive Micro Deburring (Mamde)," India, pp. 307-312.

[95] Jang, K.-I., Kim, D.-Y., Maeng, S., Lee, W., Han, J., Seok, J., Je, T.-J., Kang, S., and Min, B.-K., 2012, "Deburring Microparts Using a Magnetorheological Fluid," International Journal of Machine Tools and Manufacture, 53, pp. 170-175.

[96] Wu, C. F., and Hamada, M. S., 2009, Experiments: Planning, Analysis and Optimization, John Wiley and Sons, pp. 128-131.

[97] Mulhearn, T. O., and Samuels, L. E., 1962, "The Abrasion of Metals: A Model of the Process," Wear, 5, pp. 478-498.

[98] Lai, J.-Y., Saka, N., and Chun, J.-H., 2002, "Evolution of Copper-Oxide Damascene Structures in Chemical Mechanical Polishing," Journal of The Electrochemical Society, 149(1), pp. G31-G40.

[99] ASTM, 2010, "Standard Test Method for Peel or Stripping Strength on Adhesive Bonds," Document D903.

[100] Pelton, A. R., Dicello, J., and Miyazaki, S., 2000, "Optimisation of Processing and Properties of Medical Grade Nitinol Wire," International Conference on Shape Memory and Superelastic Technologies, Pacific Grove, CA, pp. 361-374.

[101] Buehler, W. J., and Wang, F. E., 1968, "A Summary of Recent Research on the Nitinol Alloys and Their Potential Application in Ocean Engineering," Ocean Engineering, 1, pp. 105-120.

[102] Mathai, G. K., Melkote, S. N., and Rosen, D. W., 2012, "Effect of Machining Parameters on Burr Size of Micromilled Foils," ICOMM, Evanston, IL, Paper # 129.

[103] Mathai, G. K., and Melkote, S. N., 2012, "Effect of Process Parameters on the Rate of Abrasive Assisted Brush Deburring of Microgrooves," International Journal of Machine Tools and Manufacture, 57, pp. 46-54.

[104] Schilhansl, M. J., and Providence, R. I., 1958, "Bending Frequency of a Rotating Cantilever Beam," Journal of Applied Mechanics, 25, pp. 28-30.

[105] Che, W., Guo, Y., Chandra, A., and Bastawros, A., 2005, "A Scratch Intersection Model of Material Removal During Chemical Mechanical Planarization (Cmp)," Journal of Manufacturing Science and Engineering, 127, pp. 545-554.

[106] Dintwa, E., Tijskens, E., and Ramon, H., 2008, "On the Accuracy of the Hertz Model to Describe the Normal Contact of Soft Elastic Spheres," Granular Matter, 10, pp. 209-221.

[107] Fischer-Cripps, A. C., 1999, "The Hertzian Contact Surface," Journal of Materials Science, 34, pp. 129-137.

[108] MSC ADAMS, 2005, "Material Contact Properties Table", MSC ADAMS Help Manual.

[109] NIST, 2001, Ceramics Webbook, http://www.ceramics.nist.gov/srd/summary/scdaos.htm, Accessed November 12, 2012.

[110] Matsumura, T., Konno, T., and Tobe, S., 2010, "Deburring of Micro-Scale Structures Machined in Milling," Erie, Pennsylvania, pp. 341-349.

[111] A. Kienzler, Deuchert, M., and Schulze, V., 2009, "Burr Minimization and Removal by Micro Milling Strategies or Micropeening Processes," 1, pp. 237-243.

[112] Tada, H., Paris, P., and Irwin, G., 2000, The Stress Analysis of Cracks Handbook, American Society of Mechanical Engineers, New York, p. 89.

[113] Robertson, S., and Ritchie, R., 2007, "In Vitro Fatigue-Crack Growth and Fracture Toughness Behavior of Thin-Walled Superelastic Nitinol Tube for Endovascular Stents: A Basis for Defining the Effect of Crack-Like Defects," Biomaterials, 28, pp. 700-709.

[114] Pahl, G., Beitz, W., Feldhusen, J., and Grote, K.-H., 2007, Engineering Design: A Systematic Approach, Springer, pp. 125-141.

[115] Hasson, M., 2010," Corneal Graft Manipulation Spurs Endothelial Cell Loss," Ocular Surgery News, http://www.osnsupersite.com, Accessed November 12, 2012.

[116] Campos, M., Wang, X. W., Hertzog, L., Lee, M., Clapham, T., Trokel, S. L., and Mcdonnell, P. J., 1993, "Ablation Rates and Surface Ultrastructure of 193 Nm Excimer Laser Keratectomies," Investigative Ophthalmology & Visual Science, 34(8), pp. 2493-2500.

[117] SRI Internationl, 2011, http://www.sri.com/rd/electroadhesion.html, Accessed November 12, 2012.

[118] Guo, J. H., 1994, "Investigating the Surface Properties and Bioadhesion of Buccal Patches," Journal of Pharmacy and Pharmacology, 46(8), pp. 647-650.

[119] Heckele, M., and Schomburg, W. K., 2004, "Review on Micro Molding of Thermoplastic Polymers," Journal of Micromechanics and Microengineering, 14(3), pp. R1-R14.

[120] Limaye, A. S., and Rosen, D. W., 2007, "Process Planning Method for Mask Projection Micro-Stereolithography," Rapid Prototyping Journal, 13(2), pp. 76-84.

[121] Ingle, N. P., and King, M. W., 2010, "Optimizing the Tissue Anchoring Performance of Barbed Sutures in Skin and Tendon Tissues," Journal of Biomechanics, 43, pp. 302-309.

[122] Wahl, A. M., 1944, "Mechanical Springs," Penton Publishing Company, Cleveland, Ohio, p. 216.

[123] Kalpakjian, S., 1984, "Manufacturing Processes for Engineering Materials," Addison-Wesley Publishing, p. 407.

[124] Tungjitkusolmun, S., Staelin, S. T., Haemmerich, S. T. D., Tsai, J.-Z., Cao, H., Webster, J. G., Jr., F. T. L., Mahvi, D. M., and Vorperian, V. R., 2002, "Three-Dimensional Finite-Element Analyses for Radio-Frequency Hepatic Tumor Ablation," IEEE Transactions on Biomedical Engineering, 49(1), pp. 3-9.

[125] Ali, M., 2006, "Natural Convection Heat Transfer from Vertical Helical Coils in Oil," Heat Transfer Engineering, 27(3), pp. 79-85.

[126] Carstensen, E. L., Buettner, A., Genberg, V. L., and Miller, M. W., 1985, "Sensitivity of the Human Eye to Power Frequency Electric Fields," IEEE Transactions on Biomedical Engineering, 32(8), pp. 561-565.

[127] Härting, F., and Pfeiffenberger, U., 1982, "Thermal Conductivity of Bovine and Pig Retina: An Experimental Study," Graefes Archive for Clinical and Experimental Ophthalmology, 219(6), pp. 290-291.

[128] Kampmeier, J., Birngruber, B. R. R., and Brinkmann, R., 2000, "Thermal and Biomechanical Parameters of Porcine Cornea," Cornea, 19(3), pp. 355-363.

[129] Friedman, E., Kopald, H., Smith, T., and Mimura, S., 1964, "Retinal and Choroidal Blood Flow Determined with Krypton-85 Anesthetized Animals," Investigative Ophthalmology and Visual Science, 3(5), pp. 539-547.